

CZECH TECHNICAL  
UNIVERSITY IN PRAGUE

FACULTY OF MECHANICAL  
ENGINEERING

DEPARTMENT OF MECHANICS,  
BIOMECHANICS AND  
MECHATRONICS



MASTER THESIS

**Tensegrity Mechanisms with  
Active Vibration Suppression**

Tomáš Šindel

2022

Supervisor: prof. Ing. Zbyněk Šika, Ph.D.



# ZADÁNÍ DIPLOMOVÉ PRÁCE

## I. OSOBNÍ A STUDIJNÍ ÚDAJE

Příjmení:	Šindel	Jméno:	Tomáš	Osobní číslo:	466403
Fakulta/ústav:	Fakulta strojní				
Zadávající katedra/ústav:	Ústav mechaniky, biomechaniky a mechatroniky				
Studijní program:	Aplikované vědy ve strojném inženýrství				
Specializace:	Mechatronika				

## II. ÚDAJE K DIPLOMOVÉ PRÁCI

Název diplomové práce:

Tensegritní mechanismy s aktivním snižováním vibrací

Název diplomové práce anglicky:

Tensegrity mechanisms with active vibration suppression

Pokyny pro vypracování:

- 1) Seznamte se s ovladatelnými tensegritními strukturami obecně a s jejich použitím v mechanismech.
- 2) Seznamte se s různými postupy aktivního snižování vibrací struktur.
- 3) Vyberte tensegritní struktury s robotickým potenciálem a provedte optimalizaci rozmístění aktuátorů různého určení.
- 4) Proveďte detailní návrh a optimalizaci aktuátorů a senzorů pro aktivní snižování vibrací zvolené tensegrity.
- 5) Proveďte srovnání několika variant řízeného snižování vibrací a implementaci vybraného postupu.
- 6) Vyuvinutý postup snižování vibrací ověřte na komplexním simulačním modelu během pohybu robotické tensegrity v pracovním prostoru.

Seznam doporučené literatury:

- [1] Skelton, R., C., De Oliveira, M., C., Tensegrity systems, New York: Springer, 2009.
- [2] Adam B and Smith I, "Tensegrity Active Control: Multiobj ective Approach", Journal of Computing in Civil Engineering, 2007, 21: 3–10.
- [3] Yaowen, O., Xiaodong, F., & Miah, M. S., Active vibration control of tensegrity structures for performance enhancement: A comparative study. Earthquake Engineering and Engineering Vibration, 2019, 18(3), 679–693.
- [4] Šíka, Z., Zavrel, J., & Valasek, M., Residual modes for structure reduction and efficient coupling of substructures. Bulletin of Applied Mechanics, 2009 5(19), 54-59.

Jméno a pracoviště vedoucí(ho) diplomové práce:

prof. Ing. Zbyněk Šíka, Ph.D. odbor mechaniky a mechatroniky FS

Jméno a pracoviště druhé(ho) vedoucí(ho) nebo konzultanta(ky) diplomové práce:

Datum zadání diplomové práce: 22.04.2022

Termín odevzdání diplomové práce: 15.08.2022

Platnost zadání diplomové práce:



prof. Ing. Zbyněk Šíka, Ph.D.  
podpis vedoucí(ho) práce

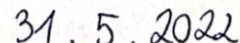
doc. Ing. Miroslav Španiel, CSc.  
podpis vedoucí(ho) ústavu/katedry



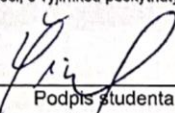
doc. Ing. Miroslav Španiel, CSc.  
podpis děkana(ky)

## III. PŘEVZETÍ ZADÁNÍ

Diplomant bere na vědomí, že je povinen vypracovat diplomovou práci samostatně, bez cizí pomoci, s výjimkou poskytnutých konzultací.  
Seznam použité literatury, jiných pramenů a jmen konzultantů je třeba uvést v diplomové práci.



Datum převzetí zadání



Podpis studenta

# Annotation Sheet

<b>Title:</b>	Tensegrity mechanisms with active vibration suppression
<b>Název:</b>	Tensegritní mechanismy s aktivním snižováním vibrací
<b>Author:</b>	Bc. Tomáš Šindel
<b>Academic year:</b>	2021/2022
<b>Study program:</b>	Applied Sciences in Mechanical Engineering
<b>Department:</b>	Department of Mechanics, Biomechanics and Mechatronics
<b>Supervisor:</b>	prof. Ing. Zbyněk Šika, Ph.D.
<b>Scope of work:</b>	Pages: 103 Figures: 73 Attachments: 1 CD
<b>Keywords:</b>	Tensegrity, robots, active vibration control, active damping, vibration isolation, actuators, sensors, optimal placement
<b>Klíčová slova:</b>	Tensegrity, roboti, aktivní řízení vibrací, aktivní tlumení, vibroizolace, aktuátory, senzory, optimální umístění
<b>Abstract:</b>	This work deals with the synthesis, analysis, and optimization of active vibration suppression of tensegrity manipulators. These structures generally have poor damping properties due to the presence of infinitesimal mechanisms. Therefore, it seems suitable for this task to utilize active means. A comprehensive literature review of tensegrity robotics is performed together with a juxtaposition of different active vibration control approaches. The two domains are then merged and applied to three specific cases of tensegrity manipulators. Concurrently, sensors and actuators are selected for the task and their optimal placement within the mentioned structures is examined. The results suggest that active vibration suppression using decentralized integral force feedback is effective for tensegrity manipulators in terms of damping and vibration isolation.
<b>Abstrakt:</b>	Tato práce se zabývá syntézou, analýzou a optimalizací aktivního snižování vibrací tensegritních manipulátorů. Tyto struktury mají obecně nepříznivé tlumící vlastnosti z důvodu přítomnosti infinitesimálních mechanismů. Proto se zde jako vhodné jeví použití aktivních prostředků. Je provedena komplexní rešerše tensegritní robotiky společně se srovnáním různých přístupů k aktivnímu tlumení vibrací. Tyto dvě oblasti jsou poté sjednoceny a aplikovány na tři konkrétní případy tensegritních manipulátorů. Současně jsou pro tento účel zvoleny senzory a aktuátory, a jejich optimální umístění v rámci zmíněných struktur je zhodnoceno. Výsledky naznačují, že aktivní snižování vibrací pomocí decentralizované integrální silové zpětné vazby je pro tensegritní manipulátory účinné z hlediska tlumení a vibroizolace.

# **Abstract**

This work deals with the synthesis, analysis, and optimization of active vibration suppression of tensegrity manipulators. These structures generally have poor damping properties due to the presence of infinitesimal mechanisms. Therefore, it seems suitable for this task to utilize active means. A comprehensive literature review of tensegrity robotics is performed together with a juxtaposition of different active vibration control approaches. The two domains are then merged and applied to three specific cases of tensegrity manipulators. Concurrently, sensors and actuators are selected for the task and their optimal placement within the mentioned structures is examined. The results suggest that active vibration suppression using decentralized integral force feedback is effective for tensegrity manipulators in terms of damping and vibration isolation.

# **Keywords**

Tensegrity, robots, active vibration control, active damping, vibration isolation, actuators, sensors, optimal placement

## Acknowledgments

I would like to express my gratitude to prof. Zbyněk Šika for his guidance, suggestions, and insistence on high standards, which surely improved the quality of this work. I would like to thank Ing. Tomáš Kaňka for his insight into the domain of tensegrity robotics, which elevated my understanding of the topic. I am also grateful to Ing. Vojtěch Halamka who provided me with the data necessary to finish my work. Lastly, and most importantly, my sincere gratitude belongs to my family, who have shown great patience and understanding during the times of the writing of this work and allowed me to come this far.

## **Declaration of Honor**

The author hereby declares that this work was produced independently under the supervision of prof. Ing. Zbyněk Šika, Ph.D. with the help of the literature cited at the end of this work.

# List of Figures

Figure 1: Sequence of tensegrity deployment states .....	5
Figure 2: Deployment equilibrium manifold .....	6
Figure 3: Examples of tensegrity locomotion modes with different actuations and topologies .....	8
Figure 4: Fully assembled SUPERball in NASA Ames Research Center .....	9
Figure 5: Tetraspine robot virtual model .....	9
Figure 6: Tetraspine physical model .....	10
Figure 7: 3DOF tensegrity manipulator .....	11
Figure 8: TenseBot 6DOF robot .....	12
Figure 9: 2-stage tensegrity tower. a) virtual model, b) physical model.....	12
Figure 10: HEDRA, a bio-inspired robotic manipulator.....	13
Figure 11: Arm-inspired tensegrity manipulator.....	13
Figure 12: Tensegrity manipulator inspired by a human leg .....	14
Figure 13: Feedback control loop .....	16
Figure 14: Feedforward control principle .....	18
Figure 15: Model-based control architecture .....	19
Figure 16: Architecture of data-driven methods .....	19
Figure 17: Collocated sensor-actuator pair for active vibration control of tensegrity tower .....	20
Figure 18: Comparison of collocated and non-collocated control loops applied on a ball-screw feed drive .....	21
Figure 19: Pole-zero alternating pattern of a lightly damped system with collocated control .....	22
Figure 20: a) End-effector force disturbance source; b) Base frame kinematic disturbance; c) Active vibration isolator.....	27
Figure 21: Passive isolator transmissibility for different damping ratio values $\xi$ .....	27
Figure 22: Example of a uniaxial active isolator .....	28
Figure 23: a) Acceleration/velocity-based isolator; b) Equivalent sky-hook damper....	29
Figure 24: Uniaxial force-feedback isolator connecting two flexible bodies .....	30
Figure 25: Force feedback active truss FRF .....	31
Figure 26: IFF root locus plot with interlacing poles and zeros .....	31

Figure 27: Positive position feedback root loci; a) Tuned for the 1st mode; b) Tuned for the 2nd mode .....	32
Figure 28: Plant with a feedback controller .....	34
Figure 29: Various material physical phenomena in terms of stimulus-response.....	35
Figure 30: Typical characteristic of piezoelectric force sensor .....	36
Figure 31: ICP 208C02 force sensor .....	37
Figure 32: ICP® force sensor system schematic .....	37
Figure 33: Piezoactuator characteristics.....	40
Figure 34: APA120ML piezoactuator.....	41
Figure 35: S3 tensegrity simplex.....	43
Figure 36: Task-space coordinate displacements and rotation from given cable contractions (20 mm). .....	44
Figure 37: Cost function variation over possible numbers of actuators.....	46
Figure 38: Optimal large-displacement actuator placement for 3 actuators .....	47
Figure 39: Optimal large-displacement actuator placement for 6 actuators .....	47
Figure 40: Controllability and observability of a simply supported beam.....	48
Figure 41: Structure of the assemblage matrices of the FEM model.....	50
Figure 42: Axial element in initial and final configuration.....	51
Figure 43: 2-stage tensegrity tower of type-2 with fully connected nodes and a top platform .....	58
Figure 44: Best controllability plot relative to the same number of actuators for each possible number of actuators.....	60
Figure 45: Best controllability plot relative to a single actuator for each possible number of actuators .....	61
Figure 46: Best observability plot relative to the same number of sensors for each possible number of sensors .....	61
Figure 47: Best observability plot relative to a single sensor for each possible number of sensors .....	62
Figure 48: Pictorial representation of actuator placement for: a) 3 actuators; b) 6 actuators .....	63
Figure 49: Pictorial representation of sensor placement for: a) 3 sensors; b) 6 sensors	64
Figure 50: Physical demonstrator of the 2-stage type-1 tensegrity manipulator .....	65
Figure 51: Simscape Multibody® model of the tensegrity manipulator.....	65
Figure 52: Displacement and rotation time plot of the top platform.....	67

Figure 53: Manipulator trajectory half-cycle where T is the period of the trajectory....	68
Figure 54: CTC task-space displacement error plot along the trajectory without disturbances.....	69
Figure 55: CTC task-space angular error plot along the trajectory without disturbances .....	69
Figure 56: Tensegrity manipulator use case.....	70
Figure 57: Closed-loop plant model.....	71
Figure 58: Multiple operating point (OP) plant assembly, where sys1, ..., sysN correspond to linearized plants in different OP.....	71
Figure 59: Open-loop multiple OP disturbance response of plant $P_{a1}$ .....	72
Figure 60: Open-loop multiple OP disturbance response of plant $P_{a2}$ .....	73
Figure 61: Singular value bound of closed-loop plant $P_{a1CL}$ with the compared control laws of optimal gains and of the open-loop plant $P_{a1}$ .....	75
Figure 62: Singular value bound of closed-loop plant $P_{a2CL}$ with the compared control laws of optimal gains and of the open-loop plant $P_{a2}$ .....	75
Figure 63: Task-space displacement and velocity error with white noise disturbance ..	78
Figure 64: Disturbance rejection error of the force impulse response .....	80
Figure 65: Deviation of the real cable force from the cable force without white noise disturbance injection .....	82
Figure 66: Energy dissipation of the IFF control for both disturbance types .....	82
Figure 67: Simple planar tensegrity structure .....	86
Figure 68: Eigenmodes of the structure: a) first; b) second .....	88
Figure 69: Controllability and observability energy ellipsoids .....	89
Figure 70: Gramian principal component ratio with varying initial prestressing cable elongation.....	90
Figure 71: Gramian principal component ratio with varying strut-to-cable specific stiffness ratio .....	91
Figure 72: Gramian principal component ratio with varying damping ratio of the first mode relative to the second mode .....	91
Figure 73: Simplified model of an active cable .....	93

# List of Tables

Table 1: Comparison of feedback and feedforward control.....	17
Table 2: ICP 208C02 performance characteristics.....	37
Table 3: ICP 208C02 electrical properties .....	38
Table 4: ICP 208C02 mechanical properties .....	38
Table 5: ICP 208C02 thermal properties .....	38
Table 6: Properties of piezoelectric actuator.....	39
Table 7: APA120ML quasistatic properties.....	41
Table 8: APA120ML dynamic properties.....	42
Table 9: APA120ML electrical properties .....	42
Table 10: APA120ML interfacing specifications .....	42
Table 11: Task-space weights used for optimization .....	46
Table 12: FEM incidence table .....	50
Table 13: User-specified optimization options .....	59
Table 14: PID gains for the CTC controller.....	66
Table 15: Inputs and outputs of the first considered plant $P_1$ .....	71
Table 16: Linearization times (snapshots) relative to the trajectory period $T$ .....	72
Table 17: $H^\infty$ -optimal gains for the chosen control laws .....	74
Table 18: Sigma bound attenuation comparison of different control laws .....	76
Table 19: Injected disturbance noise parameters .....	77
Table 20: Output signal relative power attenuation .....	79
Table 21: FEM incidence table of the case structure .....	86

# Contents

<b>Annotation Sheet .....</b>	<b>iv</b>
<b>Abstract .....</b>	<b>v</b>
<b>Keywords .....</b>	<b>v</b>
<b>Acknowledgments .....</b>	<b>vi</b>
<b>Declaration of Honor .....</b>	<b>vii</b>
<b>List of Figures.....</b>	<b>viii</b>
<b>List of Tables .....</b>	<b>xi</b>
<b>1 Introduction .....</b>	<b>1</b>
1.1 Serial and Parallel Robots .....	1
1.2 General Tensegrity Structure .....	1
1.3 Tensegrity in Robotics .....	2
1.4 Research Motivation .....	2
1.5 Thesis Structure.....	3
<b>2 Tensegrity Mechanisms .....</b>	<b>5</b>
2.1 Locomotion .....	6
2.1.1 Rolling.....	7
2.1.2 Crawling.....	7
2.1.3 Vibration .....	10
2.2 Manipulation .....	10
2.2.1 Early Manipulators .....	11
2.2.2 Multi-stage Manipulators .....	13
2.2.3 Bio-inspired Manipulators .....	14
<b>3 Active Vibration Suppression .....</b>	<b>15</b>
3.1 Closed-loop Direction .....	16
3.1.1 Feedback .....	16
3.1.2 Feedforward .....	17
3.2 Modelling Dependency .....	18
3.2.1 Model-based.....	18
3.2.2 Model-free .....	19
3.3 Relative Sensor and Actuator Location.....	20
3.3.1 Collocated .....	20
3.3.2 Non-collocated .....	21
3.4 Control Distribution .....	22

3.4.1	Centralized .....	22
3.4.2	Decentralized.....	24
3.5	Vibration Isolation .....	26
3.5.1	Sky-hook .....	28
3.5.2	General Force Feedback.....	29
3.5.3	Integral Force Feedback .....	30
3.5.4	Positive Position Feedback .....	32
<b>4</b>	<b>Thesis Objectives .....</b>	<b>33</b>
<b>5</b>	<b>Actuators and Sensors .....</b>	<b>34</b>
5.1	Sensors .....	35
5.2	Actuators .....	38
<b>6</b>	<b>Actuator Placement for Large Motion Control.....</b>	<b>43</b>
<b>7</b>	<b>Actuator and Sensor Placement for Active Vibration Suppression .....</b>	<b>48</b>
7.1	FEM Model of Tensegrity Structure .....	48
7.2	Force Jacobians .....	51
7.3	State-space Representation.....	52
7.4	Optimality Criterions .....	53
7.4.1	Degree of Controllability .....	53
7.4.2	Degree of Observability .....	54
7.4.3	Degree of Balanced Interaction.....	56
7.5	Implementation .....	57
7.5.1	Quantitative Optimization Results .....	59
7.5.2	Qualitative Optimization Results .....	62
<b>8</b>	<b>Active Vibration Suppression Superimposed on Large Motion Control.....</b>	<b>65</b>
8.1	The Model .....	65
8.2	Control Law Comparison.....	73
8.3	Simulation .....	77
<b>9</b>	<b>Conclusion Remarks .....</b>	<b>83</b>
<b>A.</b>	<b>Gramians of a Simple Planar Tensegrity .....</b>	<b>86</b>
<b>B.</b>	<b>Active Cable Model .....</b>	<b>93</b>
<b>C.</b>	<b>Electronic Data .....</b>	<b>97</b>
	<b>Bibliography .....</b>	<b>98</b>

# 1 Introduction

## 1.1 Serial and Parallel Robots

When it comes to robotic manipulators, two main categories come to mind: serial and parallel robots. They have been used in industry for decades and ever since Unimate 1900 made its entrance to the market in 1961, the general population gradually became aware of how the robotic manipulator structures are composed. The idea stays generally the same nowadays. A chain of rigid links anchored to the ground with the end-effector at the end, moving things from place to place. Between the ground and the load resides a great opportunity for innovation. Serial robots, being the most publicly known form of these structures, contain the mentioned rigid links in *series* and the actuator of a given link moves it relative to the previous one. This approach enables the robot to reach a relatively large workspace when compared to its build-up space. There is, however, a tradeoff and when the load is applied to the structure at its end-effector, the force is transferred through the serial chain, causing bending moments and torque concentration at the joints [1]. This phenomenon then leads to a relatively low stiffness-to-mass ratio when compared to its counterpart – a parallel robot. This robot, on the other hand, utilizes multiple force transfer pathways, which result from the structure being composed of multiple links connected in *parallel*. The resulting effect is then an increased stiffness sacrificed for a reduced workspace-to-build-up-space ratio and lower dexterity [2].

## 1.2 General Tensegrity Structure

Tensegrity structures are considered a promising candidate to take the desirable properties of both aforementioned configurations. Their serial-parallel structure allows them to distribute the loading forces evenly within its elements and negate the origin of bending moments while maintaining their dexterity by a variable equilibrium state [1]. They are defined according to [3] as a mechanical system composed of a disjoint set of compressive elements (e.g., struts) within a continuous set of tensile elements (e.g., tendons, cables). A poetic version of this definition according to Buckminster Fuller is “islands of compression inside an ocean of tension” and it is expanded in [4] that only the structures in a stable equilibrium can be called tensegrities. Their unique structure presents a set of interesting properties potentially useful in robotic applications.

Generally, stiffness increases with tension and decreases with compression, making the tensegrity structure efficient in terms of stiffness-to-mass ratio [5]. Furthermore, the elements represent only the essential loading pathways and are loaded uniaxially, making the structure easy to analyze [1]. Another unique characteristic is that a tensegrity structure is in equilibrium under zero external actions. This property is called *self-stress*, a state of internal tension between its elements, scalable by the pretension coefficients while preserving identical geometry [6]. Variation of this self-stress state then changes the stiffness of the entire structure accordingly. The condition of stable self-stress is then called the *prestressability* condition. A possible tension modification combined with large force diffusivity could possibly allow the structure to operate when partially damaged and compensate for the damage by taking a new equilibrium shape [5].

### 1.3 Tensegrity in Robotics

The tensegrity structure design has been analyzed extensively in architecture and civil engineering [7]. However, as they are subjected to constant tension, they found themselves in a state of nonzero potential energy. This property is advantageous for energetically efficient motion including large deformations, making it suitable for robotic applications [8], most likely in space robotics due to its deployment capabilities. Moreover, it has been shown that it is desirable for the tensegrity structure to perform its large-scale motion using infinitesimal mechanisms [6]. Along these mechanisms, the power dissipation due to linear kinetic damping is zero and the variation of elastic potential energy is small, allowing for more efficient deployment methods.

### 1.4 Research Motivation

The absence of damping is, however, a problem for the dynamic excitations of the structure caused by external disturbances - vibrations. It has been shown that infinitesimal mechanisms are always present in tensegrity structures, hence these structures have generally small damping, making them susceptible to long-lasting oscillations and dangerous resonant behavior [9]. With the growth of the possibilities of mechatronics, active vibration suppression is expected to serve as the most suitable way to tackle this challenge. It offers a better, more universal, and cost-effective performance than passive vibration suppression, which can also compromise the dynamic properties of the tensegrity structure [10].

## 1.5 Thesis Structure

The structure of the thesis is given as follows: In the theoretical section, an extensive literature review of tensegrity robots and active vibration control is conducted. The tensegrity robotics chapter is focused primarily on the tensegrities capable of large structural displacements, suitable for robotic applications – namely folding, deployment, locomotion, and manipulation. The main focus is given to the latter two applications due to their considered interaction with the environment. Locomotive robots are reviewed as the starting point for the reader to appreciate the mechanical complexity of tensegrity robots, whereas the manipulator section is tracking a deliberate improvement of these structures with a goal of possible industrial applications. A clear inspiration by and the similarity with the biological world are emphasized in this section and demonstrated by concrete examples.

Further, in the following chapter, the review generalizes outside of the tensegrity domain into the theory of active vibration control. Linear control theory for disturbance rejection and control attenuation is reviewed. Various control laws are reviewed with their advantages and drawbacks. SISO and MIMO methods are juxtaposed, and the simplifying assumptions are reviewed for different cases. An assessment of sensors and actuators used for vibration control is also performed.

In the practical part of this work, the objectives thereof are dissected in a detailed manner and each following section is justified for our application in tensegrity mechanisms. Different sensors and actuators for active vibration suppression are compared and properly selected for implementation in conjunction with the preferred control method. Lastly, the quantitative parameters of sensors and actuators are chosen based on the available options and given criteria for the feedback-loop performance.

The next two sections deal with the optimal placement of actuators and sensors. Firstly, a few examples of tensegrity virtual models are analyzed in terms of sensitivity along large displacement paths. These results are then assessed for the proper placement and functionality of large-displacement actuators, for example, winches or McKibben artificial muscles. Besides, the section elaborates on the theory of linear controllability and its contribution to actuator placement optimization in terms of small displacements. A finite-element dynamical model of a simple tensegrity structure is derived analytically

and the controllability Gramians with certain simplifying assumptions are then exploited to provide a novel controllability cost function formulation, homogenizing the structural eigenmodes. The actual optimization is then performed, and the results are shown, providing useful information for decision-making purposes. Alongside, the linear observability theory is also utilized to derive a simplified version of the observability Gramian, resulting in a novel cost function formulation for sensor placement optimization. The results of this optimization are also displayed and together with the previous results they provide an insight into the used state-space formulation and its usefulness for collocated control.

In the next section, the previously reviewed control laws are evaluated and compared. The considered factors, such as performance, robustness, energy efficiency, cost-efficiency, complexity, and generalizability to nonlinear systems, are incorporated into the process of decision-making. Together with the previously acquired knowledge of sensors and actuators, the most suitable control law is selected, and its application justified for a specific example.

The final segment of the work deals with the practical implementation of the chosen active vibration suppression strategy. A given virtual tensegrity model undergoing large displacements is used and the closed-loop vibration control performance is evaluated alongside the open-loop case. The procedure is performed for an optimal gain value obtained by a control synthesis and the influence of the gain on the vibration attenuation is also discussed.

## 2 Tensegrity Mechanisms

In this chapter, a general overview of the tensegrity robotics field is encompassed. An extensive amount of literature has covered an assessment of static tensegrity properties, such as form-finding, prestressability, stiffness, etc., currently applicable to a great extent in civil engineering and architecture. There is only a relatively small amount, however, of research publications focused on the tensegrity structures undergoing large structural deformations. The reason is a highly nonlinear dynamic behavior complicating the analysis in many ways. Therefore, a useful approach for the large deformation description has been shown to include quasi-static path planning strategies [6], where the motion follows an equilibrium manifold defined by the prestress distribution within the structure. Using this method, the robot switches between the adjacent static equilibria, which allows for a wide variety of form-finding methods to be exploited [5]. Moreover, the property of the motion along an equilibrium manifold offers an increase in energy efficiency, when compared to classic rigid-body robots, for it allows large deformations to take place with a minor change in potential energy [5], utilizing the fundamental property of infinitesimal mechanisms, which will be discussed in the next chapter, and the property of nonzero potential energy in the equilibrium state as well. This property then translates into an energy-efficient deployment. An example of such deployment is shown in Figure 1, which displays a sequence of consecutive prestressable configurations for a 3-stage rotationally symmetric case, and in Figure 2 showing an equilibrium manifold of a deployment path.

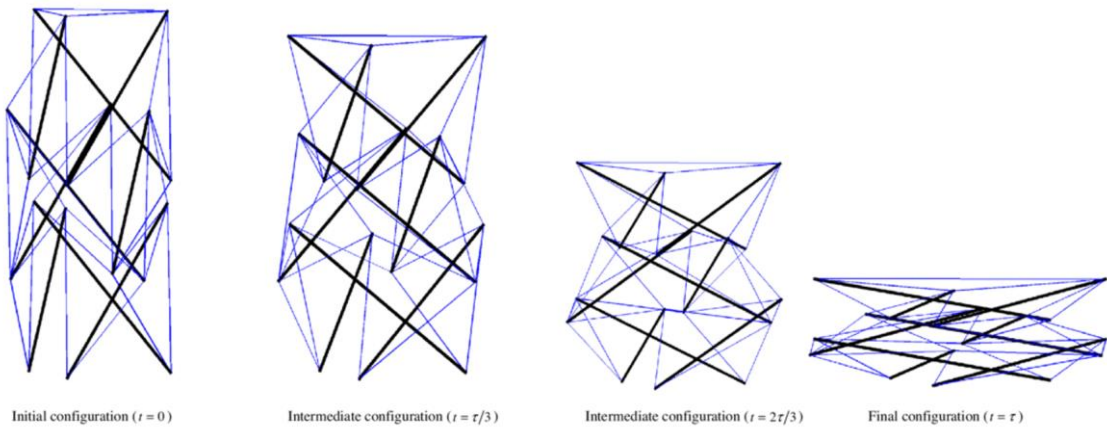
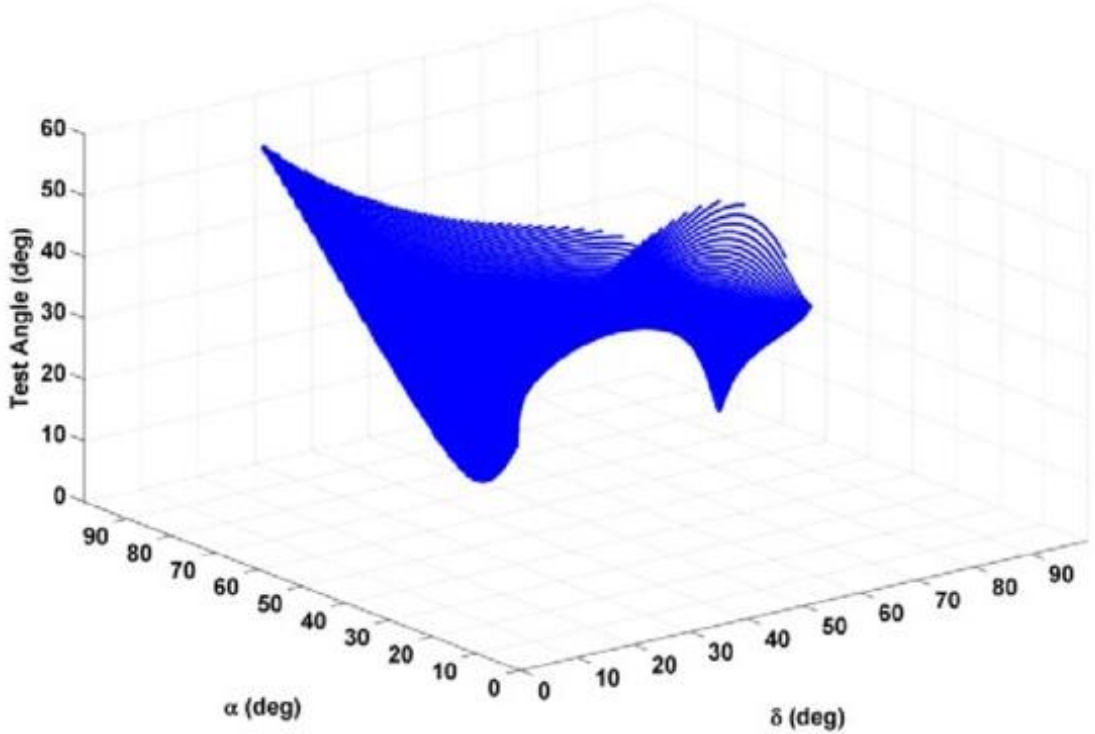


Figure 1: Sequence of tensegrity deployment states [11]



*Figure 2: Deployment equilibrium manifold [11]*

The main research areas for dynamically controlled tensegrities include manipulation, locomotion, and novel gripper designs, often utilizing biomimicry combined with anthropomorphic features. The latter comes from the fact that tensegrity structures can be frequently found in biology [12], underlining the efficiency of these structures by the actual evolution.

## 2.1 Locomotion

In robotic locomotion, the main task of the robot is to transport oneself relative to a global reference frame in terms of an untethered movement. With the locomotion covering a substantial part of the effort and thus achieving a greater advancement in the overall tensegrity robotics field [8], various locomotion modalities have been investigated for tensegrity structures with some examples mentioned below and displayed in Figure 3. The main advantage of using the tensegrity structures for locomotion is their robustness to the outside environment in terms of damage tolerance and the diffusive force distribution, which allows the structure to be less susceptible to failure when subjected to an unpredictable external disturbance, especially during highly dynamic motion [13].

### **2.1.1 Rolling**

The most widely used mode of tensegrity locomotion is rolling, where the motion is performed by a periodic sequence of impacts of different polyhedron faces on the surface, connected by the edge at which the turnover is taking place. The movement is triggered by deforming the structure in such a way that moves the center of mass out of the stability prism projected vertically by the stability polygon, composed of the vertices touching the surface [8]. Leaving this polygon allows the structure to settle in a state of lower potential energy during the movement. The tensegrity shapes used for this locomotion strategy are characterized by a higher number of symmetries, often approximating the shape of a sphere. The leading example of this mode is the SUPERball [14] by NASA Ames Intelligent Robotics Group and Dynamic Tensegrity Robotics Lab and is shown in Figure 4. This robot was designed for space exploration purposes due to its low mass-to-stiffness ratio, deployment capabilities and damage robustness. It is shaped as a 6-strut icosahedron, which is the most frequent topology of tensegrity rolling robots and weighs 21 kg with diameter of 1.7 m [14].

### **2.1.2 Crawling**

Crawling, being the next described mode of locomotion, takes a more biomimetic approach to motion. Instead of switching between adjacent local energetic minima naturally, it utilizes the ground reactive force of contact points as the main driving factor. These contact points are then used as feet to push the structure forward, as frequently occurring in the natural world. Specific robots of this type can then perform snake-like movements or gaits. Up to this point, however, to the authors knowledge, this type of locomotion has only been realized in simulation.

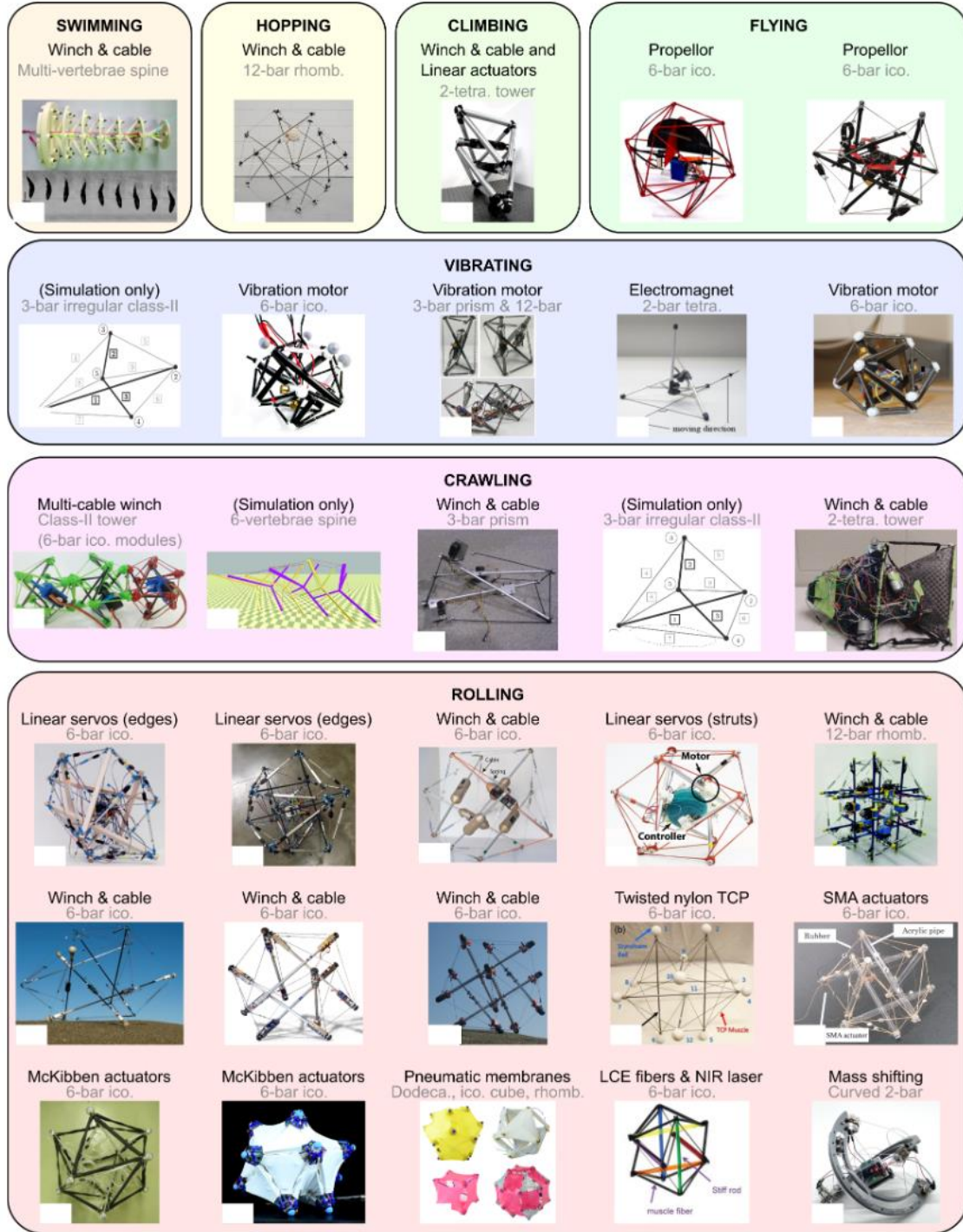


Figure 3: Examples of tensegrity locomotion modes with different actuations and topologies [8]

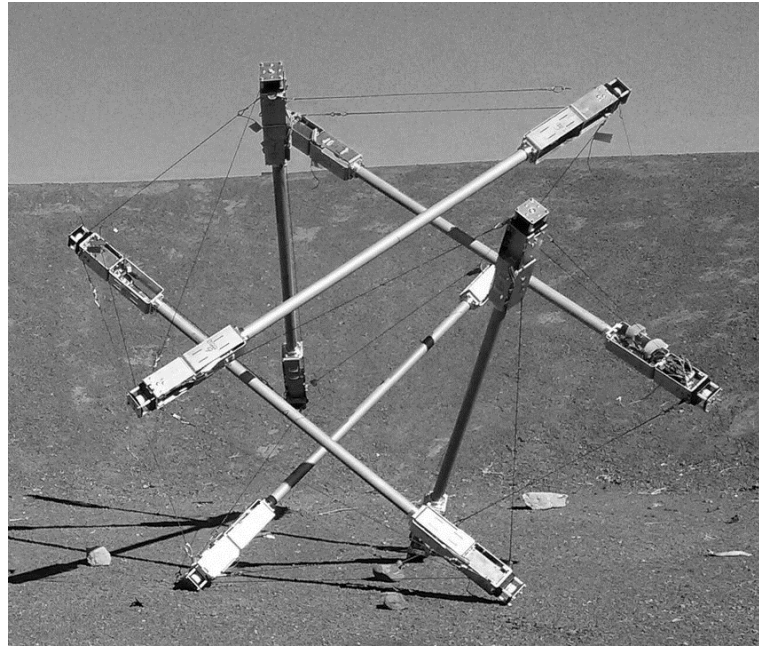


Figure 4: Fully assembled SUPERball in NASA Ames Research Center [14]

For example, the Tetraspine robot inspired by the animal spinal structure, is composed of tetrahedron-shaped elements connected by six strings, resulting in a stellated tensegrity spine. The motion relies heavily on a proper synchronization of the movement, hence preferably utilizing central pattern generators (CPGs) [15]. The advantage of this topology compared to the spherical one is the structural modularity, allowing the composing modules to be manufactured more efficiently while being able to create more complex shapes. In Figure 5 the Tetraspine virtual model is shown and Figure 6 displays the robot *in ferro*.

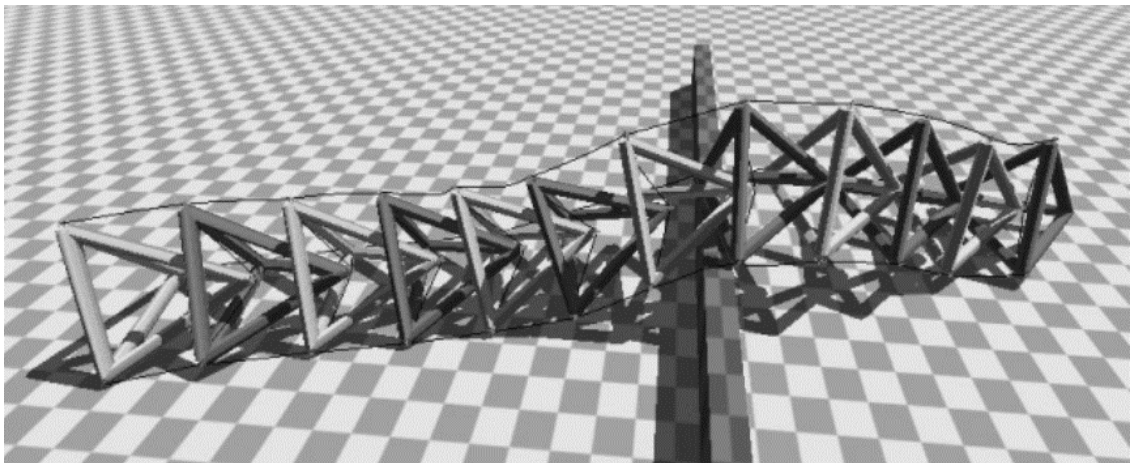
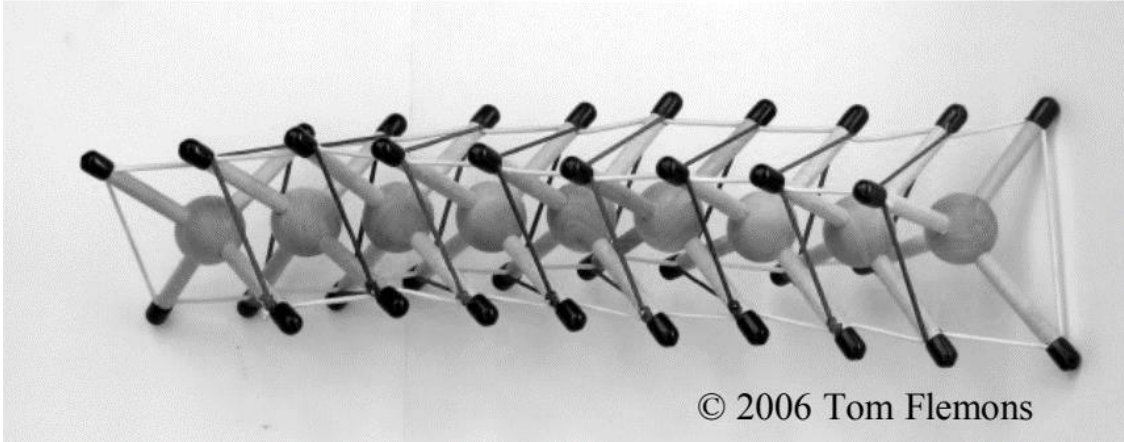


Figure 5: Tetraspine robot virtual model [15]



© 2006 Tom Flemons

Figure 6: Tetraspine physical model [15]

### 2.1.3 Vibration

The last discussed locomotion type shows quite different characteristics than the aforementioned cases and is quite contrary to the main idea of this work, for it uses vibration as the main source of movement. It relies on the dynamic excitation of the structure by various oscillatory elements, such as eccentric mass motors or electromagnetic oscillators [8]. The characteristic resonant behavior then causes the structure to “hop” and propel forward. Its advantage over the previous examples is the fact that it does not require large deformations to perform the movement, thus allowing for a better utilization of linear control methods. However, since the main topic of this paper is the *suppression* of vibrations, further discussion of this type of motion shall not take place in this work. Lastly, there is a vast number of other modes of tensegrity locomotion and the reader can be referred to Figure 3 for more information.

## 2.2 Manipulation

As of the time of writing of this work there was a less significant progress in the field of tensegrity manipulators compared to the locomotors. Therefore, this section contains a review of multiple areas dealing with constrained tensegrity motion. Robotic manipulation is basically a displacement action of a load relative to the reference frame, where the force exerted on the load is transferred by the end-effector to the manipulator, which is constrained to the reference frame, often holonomically.

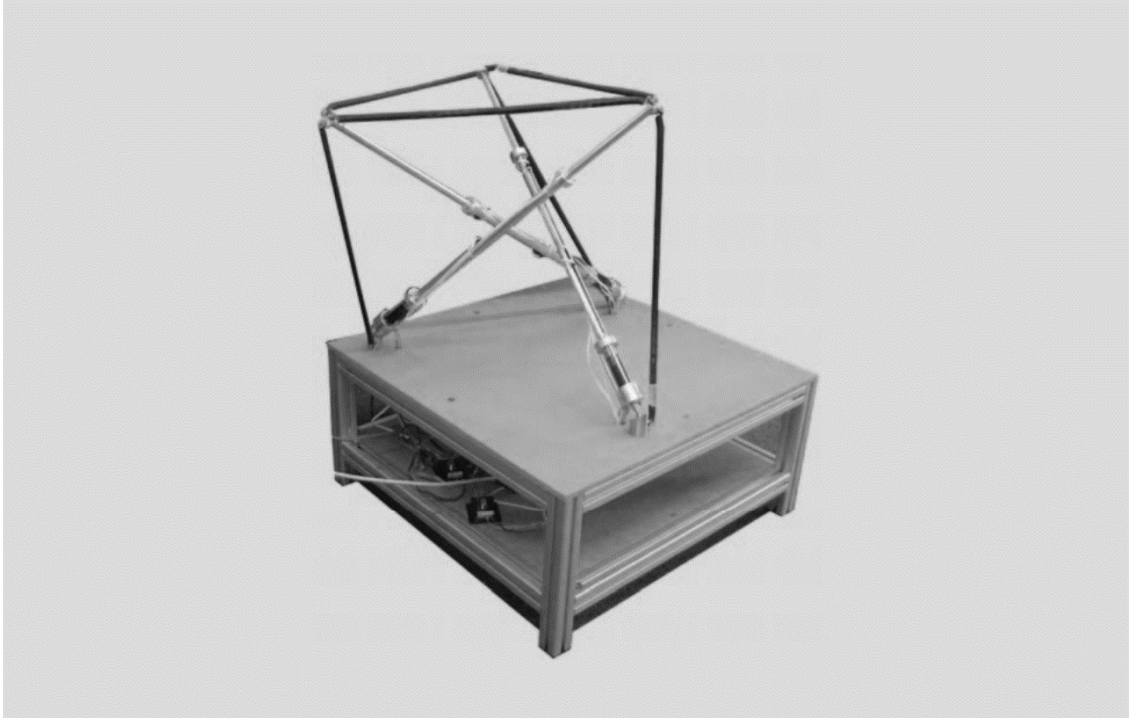


*Figure 7: 3DOF tensegrity manipulator [16]*

### 2.2.1 Early Manipulators

The first attempt to use tensegrity structure for manipulation was made by [16] who constructed a minimal tensegrity robot anchored to the ground and composed of three struts, resulting in a 3DOF manipulator shown in Figure 7. Prismatic morphology of this robot allowed for a distinction between the frame anchor and the end-effector and provided an insight into the constrained kinematics of these structures. Useful properties of prismatic tensegrities for manipulation resulted in a further investigation, for example, of quadrilateral or dual-triangular topologies [1]. The TenseBot by NASA-Ames Research Center expanded the manipulation workspace and dexterity by incorporating six struts, and thus creating an analogy of a 6DOF Stewart platform [17, 18] as shown in Figure 8.

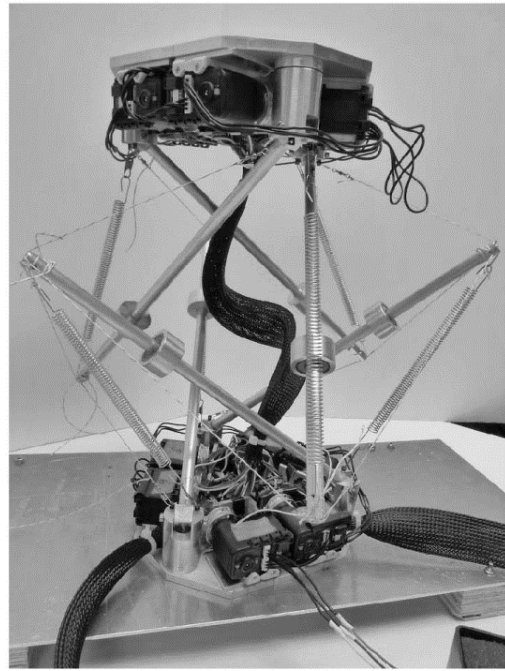


Figure 8: TenseBot 6DOF robot [18]

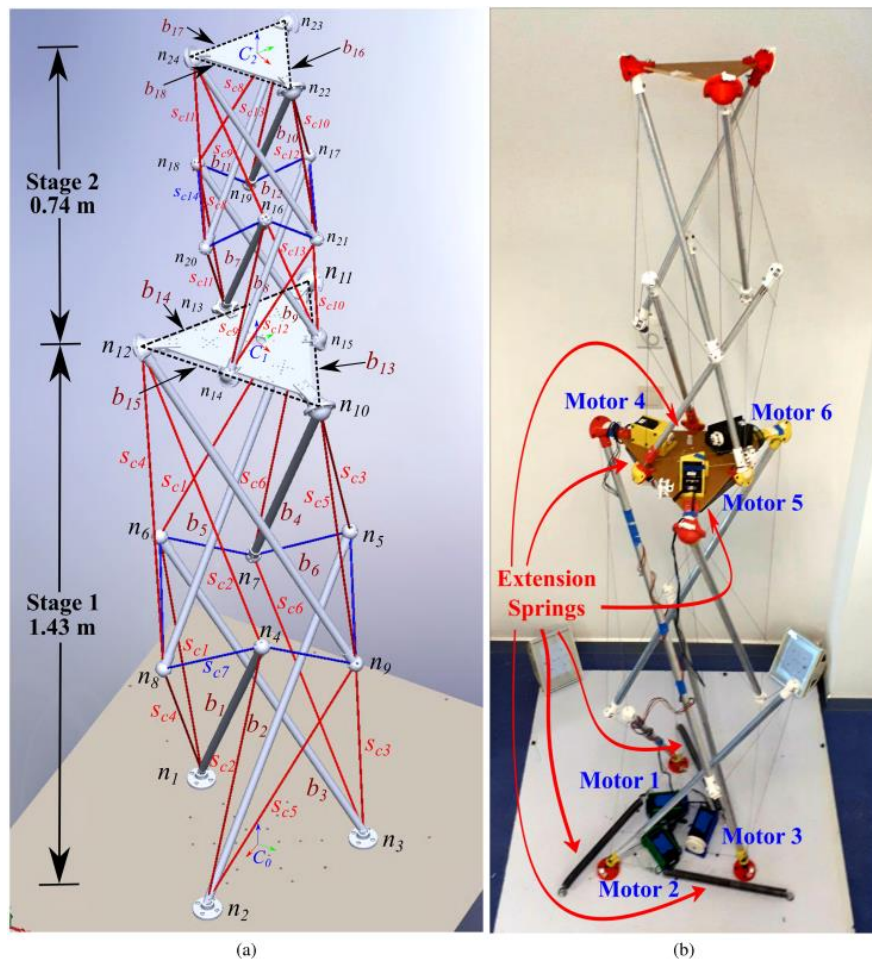


Figure 9: 2-stage tensegrity tower. a) virtual model, b) physical model [19]

### 2.2.2 Multi-stage Manipulators

Progressing into the 2-stage prisms, allowing for a substantial workspace expansion, the authors of [19] constructed a mechanism with 3 struts in each stage with intermediary platforms between the stages and developed a corresponding generalized dynamical model with incorporated damping effects, which they showed to be a necessary step towards a successful system modelling. The mechanism is displayed in Figure 9 and provides a realistic idea of the tensegrity manipulator stacking potential and hence its modularity, where the tensegrity simplexes serve as the possible modules, being a 3-strut ( $S_3$ ) simplex in this case.

The modularity capability has then been emphasized in [20] where Hedra, a fully-fledged *in ferro* manipulator with a cable-driven gripper, was developed. This bio-inspired manipulator, composed of polyhedral parallel modules, shows a clear aim at the robotic manipulation domain by unifying the advantages of rigid and soft robots. Physical model of Hedra can be seen in Figure 10.

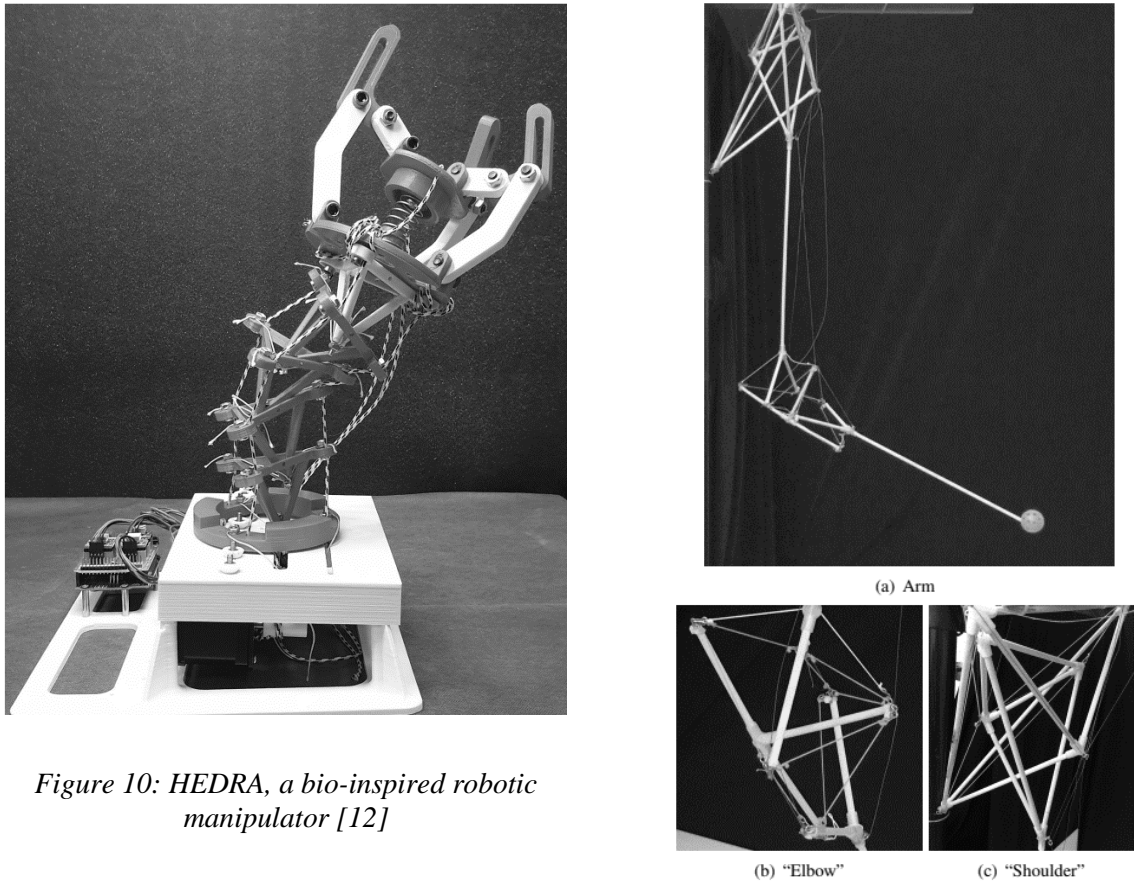
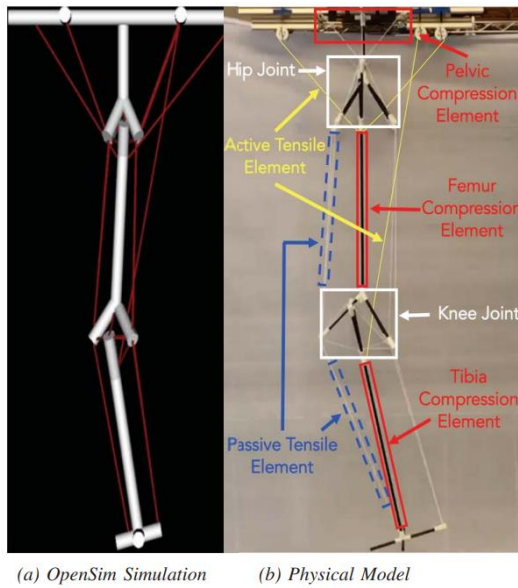


Figure 10: HEDRA, a bio-inspired robotic manipulator [12]

Figure 11: Arm-inspired tensegrity manipulator [13]

### 2.2.3 Bio-inspired Manipulators

Traversing into the biomimetic area, a similarity between the role of fascia in biological organisms and tensegrity tendons has been described [1]. This naturally led many researchers to investigate the structures of tensegrities in correlation with biomechanics, especially in the context of humanoid musculoskeletal robotics. Lessard *et al.* have designed a humanoid robotic arm inspired by the biomechanical function of shoulder and elbow joints [12]. As can be seen in Figure 11, the rigid elements provide the role of a structural skeleton, whereas the tendons are analogical to muscles and fascia of the joints. Functional redundancy of the arm is also addressed in the paper. Following their work, Jung *et al.* have focused on the functionalities of the lower body and the proposed a leg model containing a knee and a hip joint [21]. The tensegrity-based approach leads to a better agreement with the human musculoskeletal function than the conventional revolute joint model and the authors highlight the incorporation of internal joint flexibility implemented in the manipulator. In Figure 12 a comparison between the virtual and the physical model is shown.



*Figure 12: Tensegrity manipulator inspired by a human leg [14]*

The current chapter has shown that in spite of the novelty of tensegrity robotics, there is a substantial amount of research results advocating the adoption of these structures. The potential thereof gives us an opportunity to expand the functionalities of mechanisms, bridge a gap between artificial and biological mechanisms, and, ultimately, take the best of both worlds from the rigid and soft robotic fields.

### 3 Active Vibration Suppression

There are three main types of vibration control: passive, semi-active and active. The passive type, still being the most conventional of the three, is based on inherent properties of the structure itself. The most common example would offer itself to be the passive damping of a car wheel. The dampers have inherent force-velocity characteristics, imprinted in them during the manufacturing process, and these stay the same if we neglect the temperature changes and the mechanical wear over time. Other examples would include elastomers or dynamic vibration absorbers which, despite their technological sophistication, are only fine-tuned for a given application. Active and semi-active methods have shown themselves to be more universal, for they can be deliberately adjusted in real time to produce a desired response. Semi-active devices, such as magneto-rheological fluid dampers, can only absorb energy from the interacting system, hence cannot destabilize it. This property is often desirable in terms of reliability. Nonetheless, their performance is quite limited because of it, even when sophisticated nonlinear control is used. The passive and semi-active methods essentially rely on their composing material and precision components. These drawbacks, simultaneously with improvements in computation and electrical component properties and their declining cost, caused the active vibration suppression to get more and more adopted throughout the industry. It can potentially increase performance in a given control bandwidth while reducing the application cost.

Active structures, sometimes referred to as *smart* structures, are composed of a mechanical system coupled with sensors and actuators, connected by a closed loop. The actuators can add energy into the system, opening the possibility of functional improvement. This fact means, however, that a poorly designed regulator can destabilize the structure. For this reason, it is paramount in this case to design the control system carefully and ensure its robustness to parameter and input uncertainties [22]. Let us now reference a few of the most established classification aspects of active disturbance rejection control.

### 3.1 Closed-loop Direction

Firstly, we can divide the vibration control strategies by the closed-loop direction, hence the direction of the information flow. The basic two kinds are *feedback* and *feedforward* control. The former, being more conventional, is therefore not the only approach available, and the reader thus gets more tools to utilize for their specific application.

#### 3.1.1 Feedback

Feedback control tries to stabilize the system and to minimize the error between the desired reference signal and the system output by compensating for the system disturbance accordingly. For this reason, feedback controllers are often referred to as *compensators*. In Figure 13 the basic principle of the loop is shown. The plant  $G(s)$  is controlled by the compensator  $H(s)$  to minimize an error signal  $e = r - y$  after the disturbance  $d$  is injected.

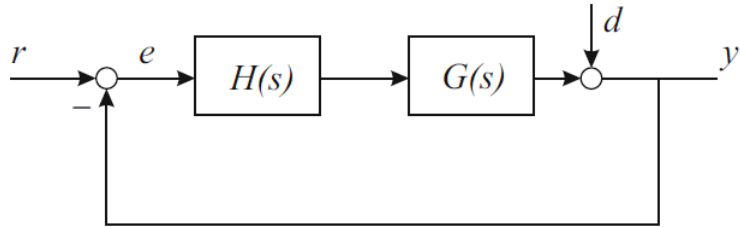


Figure 13: Feedback control loop [22]

We can reformulate the previous statement in terms of disturbance rejection. The damping objective of the feedback control can be formulated as a minimization of the transfer function

$$\frac{y(s)}{d(s)} = \frac{1}{1 + G(s)H(s)} \quad (3.1)$$

which is done by maximizing  $GH$ . This can be achieved *without the prior model knowledge* and generally can be done so for moderate gain values [22]. This method, on the contrary to the feedforward approach, acts globally.

### 3.1.2 Feedforward

Feedforward control, on the other hand, can be considered as a local method, because the mentioned bandwidth may contain locations where the disturbance signal is amplified. Nevertheless, it has been shown that this method is very effective for vibration attenuation with a deterministic disturbance [23] and its principle is displayed in Figure 14. It relies on the correlation between the original disturbance, called primary disturbance, and the reference signal, and tries to produce a secondary disturbance which cancels out the primary source at the error output. This is generally achieved by producing a signal of an opposite phase and works for any frequency. Therefore, it is often referred to as *adaptive filtering*. It is suitable for narrow-band disturbance sources and heavily relies on the availability of the reference signal correlated to the primary disturbance. For this reason, feedback control is generally more popular [22]. Table 1 encapsulates the advantages and disadvantages of these two methodologies, including model-based feedback control approach.

*Table 1: Comparison of feedback and feedforward control [22]*

Type of control	Advantages	Disadvantages
<b>Feedback</b>		
Active damping	• no model needed	• effective only near resonances
	• guaranteed stability when collocated	
Model based ( $LQG, H_\infty \dots$ )	• global method	• limited bandwidth ( $\omega_c \ll \omega_s$ )
	• attenuates all disturbances within $\omega_c$	• disturbances outside $\omega_c$ are amplified
		• spillover
<b>Feedforward</b>		
Adaptive filtering of reference ( $x$ -filtered LMS)	• no model necessary	• reference needed
	• wider bandwidth ( $\omega_c \simeq \omega_s/10$ )	• local method (response may be amplified in some part of the system)
	• works better for narrow-band disturb.	• large amount of real time computations

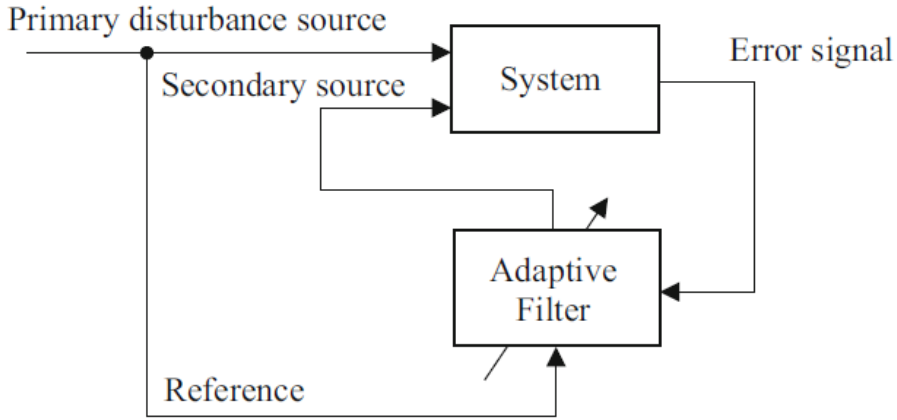


Figure 14: Feedforward control principle [22]

## 3.2 Modelling Dependency

Another point of view that can be taken in regard to classification of vibration control is a distinction between model-*based* and model-*free* controllers.

### 3.2.1 Model-based

The former relies profoundly on the mathematical model used to describe the system. This approach is reliable as long as an accurate model of the phenomena involved is available. In the case of flexible robots, for instance, this model is usually formulated as an infinite-dimensional set of partial differential equations (PDEs), which is then discretized to form a finite-element model [24]. This leap into the finite dimensionality carries a risk of so-called *spillover*, which occurs when the truncated vibrational modes of a structure compromise the controller performance outside of its bandwidth [22]. Another potential drawback of this approach is a questionable robustness to parameter uncertainties, compared to the theoretical model, where ideal and deterministic properties are assumed [24]. There are some non-negligible benefits, nonetheless. This methodology enables us to interpret the system's behavior and understand the causes and effects more deeply. Moreover, we can simulate the model behavior when the real system does not yet exist, and to consider a plethora of different configurations. This will always be beneficial in the design of artifacts. Figure 15 shows the basic idea of this control.

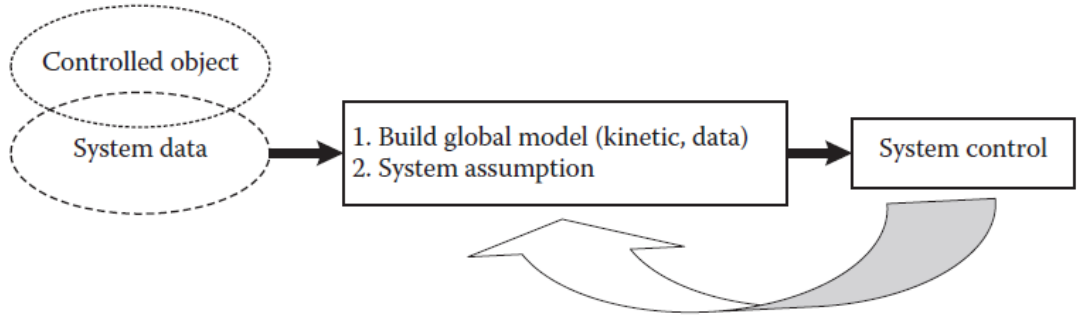


Figure 15: Model-based control architecture [25]

### 3.2.2 Model-free

Contrarywise, the model-free strategy adopts a different philosophy by making a substantial use of the available output data. Provided measurable outputs are available, this approach has demonstrated a comparable performance in flexible robot vibration control as the former case and is more robust to parameter variation [24]. Implementation of this technique, sometimes called *data-driven* control, has shown its practicality when the system model is unavailable, inaccurate, or too complex for a given application, causing latency issues. Independent of the model, often utilizing neural or fuzzy approaches, it brings new possibilities in terms of control speed and robustness. As shown in Figure 16, inputs and outputs of the system must be known a priori, constructing a tailored scheme of regulation. The main shortcoming of the model-free control has already been mentioned. The system I/O data must be known; the system must exist – physically or virtually. This impedes the methods of this type to be used in development of new designs. [25]

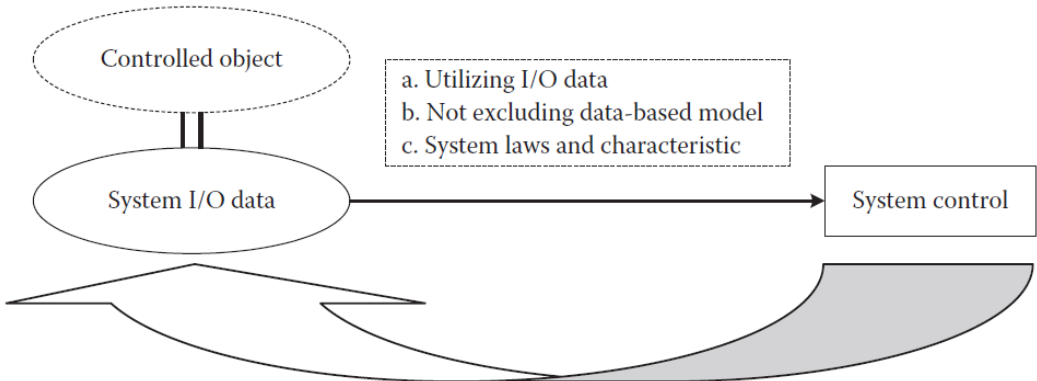


Figure 16: Architecture of data-driven methods [25]

### 3.3 Relative Sensor and Actuator Location

By this classification we can divide control to *collocated* and *non-collocated*. For a lightly damped system with the assumption of perfect sensor/actuator dynamics we can state the following distinctions.

#### 3.3.1 Collocated

Collocated control is the case when a sensor and an actuator have identical position and state direction, meaning that the measured quantity is also being controlled. Figure 17 shows the use thereof for the practical case of tensegrity structure active vibration control. It can be shown that this fact ensures robustness in terms of stability, represented by an infinite gain margin of the system. Furthermore, it always leads to alternation of poles and zeros in the vicinity of imaginary axis, which guarantees robustness to parameter uncertainties and asymptotic stability for most SISO systems. However, in the following chapter it will be shown that this property can be generalized to certain MIMO systems as well. Specific circumstances will determine the usability of this approach, but, generally, it should be implemented whenever possible.

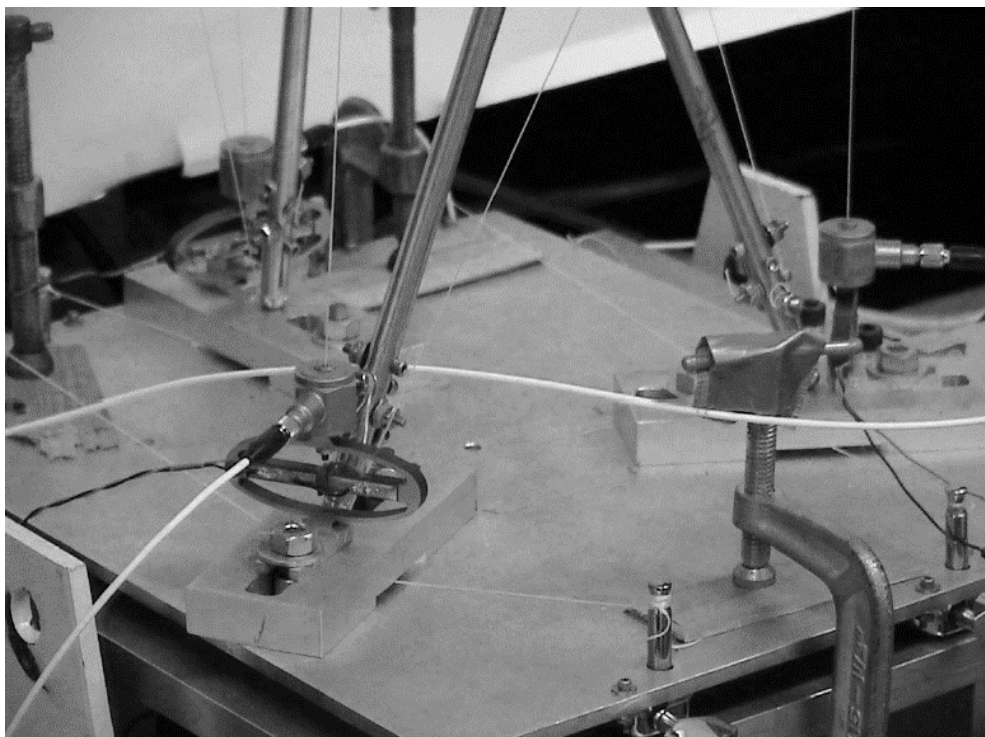


Figure 17: Collocated sensor-actuator pair for active vibration control of tensegrity tower. The pair consists of a force sensor and a displacement amplified piezoactuator (APA). It is placed in the direction of a prestressed tendon near the bottom platform, ensuring minimal influence of the pair on the dynamics of the structure. [26]

Finally, the phenomenon referred to as *pole-zero flipping* cannot occur for collocated systems, which emphasizes the use of this approach when safety and reliability is more important than performance. The effect of pole-zero flipping will be discussed in more detail in the following paragraph.

### 3.3.2 Non-collocated

The opposite of the former case is the non-collocated control, as shown in Figure 18 on the example of a ball-screw feed drive. Its sparse usage can be justified by certain inherent characteristics which must be kept in mind, should one consider placing sensors and actuators in different positions and/or orientations. Let us consider a root locus of a SISO system. After the robustness analysis, it is realized that the shape of the locus varies significantly with parameter perturbations. The explanation is, that the gain margin for this case is small, even for a moderate bandwidth. In an application with flexible modes, this constrains the system to have a considerable amount of passive damping always present [22]. Moreover, an occurrence of pole-zero flipping is likely, unless the system is designed with extreme care. In the following paragraph, this phenomenon will be explained.

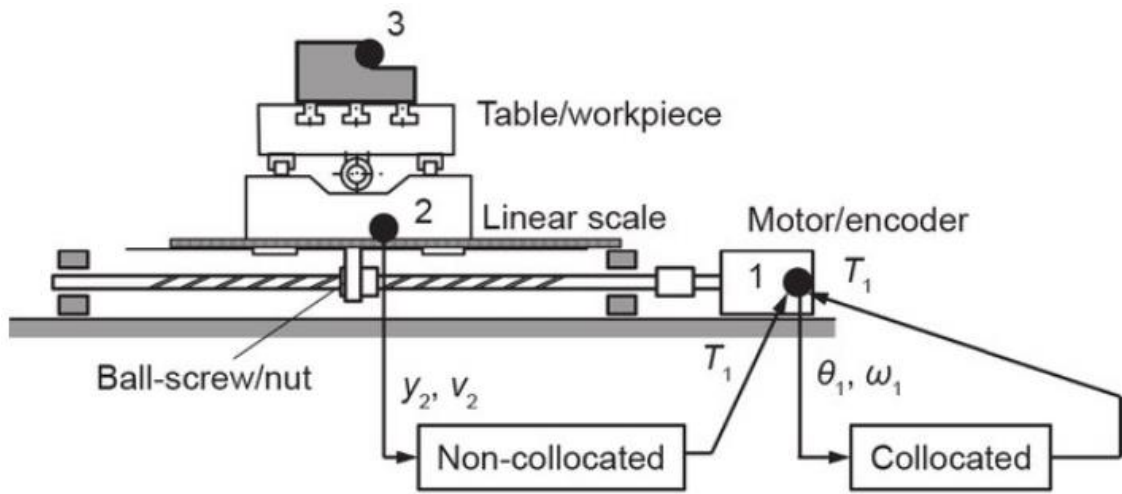
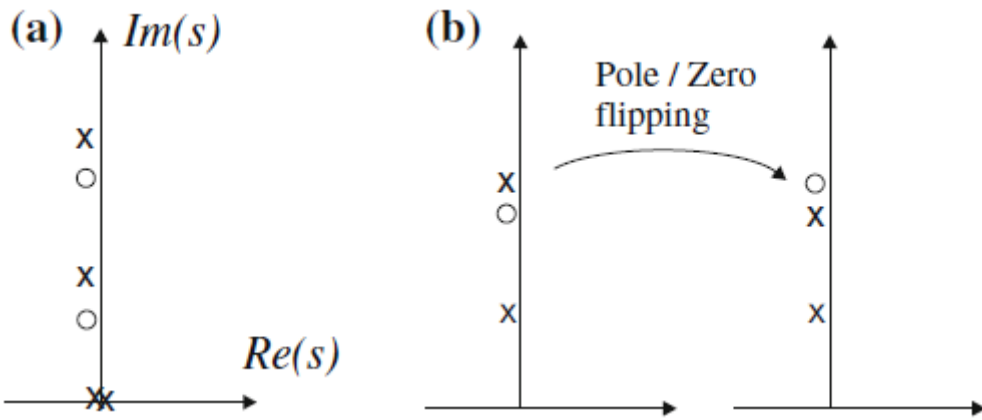


Figure 18: Comparison of collocated and non-collocated control loops applied on a ball-screw feed drive [27]

Pole-zero flipping occurs when poles and zeros of the system are reversed with respect to imaginary axis, as displayed in Figure 19, where it is juxtaposed with the aforementioned collocated case. The root locus does not lie completely in the left half-plane and thus there is a certain gain threshold at which the stabilizing compensator turns

into destabilizing. The occurrence of pole-zero flipping is then responsible for a phase uncertainty of  $360^\circ$  and the only way to tackle this problem is passive damping. There are two main causes of this effect: notch filter, and controllability/observability deficiency. The former case occurs when the controller zeros approach the proximity of system poles, signifying a bad influence of sensor, actuator, or controller dynamics on the structure. The latter case takes place when sensor or actuator is placed near a modal node, well interpretable in the vibration suppression context.



*Figure 19: Pole-zero alternating pattern of a lightly damped system with collocated control (a), compared to the pole-zero flipping pattern of the system with non-collocated control (b) [22]*

### 3.4 Control Distribution

While the previous section dealt with the relative position of sensors and actuators, now we shall classify the control schemes based on the relative position of whole control loops, or alternatively, the number thereof. Linear Quadratic Gaussian (LQG) is a well-known centralized method suitable for disturbance rejection. It has been shown to outperform other methods in rejection of white noise disturbances [28]. However, it is considerably more complex than the algorithms used in decentralized approach. Therefore, only static gain controllers will be considered in this review, since the approaches need to be compared from equal perspectives.

#### 3.4.1 Centralized

Let us have a general state space model with a centralized constant output feedback gain according to [29]:

$$\begin{aligned}\dot{\mathbf{x}}(t) &= \mathbf{A}\mathbf{x}(t) + \mathbf{B}_u\mathbf{u}(t), \\ \mathbf{y}(t) &= \mathbf{C}\mathbf{x}(t), \\ \mathbf{u}(t) &= -\mathbf{G}\mathbf{y}(t)\end{aligned}\tag{3.2}$$

where  $\mathbf{G}$  is not a diagonal matrix. This system, considering no external excitations, then evolves as follows:

$$\mathbf{x}(t) = \Phi(t)\mathbf{x}(0),\tag{3.3}$$

where  $\Phi(t)$  is a state-transition matrix of the controlled system given as

$$\Phi(t) = e^{\mathbf{A}_c t}\tag{3.1}$$

and matrix  $\mathbf{A}_c$  is defined as follows for a constant feedback controller

$$\mathbf{A}_c = \mathbf{A} - \mathbf{B}_u \mathbf{G} \mathbf{C}.\tag{3.4}$$

One can then define a quadratic cost function

$$J = \mathbf{x}^T(0) \int_0^\infty \Phi^T(t) \{ \mathbf{Q} + \mathbf{C}^T \mathbf{G}^T \mathbf{R} \mathbf{G} \mathbf{C} \} \Phi(t) dt \mathbf{x}(0)\tag{3.5}$$

and its differential with respect to the feedback gain matrix

$$\frac{\partial J}{\partial \mathbf{G}} = 2\mathbf{R}\mathbf{G}\mathbf{C}\mathbf{L}\mathbf{C}^T = 2\mathbf{B}_u^T \mathbf{K} \mathbf{L} \mathbf{C}^T,\tag{3.6}$$

where  $\mathbf{K}$  is the solution of the Lyapunov equation

$$\mathbf{K}(\mathbf{A} - \mathbf{B}_u \mathbf{G} \mathbf{C}) + (\mathbf{A} - \mathbf{B}_u \mathbf{G} \mathbf{C})^T \mathbf{K} + (\mathbf{Q} + \mathbf{C}^T \mathbf{G}^T \mathbf{R} \mathbf{G} \mathbf{C}) = \mathbf{0}.\tag{3.7}$$

The algorithm in [28] can be used to find an optimal controller  $\mathbf{G}_{opt}$ , starting with an initial guess  $\mathbf{G}_0$ . Although it cannot be proven that this algorithm converges to a global minimum, practical applications have shown that the final result is invariant to the choice of the initial controller  $\mathbf{G}_0$  with exceptions stated in [28] and can be considered optimal.

### 3.4.2 Decentralized

On the contrary, decentralized static gain feedback control is the simplest feedback control scheme available [28]. In this scheme, system stability is guaranteed when sensors and actuators are collocated and dual [30, 31]. Another advantage is the fact that there need not be a connection between individual control loops in terms of hardware or otherwise, making it possible to produce the sensor-actuator-controller triplets as an integrated modular unit. In mathematical terms, the decentralized control corresponds to the gain matrix  $\mathbf{G}$  in equation (3.1) being diagonal. This imposes a heavy constraint on the system in terms of optimal solution, for that reason the decentralized control is deemed to be generally suboptimal [28]. Finally, let us mention two cases of sensor/actuator pair configuration for collocated decentralized control:

- force actuator and displacement sensor,
- displacement actuator and force sensor.

In the former case, according to [22], the mechanics of the controlled structure is governed by the equation

$$\mathbf{M}\ddot{\mathbf{x}} + \mathbf{Kx} = \mathbf{Bu} \quad (3.8)$$

where  $\mathbf{u}$  is the force input and the output takes on the following form:

$$\mathbf{y} = \mathbf{B}^T \mathbf{x}, \quad (3.9)$$

where  $\mathbf{B}$  is a force Jacobian defined by the actuator placement for which reason  $\mathbf{B}^T$  corresponds to a velocity Jacobian. A single-gain static control law is then defined as

$$\mathbf{u} = -g\mathbf{H}(s)\mathbf{y}, \quad (3.10)$$

where  $g$  is a scalar gain, and  $\mathbf{H}(s)$  is a square matrix, diagonal for the decentralized control. By combining equations (3.8), (3.9) and (3.10), an eigendecomposition of the closed-loop system can be obtained:

$$\{\mathbf{M}s^2 + \mathbf{K}g\mathbf{B}\mathbf{H}(s)\mathbf{B}^T\}\mathbf{x} = \mathbf{0}. \quad (3.11)$$

It can be shown that the asymptotic eigenvalues in this case are independent of  $\mathbf{H}(s)$  [32]. Hence, it can be assumed, without a loss of generality, that  $\mathbf{H}(s) = \mathbf{I}$ , which yields

$$\lim_{g \rightarrow \infty} (\mathbf{M}s^2 + \mathbf{K} + g\mathbf{B}\mathbf{B}^T) \mathbf{x} = \mathbf{0}. \quad (3.12)$$

This equation then yields a solution which is a set of system transmission zeros of the MIMO system. Matrix  $g\mathbf{B}\mathbf{B}^T$  is then the contribution to the global stiffness matrix of the system. The asymptotic behavior, when  $g \rightarrow \infty$ , then causes the stiffness along the controlled DOF go to *ad infinitum*, creating rigid constraints in these directions. Ultimately, the transmission zeros can be thought of as the poles of a modified system, where the motion of controlled DOF is blocked [22].

The latter bullet point deals with an opposite case. For collocated displacement actuators and force sensors, the linearized equations of motion are

$$\mathbf{M}\ddot{\mathbf{x}} + \mathbf{K}\mathbf{x} = \mathbf{B}\mathbf{K}_a\boldsymbol{\delta} \quad (3.13)$$

where  $\boldsymbol{\delta}$  is a displacement input vector,  $\mathbf{K}_a$  is the stiffness matrix of active members of the structure, output is defined as

$$\mathbf{y} = \mathbf{K}_a(\mathbf{B}^T\mathbf{x} - \boldsymbol{\delta}), \quad (3.14)$$

and the control law is of the form

$$\boldsymbol{\delta} = g\mathbf{H}(s)\mathbf{y}. \quad (3.15)$$

The characteristic equation is then

$$\{\mathbf{M}s^2 + \mathbf{K} - g\mathbf{B}\mathbf{K}_a\mathbf{H}(\mathbf{I} + g\mathbf{K}_a\mathbf{H})^{-1}\mathbf{K}_a\mathbf{B}^T\}\mathbf{x} = \mathbf{0}, \quad (3.16)$$

where for  $g \rightarrow \infty$  it simplifies to

$$(\mathbf{M}s^2 + \mathbf{K} - \mathbf{B}\mathbf{K}_a\mathbf{B}^T)\mathbf{x} = \mathbf{0}. \quad (3.17)$$

Thus, the solutions of the above equation are the transmission zeros coinciding with the natural frequencies of a modified system, where the stiffness of active elements is null [22].

### 3.5 Vibration Isolation

Vibration isolation is essential for two kinds of problems, which can be formulated in context of robotic manipulators:

- end-effector to frame isolation,
- frame to end-effector isolation.

If the feedback control is used, it attenuates the structural vibrations from both deterministic and stochastic disturbances. For vibration isolation, we can then define *transmissibility* as the transfer function between the disturbance and the output. For the case displayed in Figure 20a the transmissibility is of the form

$$\frac{F_s(s)}{F_d(s)} = \frac{1 + 2\xi s\omega_n^{-1}}{1 + 2\xi s\omega_n^{-1} + s^2\omega_n^{-2}}, \quad (3.18)$$

while for the case in Figure 20b it is derived as

$$\frac{X_c(s)}{X_d(s)} = \frac{1 + 2\xi s\omega_n^{-1}}{1 + 2\xi s\omega_n^{-1} + s^2\omega_n^{-2}}, \quad (3.19)$$

which is identical to equation (3.19). We can therefore represent the two transmissibilities by the same plot, shown in Figure 21, where the desired response of active isolator is also shown. The desired roll-off is  $-40\text{dB/decade}$  ( $s^{-2}$ ) at high frequencies with no resonant overshoot [22]. At last, in Figure 20c the idea of active vibration isolation is proposed.

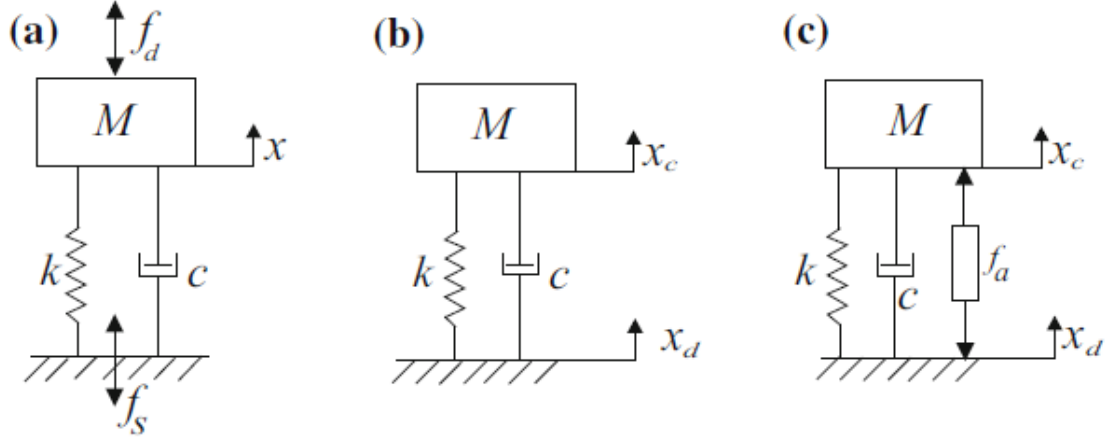


Figure 20: a) End-effector force disturbance source; b) Base frame kinematic disturbance; c) Active vibration isolator [22]

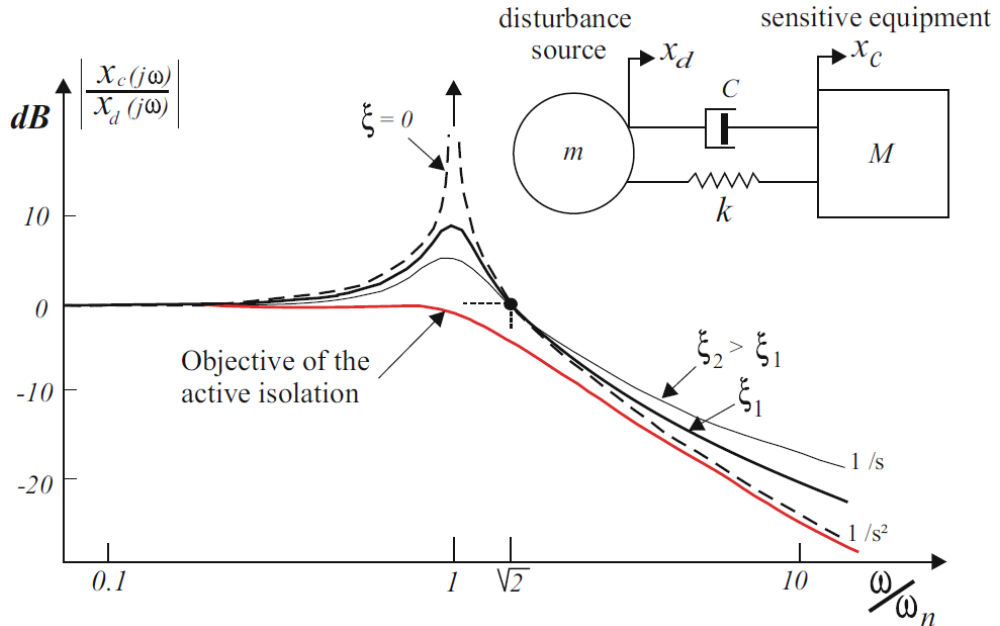


Figure 21: Passive isolator transmissibility for different damping ratio values  $\xi$  [22]

To understand the principle of active vibration isolation, let us consider an example shown in Figure 22. The objective is to minimize the transmissibility between the disturbance  $x_d$  and the payload displacement  $x_c$ . The corresponding equations of motion are

$$\begin{aligned} M\ddot{x}_c + k(x_c - x_d) &= f_a, \\ m\ddot{x}_d + k(x_d - x_c) &= f_d - f_a, \end{aligned} \quad (3.20)$$

which after Laplace transform and inversion yield the open-loop transfer function

$$G(s) = \frac{ms^2}{Mms^2 + (M+m)k}. \quad (3.21)$$

Let us now consider a general velocity feedback law

$$F_a = -H(s)sX_c(s), \quad (3.22)$$

which together with equations (3.20) results in a closed-loop system of equations

$$\begin{bmatrix} Ms^2 + H(s)s + k & -k \\ -k - H(s)s & ms^2 + k \end{bmatrix} \begin{Bmatrix} X_c \\ X_d \end{Bmatrix} = \begin{Bmatrix} 0 \\ F_d \end{Bmatrix}. \quad (3.23)$$

This results in the closed-loop transmissibility transfer function

$$\frac{X_c}{X_d} = \frac{k}{Ms^2 + H(s)s + k}. \quad (3.24)$$

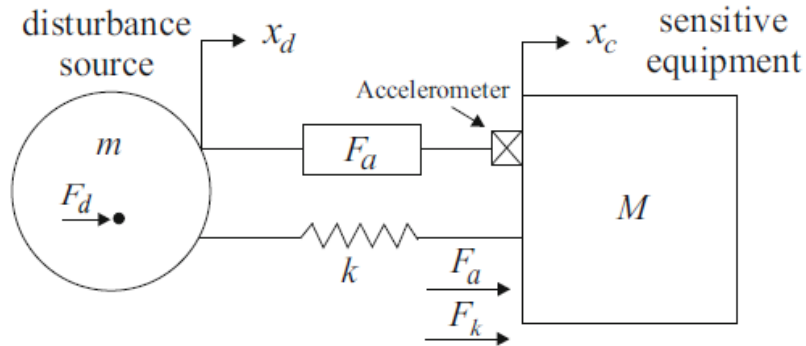


Figure 22: Example of a uniaxial active isolator [22]

### 3.5.1 Sky-hook

Let us now assume the simplest form of a direct velocity feedback, the *sky-hook*, which has transmissibility

$$\frac{X_c}{X_d} = \frac{1}{s^2\omega_n^{-2} + gsk^{-1} + 1}, \quad (3.25)$$

compatible with the aforementioned objective of -40 dB/decade attenuation and no overshoot. This control law is called the sky-hook because of the control force  $f_a = -g\dot{x}_c$  being the same as that of a viscous damper connecting the payload with the surrounding

space (the sky). Its principle can be understood from Figure 23. Root locus plot of this isolator is entirely contained by the left half-plane and hence the controlled system is stable unconditionally [22].

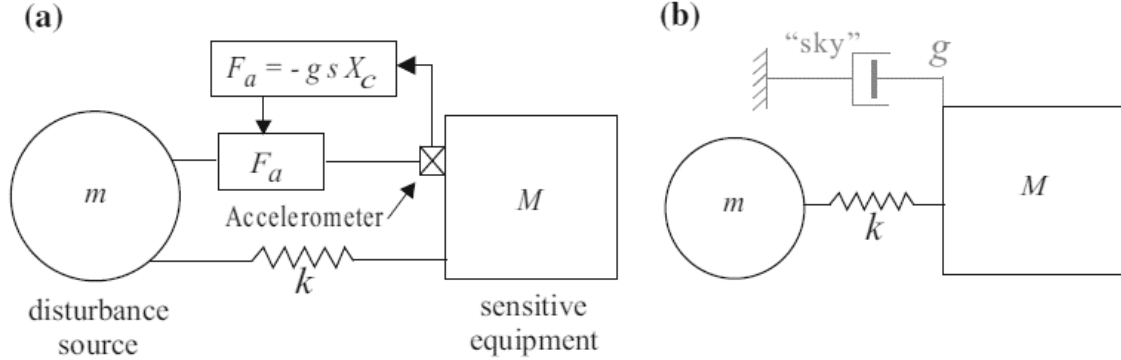


Figure 23: a) Acceleration/velocity-based isolator; b) Equivalent sky-hook damper [22]

### 3.5.2 General Force Feedback

The previous statement is, however, generally not true unless the structure being controlled can be regarded as a rigid body. For our case of tensegrity robots, this is especially false since the structural compliance is one of their main features. Therefore, instead of using an absolute velocity feedback, it is preferable to use force sensors to provide *force feedback* instead, as shown in Figure 24. Then the open-loop transfer function takes the form

$$G(s) = \frac{F_s}{F_a} = \frac{Mms^2}{Mms^2 + (M+m)k}, \quad (3.26)$$

which leads a unique property. The poles and zeros of this function always alternate on the imaginary axis, guaranteeing stability for arbitrary flexible bodies [22]. This can be explained by the continuity of the frequency response function (FRF) between consecutive resonances, where the phase sharply turns  $-180^\circ$  in the undamped case. This then ensures the FRF to cross the zero value, creating a transmission zero. Another advantage would be a generally better sensitivity at low frequencies than with an accelerometer.

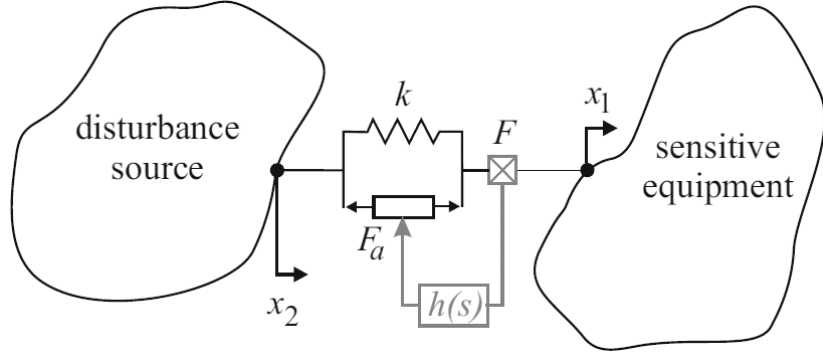


Figure 24: Uniaxial force-feedback isolator connecting two flexible bodies [22]

### 3.5.3 Integral Force Feedback

To elaborate on this method, let us consider an *integral force feedback* (IFF) using a displacement actuator and a force sensor. We then have a governing equation

$$\mathbf{M}\ddot{\mathbf{x}} + (\mathbf{K}^* + \mathbf{b}\mathbf{b}^T\mathbf{K}_a)\mathbf{x} = \mathbf{b}\mathbf{K}_a\delta, \quad (3.27)$$

where  $\mathbf{K}^*$  is the structure stiffness matrix excluding active elements,  $\mathbf{b}$  is the force Jacobian and  $\delta$  is the actuator free stroke.  $\mathbf{K}^* + \mathbf{b}\mathbf{b}^T\mathbf{K}_a$  then corresponds to a global stiffness matrix including these elements and the force output

$$\mathbf{y} = \mathbf{f} = \mathbf{K}_a(\mathbf{b}^T\mathbf{x} - \delta). \quad (3.28)$$

The open-loop transfer function can be written in a modal form and is then formulated as

$$\mathbf{G}(s) = \frac{\mathbf{f}}{\delta} = K_a \left( \sum_{i=1}^m \frac{\nu_i}{s^2\omega_i^{-2} + 1} + \sum_{i=m+1}^n \nu_i - 1 \right), \quad (3.29)$$

where  $\nu_i$  corresponds to the fraction of modal strain energy (MSE) of the  $i$ -th active strut. This situation is shown in Figure 25 in terms of the frequency response.

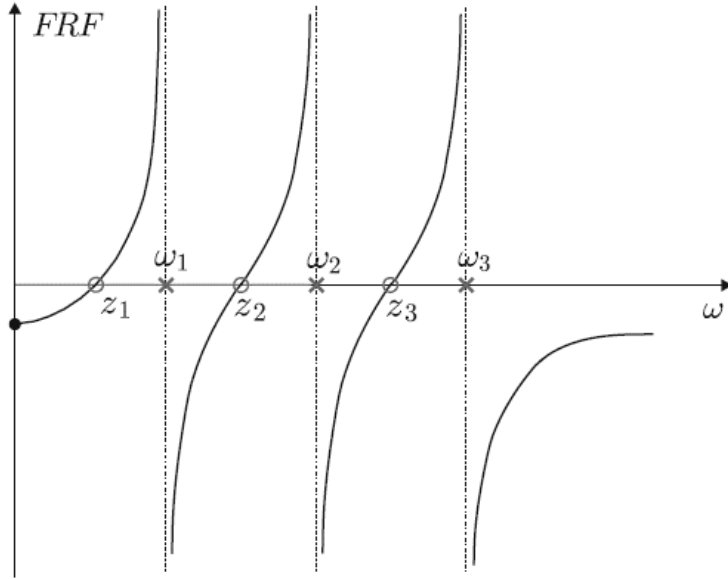


Figure 25: Force feedback active truss FRF [22]

Let us have a positive integral force feedback law defined as follows:

$$\delta = -\frac{g}{s} y. \quad (3.30)$$

Then the root locus exhibits an interlacing pole-zero pattern as shown in Figure 26. The difference between this case and other collocated control laws is the fact that the alternating pattern starts with a transmission zero. Integral feedback then corresponds to a pole in the complex plane origin, departing to negative infinity as  $g \rightarrow \infty$ .

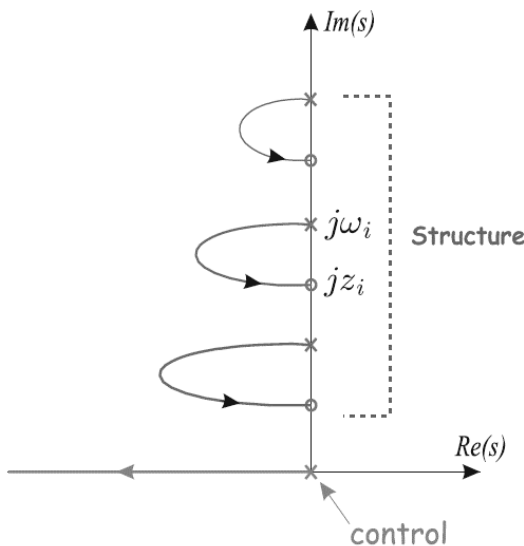


Figure 26: IFF root locus plot with interlacing poles and zeros [22]

### 3.5.4 Positive Position Feedback

Another decentralized collocated control law considered here is to measure position directly. *Positive position feedback* (PPF) controller takes the form of a second-order filter

$$H(s) = \frac{-g}{s^2 + 2\xi_f\omega_f s + \omega_f^2}, \quad (3.31)$$

where the filter parameters  $\xi_f$  and  $\omega_f$  can be tuned for a specific mode attenuation. The negative sign in the numerator changes the sign of the feedback loop, resulting in a positive feedback. In Figure 27 two root loci are shown, each representing a positive position feedback filter tuned for a different vibrational mode. For moderate gains, used in practice, this method can be considered as unconditionally stable. This approach finds its use when a feedthrough component is present in the structure, usually resulting from a mode truncation which can be resolved by using a controller with larger number of poles than zeros. PPF fulfills this need. One of the drawbacks is the fact that PPF controller needs to be tuned specifically for a given mode and thus is basically model-dependent, making it less robust to uncertainties in natural frequency [22].

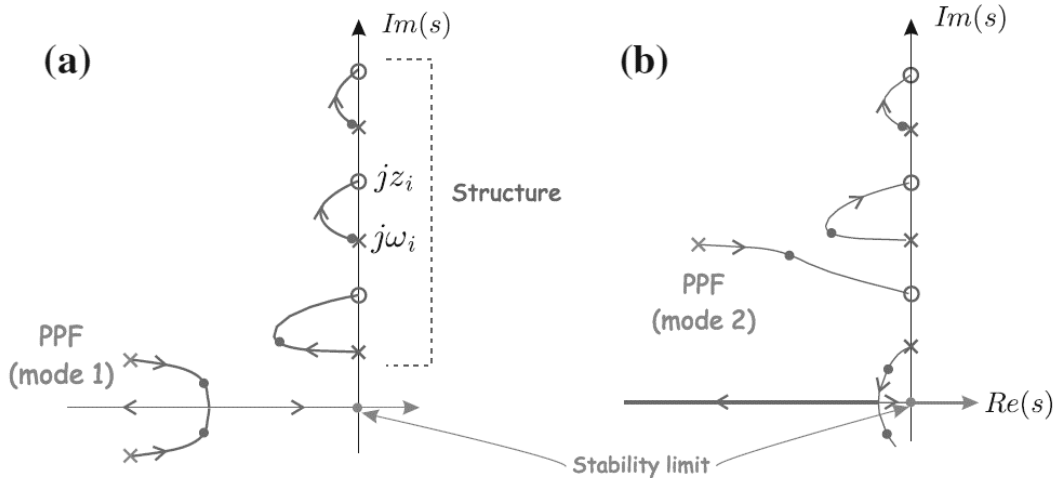


Figure 27: Positive position feedback root loci; a) Tuned for the 1st mode; b) Tuned for the 2nd mode [22]

## 4 Thesis Objectives

This work was written as a part of *Mechatronic tensegrities for energy efficient light robots* research project drafted by prof. Zbyněk Šika of CTU Prague and co-drafted by Dr. Michal Hajžman of UWB [33]. The author follows the work of Ing. Tomáš Kaňka, who in his thesis *Tensegrity mechanisms for replacement of spatial serial robots* reviewed the topic of spatial tensegrity robots in detail. In this work the static and modal properties of tensegrity simplexes, optimization of a serial tensegrity structure, dynamic modelling of this structure, and its basic control implementation were analyzed. The importance of active vibration suppression in tensegrity structures was also highlighted there [34].

The benefit of this work should be the combination of low-authority control (vibration suppression) with high-authority control for large displacements in context of tensegrity robotic manipulation. It represents the next step in the development of tensegrity manipulators for industrial applications, for the disturbance rejection is of a considerable importance in this sector.

Specific objectives of the thesis can be summarized as follows:

- perform a review of tensegrity mechanisms and methods of active vibration suppression,
- compare different vibration suppression control approaches,
- choose structures with the potential for application in robotic manipulation,
- optimize the placement of actuators for large displacements and vibration control,
- optimize the placement of sensors for active vibration control,
- perform a selection of appropriate sensors, actuators, and their parameters for vibration suppression,
- select an appropriate control strategy and design the controller accordingly,
- implement the developed method on a complex simulation model during a motion with large displacements within the workspace.

## 5 Actuators and Sensors

This chapter will be dedicated to the selection of electromechanical components in regard to active vibration suppression. The feedback loop of a controlled plant, as shown in Figure 28, is composed of the plant and the control system. We then include the actuator circuitry in the controller block. This block produces a control actuator output based on the error input. Actuator output can be a force, torque, displacement, or otherwise. Between the control circuit and the actuator an amplifier is usually present. This amplifier uses an energy source to provide the output signal for the actuator and usually provides a galvanic separation of the I/O circuits. Similarly, the sensor circuit is usually featured with a filter and an amplifier of the signal to increase signal-to-noise ratio (SNR) and prevents the loss of downstream information of the signal. Both the sensor and actuator circuitry must be carefully designed to maximize the utilization of the device and, at the very least, ensure its functionality under given conditions. In the domain of active vibration control, the use of smart materials is getting increasingly common. It is their level of multiphysical coupling which is enabling them to offer a completely new range of possibilities in terms of performance, efficiency, and responsiveness. In Figure 29 smart materials are defined with respect to different physical phenomena.

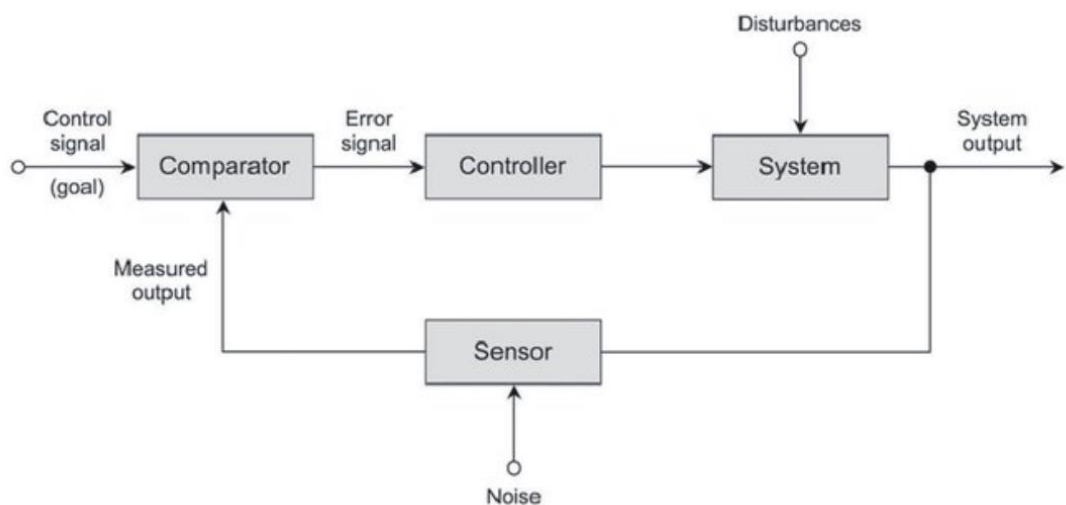


Figure 28: Plant with a feedback controller [35]

<i>Output Input</i>	Strain	Electric charge	Magnetic flux	Temperature	Light
Stress	Elasticity	Piezo-electricity	Magneto-striction		Photo-elasticity
Electric field	Piezo-electricity	Permittivity			Electro-optic effect
Magnetic field	Magneto-striction	Magneto-electric effect	Permeability		Magneto-optic
Heat	Thermal expansion	Pyro-electricity		Specific heat	
Light	Photostriction	Photo-voltaic effect			Refractive index

Figure 29: Various material physical phenomena in terms of stimulus-response. Non-diagonal cells correspond to smart materials. [22]

Given the properties of the piezoelectric material combined with the desirable properties of the *integral force feedback* (force sensing combined with displacement actuation) in context of flexible structures, as mentioned in section 3.5.3, the author will focus primarily on piezoelectric options. Further, we examine the most common sensors and actuators used for vibration suppression in these domains.

## 5.1 Sensors

The considered selection criteria for a force sensor can be summarized as follows:

- measured quantity,
- maximum load,
- sensitivity,
- broadband resolution,
- filtering options,
- temperature sensitivity,
- maximum temperature.

As stated previously, the measured quantity in our case will be a force. A general-purpose piezoelectric force sensor ICP® is considered as the first option, for its application has been verified experimentally in [26]. A sensor-actuator placement is considered in cables, since they do not transfer bending moment and are easily replaceable [26]. For this reason, an excessively large load capacity in compression is not required. Furthermore, piezoelectric force sensors have a high-pass filter characteristic [22]. A typical example is shown in Figure 30. The aim is then to match the usable region shown in the figure with the desired band of the structure.

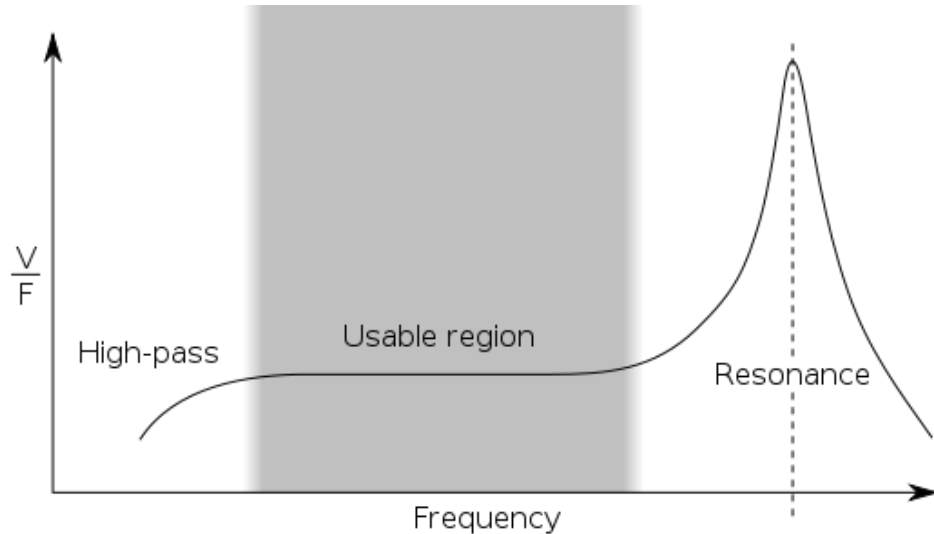


*Figure 30: Typical characteristic of piezoelectric force sensor [36]*

ICP 208C02 force sensor is chosen for the first iteration for this work. It is displayed in Figure 31 and its specifications are listed below as follows: In Table 2 the general performance specifications are shown, Table 3 enlists the electrical properties to be utilized in the design of the circuitry, Table 4 shows basic mechanical data such as weight and various dimensions, and Table 5 finally specifies the thermal properties of the sensor. Finally, Figure 32 displays an electrical schematic of the sensor.



Figure 31: ICP 208C02 force sensor [37]

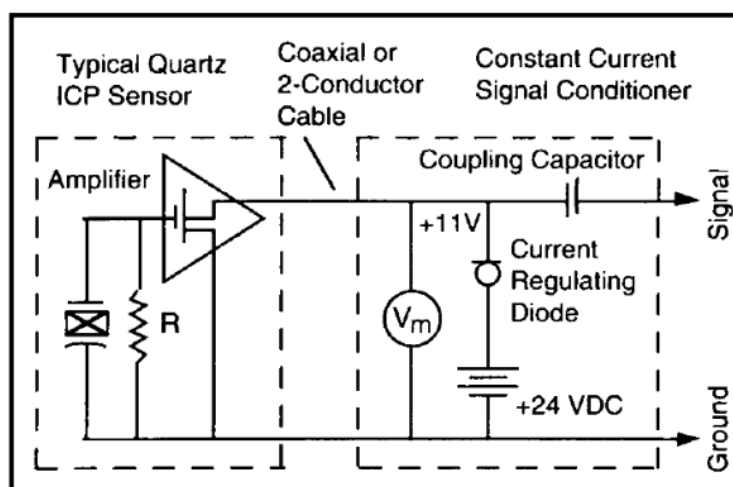


Figure 32: ICP® force sensor system schematic [38]

Table 2: ICP 208C02 performance characteristics [37]

Performance characteristic	Value	Unit
Sensitivity ( $\pm 15\%$ )	11.241	mV/N
Measurement range (peak-to-peak, symmetric)	889.6	N
Max static force (tension)	2.224	kN
Broadband Resolution (1) <sup>1</sup>	0.004	N-rms
Low Frequency Response (-5 %)	0.001	Hz
Upper Frequency Limit	36	kHz
Non-Linearity <sup>2</sup>	$\leq 1$	% FS <sup>3</sup>

<sup>1</sup> Force changes below this threshold will not be resolved

<sup>2</sup> Zero-based, least-squares, straight line method

<sup>3</sup> Full scale

Table 3: ICP 208C02 electrical properties [37]

Electrical property	Value	Unit
Discharge Time Constant	$\geq 500$	s
Excitation Voltage	20-30	VDC
Constant Current Excitation	2-20	mA
Output Impedance	$\leq 100$	Ohm
Output Bias Voltage	8-14	VDC
Spectral Noise (1 Hz)	603	$\mu\text{N}/\sqrt{\text{Hz}}$
Spectral Noise (10 Hz)	123	$\mu\text{N}/\sqrt{\text{Hz}}$
Spectral Noise (100 Hz)	42.7	$\mu\text{N}/\sqrt{\text{Hz}}$
Spectral Noise (1000 Hz)	9.46	$\mu\text{N}/\sqrt{\text{Hz}}$
Output Polarity (Compression)	Positive	

Table 4: ICP 208C02 mechanical properties [37]

Mechanical	Value	Unit
Stiffness	1.05	kN/um
Width (hex)	15.88	mm
Height	15.88	mm
Sensing surface size	12.7	mm
Weight	22.7	g

Table 5: ICP 208C02 thermal properties [37]

Thermal	Value	Unit
Temperature range	-54 to +121	°C
Temperature sensitivity	$\leq 0.09$	% per °C

## 5.2 Actuators

Firstly, in the context of control, actuators can be divided into two groups: *grounded*, and *structure-borne*. The grounded actuators are connected to a fixed frame and apply reaction forces thereon. The examples would be linear or radial motors, shakers, tendons etc. On the other hand, the structure-borne actuators, also called space-realizable, involve only internal self-equilibrating forces, for example proof-mass actuators or active

members, such as cables. The main difference between these two types is that the former can influence the rigid body modes, while the latter cannot [22]. The advantage of the utilization of structure-borne actuators for active vibration control is then clearly the fact that the rigid body modes are not affected. This then enables us to use hierarchical control approach, where the high-authority scheme is responsible for the rigid body modes, while the low-authority scheme deals with the flexible modes.

Most widely used transducers for actuation of active members are the *voice coil* and the *piezoelectric transducer*. Voice coil relies on the magnetic field to generate force. Piezoelectric transducer uses piezoelectric principle instead, and it is the most popular option in vibration control applications. Its advantages over electromagnetic actuators are a short response time and a low energy consumption in steady state [39]. For this reason, only piezoelectric actuators will be considered further in this chapter and their pros and cons are summarized in Table 6.

*Table 6: Properties of piezoelectric actuator [39]*

<b>Advantages</b>	<b>Disadvantages</b>
High resolution	Hysteresis
High generated force (stack actuators)	Drift, creep (1% displacement/time decade)
Good efficiency	Small displacement, stroke (0.1-0.2%)
Short response time (below 1 ms)	Problem of depolarization
No wear (no moving parts)	High supply voltage (60-1000V)
High stiffness of PZT material	Sensitive to radial loads and torsion
Low energy consumption (stationary state)	
Operation at cryogenic temperature	

There are many different types of piezoelectric actuators which can be divided in terms of shape, loading conditions, initial prestress or loading direction. A few examples of piezoactuators based on shape are:

- beams,
- sheets,
- stacks,
- modal filters.

Since we are looking for a general-purpose actuator with a wide bandwidth and a large stroke, the stacked option presents itself as the best candidate for the first iteration.

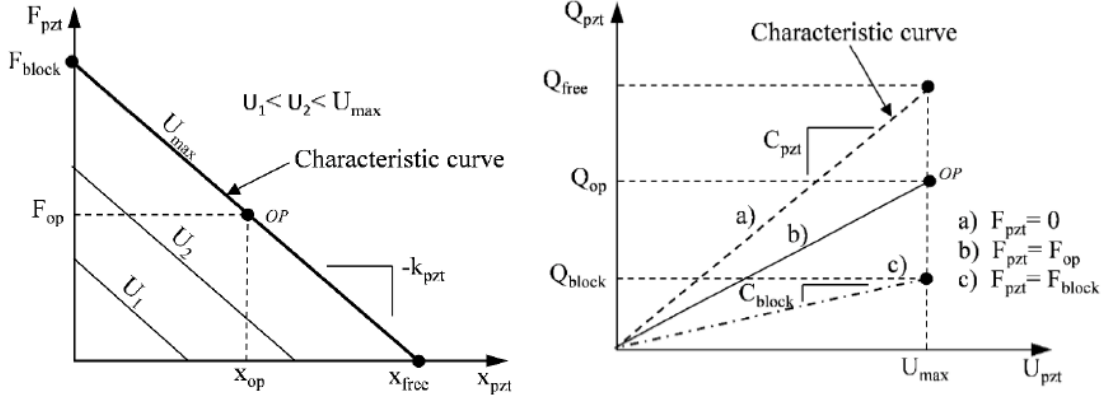


Figure 33: Piezoactuator characteristics [39]

Further, we need to consider that the actuators will be placed in cables where only tensile loads can take place. This fact is represented by a typical force-displacement curve for a piezo-stack actuator, as shown in Figure 33. However, a classical piezo-stack is sensitive to tensile loads, therefore the proposed solutions are *prestress* and *conversion*. Amplified Piezo Actuators (APA®) can be considered as the optimal starting point for our application. They combine preload with conversion in such a way that ensures the tensegrity tensile forces to induce only compressive strain to the actuator, no matter the preload. These features allow the actuator to manage both static and dynamic displacements [40]. This property combined with a substantial and efficient stroke amplification gives us the first candidate for actuation. Other selection criteria for the actuator are listed below:

- actuation bandwidth<sup>4</sup>,
- weight<sup>5</sup>,
- response speed,
- ease of installation,
- free stroke length,
- block force,
- stiffness,
- capacitance,
- dimensions,
- energy efficiency,
- driven quantity.

---

<sup>4</sup> Defined relative to a reference frequency sensitivity ( $\pm 5\%$ ,  $\pm 10\%$ ,  $\pm 1\text{dB}$ ,  $\pm 3\text{dB}$ ).

<sup>5</sup> Our goal is to minimize the dynamic interference of the sensor and actuator with the structure.

Piezoelectric actuators are either *voltage driven* or *current (charge) driven*. The former requires a simpler electrical circuitry than the latter but presents a significant nonlinear behavior at higher drives due to hysteresis. The latter, on the other hand, reduces the hysteretic factor significantly, but involves a complicated circuitry needed to regulate the DC profile of the actuator, otherwise the control signal is eventually distorted by the capacitive load.

For our work, it was decided to use a voltage driven actuator APA120ML, which is displayed in Figure 34. Its properties are listed below in Table 7, Table 8,

Table 9 and

Table 10.

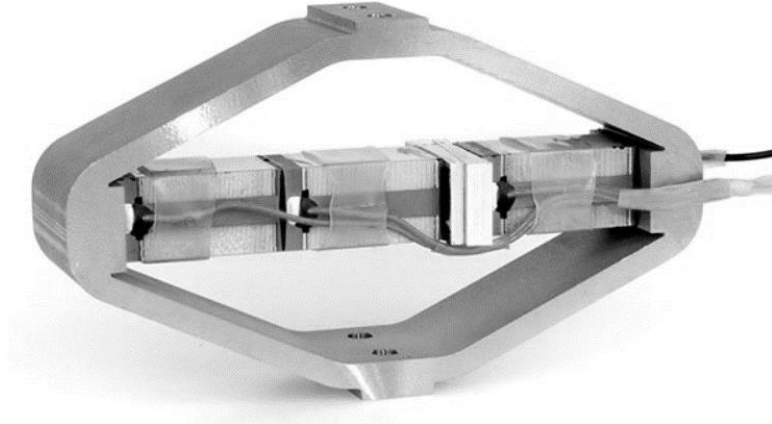


*Figure 34: APA120ML piezoactuator [41]*

*Table 7: APA120ML quasistatic properties [41]*

Quasistatic performance	Value	Unit
Nominal stroke	120	um
Min stroke	110	um
Resolution <sup>6</sup>	6.7	nm
Blocked force	1500	N
Stiffness	12	N/um

---

<sup>6</sup> Quasistatic excitation. With standard LA75 range amplifier. SNR=85dB computed as RMS output signal.

*Table 8: APA120ML dynamic properties [41]*

<b>Dynamic performance</b>	<b>Value</b>	<b>Unit</b>
Resonance frequency (free-free)	5800	Hz
Resonance frequency (blocked-free)	1900	Hz
Force amplitude limit <sup>7</sup>	910	N

*Table 9: APA120ML electrical properties [41]*

<b>Electrical properties</b>	<b>Value</b>	<b>Unit</b>
Voltage range	-20 to 150	V
Capacitance	13	uF

*Table 10: APA120ML interfacing specifications [41]*

<b>Interfacing specifications</b>	<b>Value</b>	<b>Unit</b>
Height	45	mm
Length	79	mm
Width with wires	23	mm
Weight	160	g

---

<sup>7</sup> Maximum pulling or pushing external force, valid up to 90% of the blocked-free resonance frequency of the actuator.

## 6 Actuator Placement for Large Motion Control

This chapter will focus on the optimal placement of high-authority actuators, such as winches or artificial muscles. Contrary to the vibration control actuator placement, as described in chapter 0, the following case includes large spatial displacements of the structure, which are likely to exhibit a nonlinear behavior. For this reason, the linear FEM model in section 7.1 cannot be utilized here. Instead, a nonlinear model was developed in the Simulink® software.

The use case for the optimal actuator placement will be an S3 tensegrity simplex, which is displayed in Figure 35. The simplex consists of three struts with cable-interconnected nodes. All struts are geometrically constrained to have: 1) bottom node of each strut coincident with the shown plane; 2) bottom node of two struts situated in the displayed line; 3) bottom node of one strut spherically constrained to a point on the shown line. In the figure there are three coordinate systems (CS): the world frame, the base CS, and the task-space CS. The base CS has the XY plane coincident with the constraining plane and the X axis parallel to the line connecting bottom nodes of struts 1 and 2, respectively. The task-space CS is oriented in the same manner in the top plane of the simplex, defined by the top nodes of the struts. The kinematic characteristics of the simplex will be assessed in terms of the task-space CS motion relative to the base CS. It allows for an orientation-invariant description of the cell deformation as a whole.

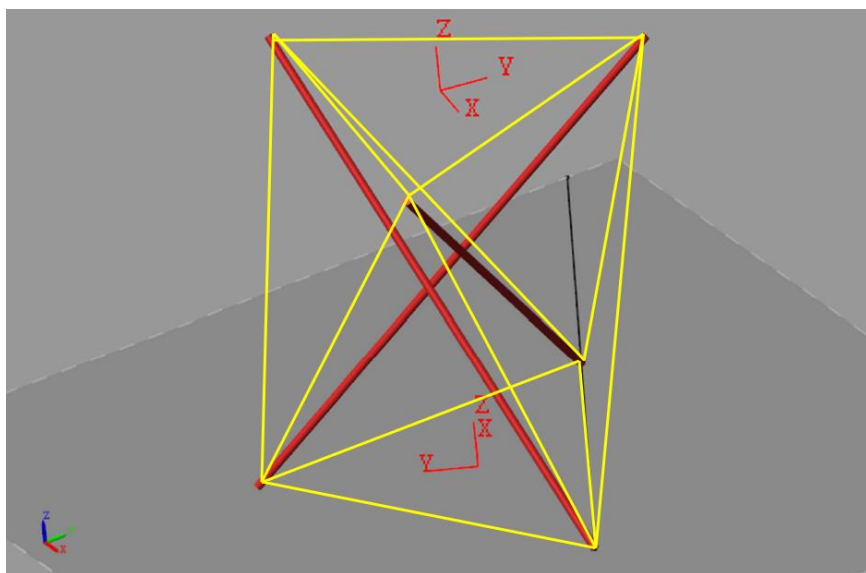


Figure 35: S3 tensegrity simplex (with cables shown in yellow and struts in red)

Static deformation responses of task-space DOFs on single cable contractions of 20 mm were measured, as displayed in Figure 36. These plots display the overall sensitivity integrals of the DOFs on the cable contractions.

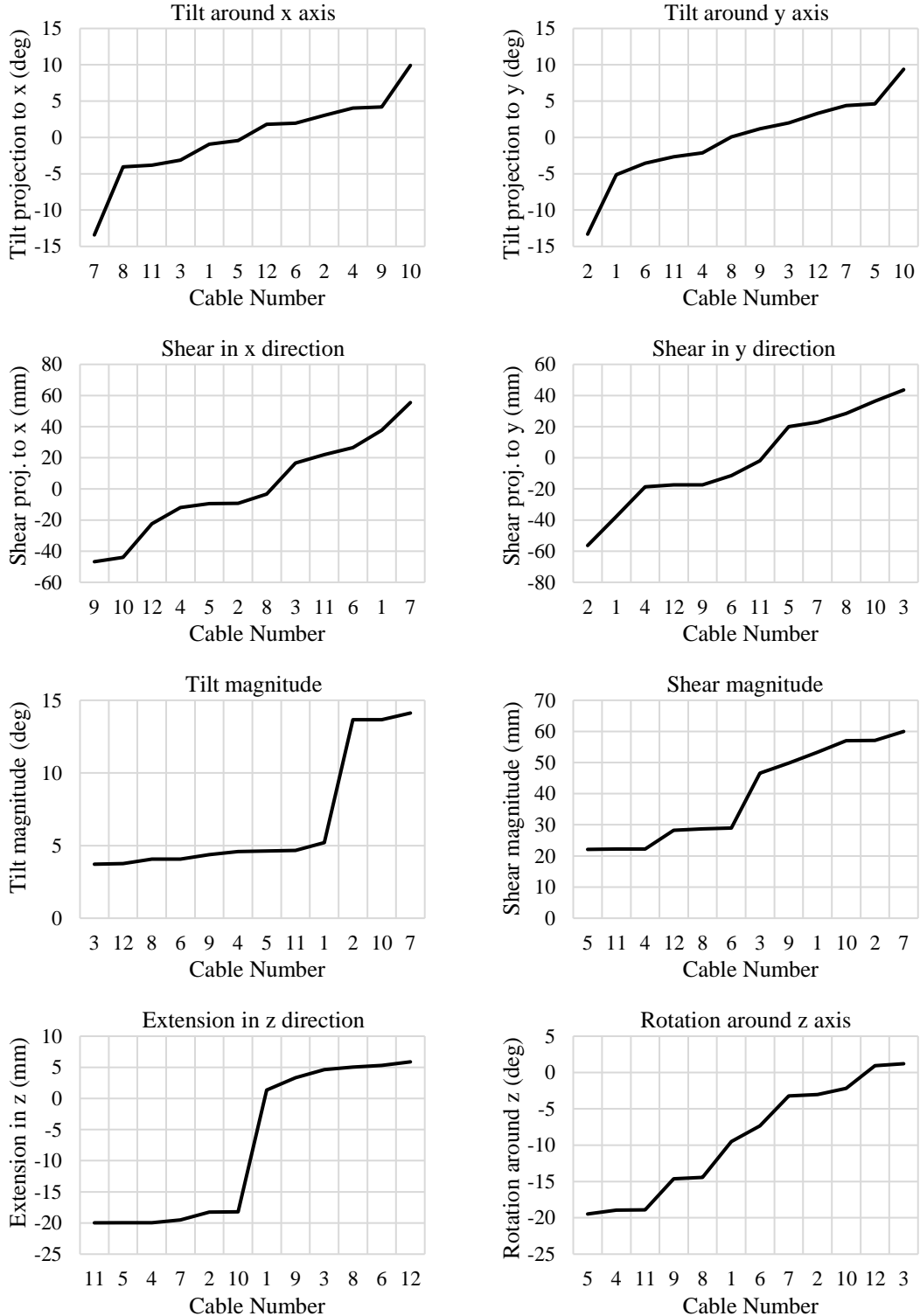


Figure 36: Task-space coordinate displacements and rotation from given cable contractions (20 mm). Each contracted cable is signified by a number on the horizontal axis.

The responses were sorted in an ascending order for clarity. Let us write the unsorted responses in an algebraic vector and their normalized version

$$\mathbf{x}_i = [r_{1i} \quad \cdots \quad r_{ni}]^T, \quad \hat{\mathbf{x}}_i = \frac{\mathbf{x}_i}{\|\mathbf{x}_i\|_2}, \quad (6.1)$$

where  $r_{ji}$  is a response of the  $i$ -th task-space DOF on a contraction of the  $j$ -th cable. Let us now define the vector of actuations

$$\mathbf{c} := [c_1 \quad \cdots \quad c_j \quad \cdots \quad c_{n_c}]^T, \quad c_j := \begin{cases} 1, & \text{if cable } j \text{ is actuated,} \\ 0, & \text{otherwise.} \end{cases} \quad (6.2)$$

The optimization objective is to find a suitable actuation vector  $\mathbf{c}_{\text{opt}}$  for a given set of contraction responses  $\mathbf{x}$ . Due to the nature of cables, the translational DOFs can be actuated in only one direction – the pulling direction. Thus, it is necessary to ensure the motion of DOFs in both directions. For this purpose, we rectify the response vectors in positive and negative senses respectively

$$\begin{aligned} \mathbf{x}_i^+ &= |\mathbf{x}_i| + \mathbf{x}_i, \\ \mathbf{x}_i^- &= |\mathbf{x}_i| - \mathbf{x}_i. \end{aligned} \quad (6.3)$$

Now we can calculate the balanced sensitivity magnitude<sup>8</sup> as follows:

$$\begin{aligned} S_i &= \frac{1}{4} (\mathbf{x}_i^+ \cdot \mathbf{c}) (\mathbf{x}_i^- \cdot \mathbf{c}) = \frac{1}{4} \{(|\mathbf{x}_i| + \mathbf{x}_i) \cdot \mathbf{c}\} \{(|\mathbf{x}_i| - \mathbf{x}_i) \cdot \mathbf{c}\} \\ &= \frac{1}{4} (|\mathbf{x}_i| \cdot \mathbf{c} + \mathbf{x}_i \cdot \mathbf{c})(|\mathbf{x}_i| \cdot \mathbf{c} - \mathbf{x}_i \cdot \mathbf{c}) \\ &= \frac{1}{4} (|\mathbf{x}_i| \cdot \mathbf{c})^2 - (\mathbf{x}_i \cdot \mathbf{c})^2 = \frac{1}{4} \mathbf{c}^T (|\mathbf{x}_i \mathbf{x}_i^T| - \mathbf{x}_i \mathbf{x}_i^T) \mathbf{c}. \end{aligned} \quad (6.4)$$

Note that  $S_i$  is null if  $\mathbf{c}$  is unable to actuate the corresponding  $i$ -th task-space DOF in both directions. The objective is to maximize the function  $S$ , which is a weighted sum<sup>9</sup> of sensitivity magnitudes for all task-space DOFs:

$$S = 4 \sum_{i=1}^{n_t} w_i S_i = \mathbf{c}^T \mathbf{Q} \mathbf{c}, \quad \mathbf{Q} = \sum_{i=1}^{n_t} w_i (|\mathbf{x}_i \mathbf{x}_i^T| - \mathbf{x}_i \mathbf{x}_i^T), \quad (6.5)$$

---

<sup>8</sup>  $\frac{1}{4}$  term scales down the value to compensate for the doubling affect in (6.3)

<sup>9</sup> The constant 4 negates the term  $\frac{1}{4}$  in equation (6.4)

where the weights  $w_i$  express the importance of the corresponding DOF. Note that in the case of a modular structure composed of the simplex cells we can choose different weights for each cell of the structure based on the preferred deformation we want to obtain. The optimal actuator placement vector for a given number of actuators  $n_a$  is then

$$\mathbf{c}_{\text{opt}} = \arg \max_{\mathbf{c}} \mathbf{c}^T \mathbf{Q} \mathbf{c}, \quad \|\mathbf{c}\|_1 = n_a. \quad (6.6)$$

Note that Figure 36 tells us that because the simplex cell topology is twisted either right-handedly or left-handedly, it has poor z-rotation properties in the opposite direction. This problem can be solved by stacking two cells of opposite twist directions on top of each other and balance out the rotation accordingly. The implementation was done with weights specified in Table 11 and Figure 37 shows the cost function value for different quantities of actuators  $n_a$ . One can identify that the balanced sensitivity is increasing monotonically with number of actuators.

*Table 11: Task-space weights used for optimization*

DOF	x-tilt	y-tilt	z-rot	x-shear	y-shear	z-extension
Weight	10	10	5	1	1	10

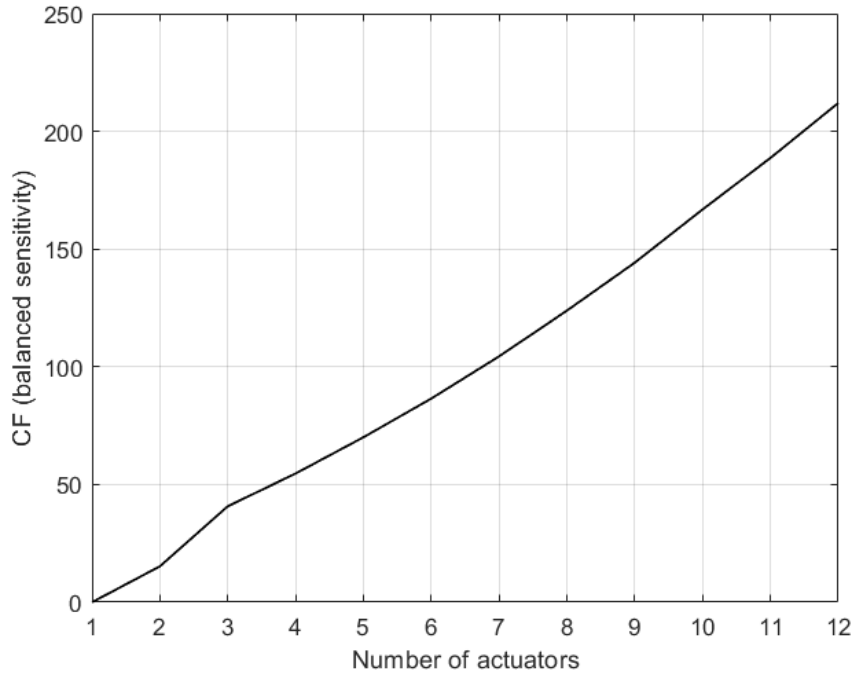


*Figure 37: Cost function variation over possible numbers of actuators*

For each  $n_a$  the best placement of actuators was found using the genetic algorithm and the Matlab® software. In agreement with section 7.5.2, the placements of 3 and 6 actuators are shown in Figure 38 and Figure 39. One can see that for three actuators the optimal placement is coincident with diagonal cables of the simplex.

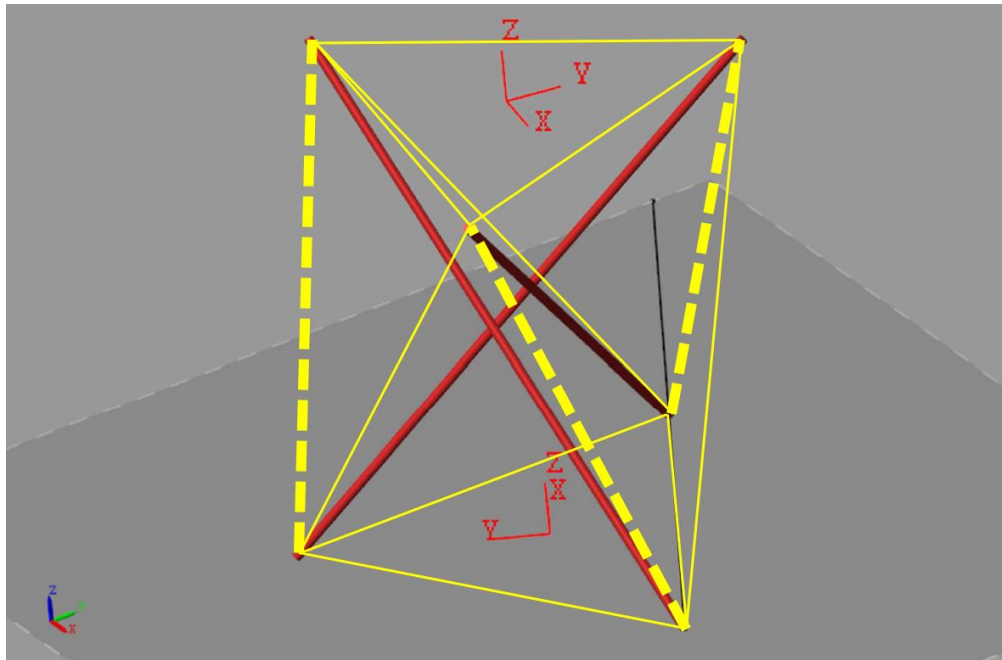


*Figure 38: Optimal large-displacement actuator placement for 3 actuators (actuated cables are dashed)*

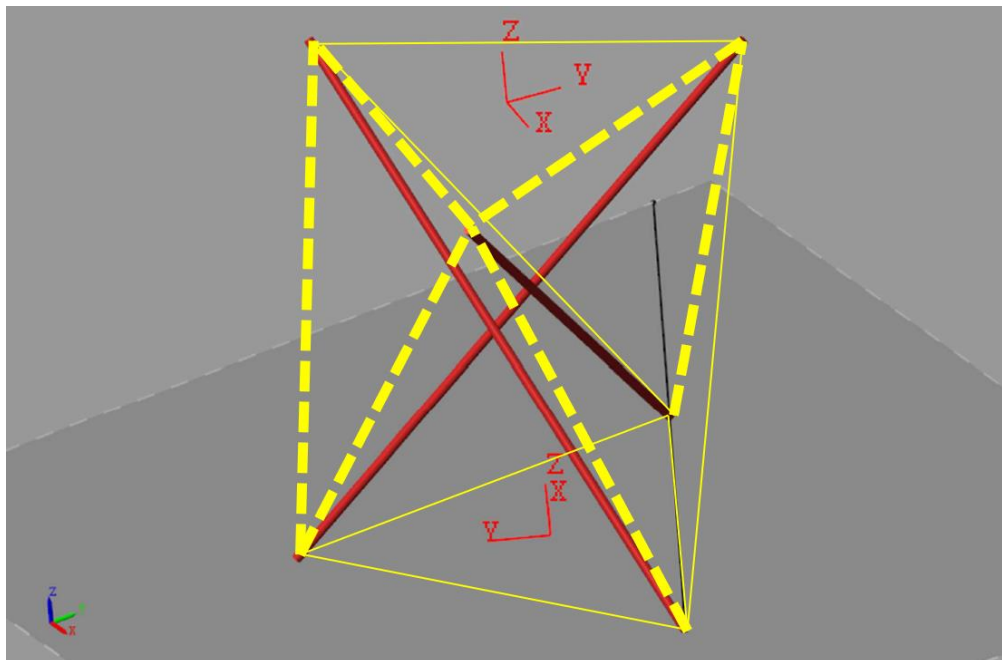


*Figure 39: Optimal large-displacement actuator placement for 6 actuators (actuated cables are dashed)*

## 7 Actuator and Sensor Placement for Active Vibration Suppression

In active vibration suppression, a mere focus on the control algorithm with neglected consideration of a suitable sensor and actuator placement results in a sub-optimal solution. As illustrated on the example of a simply supported beam in Figure 40, the collocated actuator/sensor pair is placed optimally for the first mode. However, the second mode, and all even modes for that matter, are uncontrollable and unobservable by the actuator, resulting in poorly damped vibrations of these modes. For this reason, it is of a substantial importance to address this issue early in the design process, so that the desired control performance is achieved. In this work, an optimal placement of sensors and actuators for a generic tensegrity structure is proposed. The optimization algorithm is based on the derived finite-element dynamic model combined with the Simscape Multibody® software.

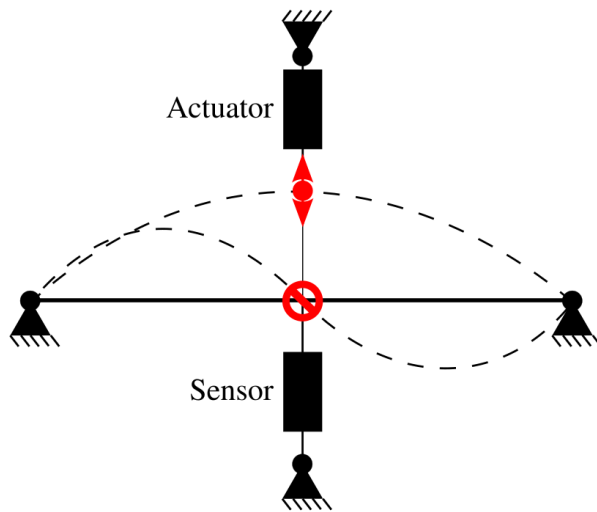


Figure 40: Controllability and observability of a simply supported beam

### 7.1 FEM Model of Tensegrity Structure

Let us have the following dynamic model of the tensegrity structure linearized around operating point  $k$

$$\mathbf{M}(k)\ddot{\mathbf{q}} + \mathbf{B}(k)\dot{\mathbf{q}} + \mathbf{K}(k)\mathbf{q} = \mathbf{J}_a(k)\mathbf{f}_a \quad (7.1)$$

where  $\mathbf{M}$ ,  $\mathbf{B}$ ,  $\mathbf{K}$  and  $\mathbf{J}_a$  are the global mass, damping, stiffness, and actuation force Jacobian matrices, respectively, linearized around operating point  $k$ , and  $\mathbf{q}$ ,  $\mathbf{f}_a$  are the vectors of independent generalized coordinates (IGCs) and actuator forces, respectively. Modal transformation then yields

$$\ddot{\boldsymbol{\alpha}} + \Delta(k)\dot{\boldsymbol{\alpha}} + \Omega^2(k)\boldsymbol{\alpha} = \Phi^T(k)\mathbf{J}_a(k)\mathbf{f}_a \quad (7.2)$$

where  $\boldsymbol{\alpha}$  is the modal coordinate vector, and  $\Delta$ ,  $\Omega^2$  and  $\Phi^T$  are the modal damping matrix, spectral matrix, and modal matrix, respectively, obtained from the linearized models around operating point  $k$ . Further we will neglect the operating point notation “( $k$ )” for clarity. Note that the modal matrix satisfies the mass-weighted orthogonality condition  $\Phi^T \mathbf{M} \Phi = \mathbf{I}$ . The global system matrices are assembled

$$\mathbf{M} = \Pi \sum_{e=1}^{n_e} (\Psi_e \mathbf{M}_e \Psi_e^T) \Pi^T, \quad (7.3)$$

$$\mathbf{K} = \Pi \sum_{e=1}^{n_e} (\Psi_e \mathbf{K}_e \Psi_e^T) \Pi^T, \quad (7.4)$$

where the assemblage<sup>10</sup> matrices  $\Psi_e$  and  $\Pi$  are defined as follows:

$$\Psi_e = \begin{bmatrix} \mathbf{0}_{a \times 6} \\ \mathbf{I}_6 \\ \mathbf{0}_{b \times 6} \end{bmatrix}, a = 6(e-1), b = 6(n_e - e), \quad (7.5)$$

$$\Pi: \Pi(3j + \langle -2, 0 \rangle, 6(e-1) + 3i + \langle -2, 0 \rangle) = \mathbf{I}_3, \quad (7.6)$$

$$\sum_i (\Pi)_{ij} = 1 \quad \forall j, \quad \sum_j (\Pi)_{ij} = n_{ej}, \quad (7.7)$$

where  $i$ ,  $j$  and  $e$  are the indices according to Table 12,  $n_e$  and  $n_{ej}$  are the total number of elements and the number of elements coinciding with the node  $j$ , respectively. The form of matrix  $\Psi_e$  displayed in Figure 41 then results in the following intermediary matrix  $\sum_{e=1}^{n_e} (\Psi_e \mathbf{M}_e \Psi_e^T)$ , which clarifies the role of matrix  $\Pi$ . The function thereof is to describe which local node  $i$  of element  $e$  corresponds to the global node  $j$  according to the

---

<sup>10</sup> A process of assembling global system matrices from the local matrices of the elements through association of local and global nodes [58].

incidence table as displayed in Table 12. The same diagonalizing relation holds for the elemental stiffness matrices  $\mathbf{K}_e$ .

Table 12: FEM incidence table ( $j_{ei}$  is the global node number of the local node  $i$  of element  $e$ )

$e \backslash i$	1	2
1	$j_{11}$	$j_{12}$
2	$j_{21}$	$j_{22}$
$\vdots$	$\vdots$	$\vdots$
$n_e$	$j_{n_e 1}$	$j_{n_e 2}$

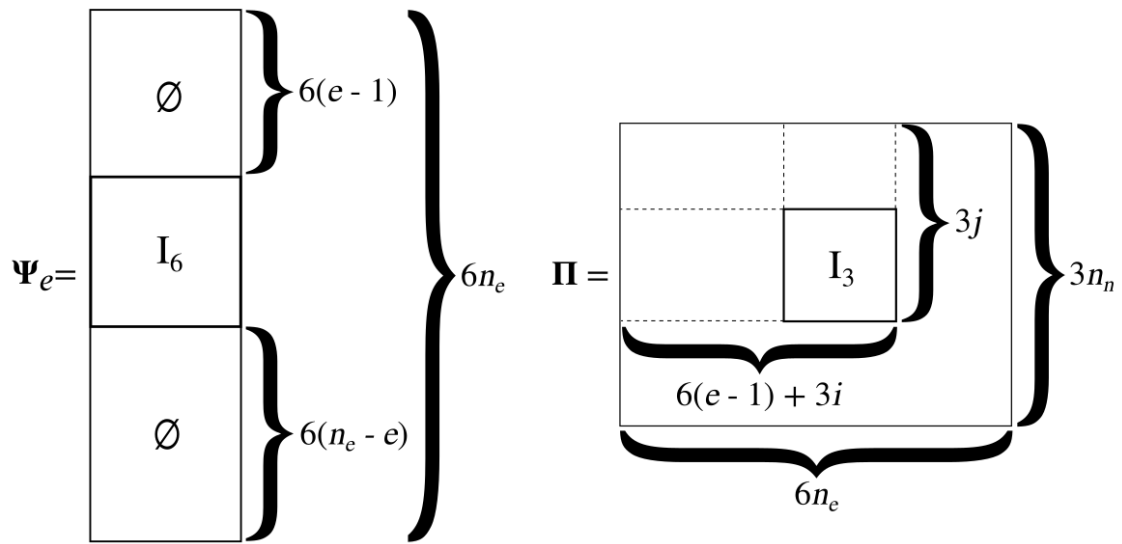


Figure 41: Structure of the assemblage matrices of the FEM model

The elemental mass and stiffness matrices of uniaxial elements with 6 DOF are defined according to [42] as

$$\mathbf{M}_e = m_e \begin{bmatrix} 2\mathbf{I}_3 & -\mathbf{I}_3 \\ -\mathbf{I}_3 & 2\mathbf{I}_3 \end{bmatrix} \quad (7.8)$$

$$\mathbf{K}_e = \frac{k_s^e}{l^e} \left\{ \mathbf{h}^{eT} \mathbf{h}^e + \frac{\Delta l^e + \Delta l_0^e}{l_0^e} [\mathbf{R} \mathbf{R}^T - (\mathbf{R} \mathbf{r}^e)(\mathbf{R} \mathbf{r}^e)^T] \right\}, \quad (7.9)$$

where  $k_s^e$ ,  $l^e$ ,  $l_0^e$ ,  $\Delta l^e$  and  $\Delta l_0^e$  are the element specific stiffness, length, free length, longitudinal deformation and its initial prestressing elongation, respectively, and  $\mathbf{h}^e = [-c_1 \ -c_2 \ -c_3 \ c_1 \ c_2 \ c_3]^T$  is the geometric projection vector of directional

cosines,  $\mathbf{R} = [-\mathbf{I}_3 \quad \mathbf{I}_3]$ ,  $\mathbf{r}^e = [c_1 \quad c_2 \quad c_3]$  and  $c_1, c_2, c_3$  are  $\cos \alpha, \cos \beta$  and  $\cos \gamma$ , respectively, according to Figure 42.

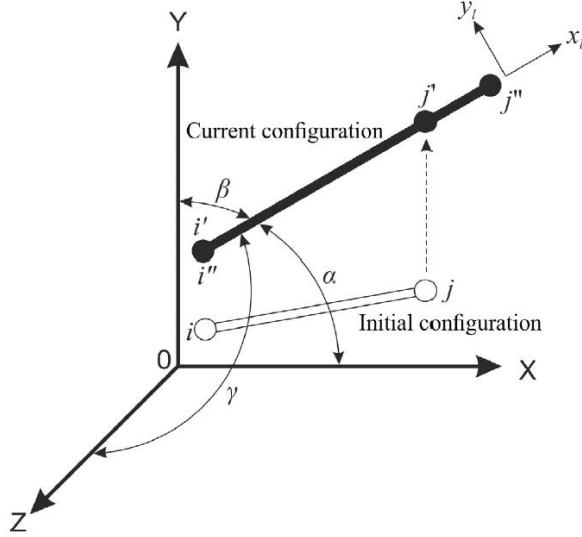


Figure 42: Axial element in initial and final configuration [43]

## 7.2 Force Jacobians

In this section, we express the sensor forces for the entire system. Since the elements in our case are spherically constrained bars and cables, let us express the internal element force as a uniaxial force

$$f_e = \frac{k_s^e \Delta l^e}{l_0^e} + k_s^e \varepsilon_0, \quad (7.10)$$

which after variation leads to

$$\delta f^e = \frac{k_s^e}{l_0^e} \delta \Delta l^e = \frac{k_s^e}{l_0^e} \mathbf{h}^e \delta \mathbf{d}^e, \quad (7.11)$$

where  $\mathbf{d}^e = [u_i^e \quad v_i^e \quad w_i^e \quad u_j^e \quad v_j^e \quad w_j^e]^T$  is the vector of nodal displacements. When expanded to all elements in the global coordinate frame, we obtain

$$\delta \mathbf{f} = \mathbf{K}_s \mathbf{L}_0^{-1} \mathbf{J}_s \delta \mathbf{q} \quad (7.12)$$

where  $\mathbf{K}_s$ ,  $\mathbf{L}_0$  and  $\mathbf{J}_s$  are the diagonal matrix of specific elemental stiffnesses, the diagonal matrix of inverse element lengths and the sensing force Jacobian, respectively. When

assuming only cable placements of sensors and identical specific stiffnesses across all cables, we can simplify

$$\delta \mathbf{f} = k_s^c \mathbf{L}_0^{-1} \mathbf{J}_s \delta \mathbf{q}. \quad (7.13)$$

The sensing force Jacobian is then defined as

$$\mathbf{J}_s = \mathbf{S}_s \mathbf{H}^T \boldsymbol{\Pi}^T \quad (7.14)$$

where the sensor placement matrix

$$\mathbf{S}_s := R_r(\text{diag}(\mathbf{s})), \quad s_e := \begin{cases} 1, & \text{if element } e \text{ is sensed,} \\ 0, & \text{otherwise,} \end{cases} \quad (7.15)$$

where  $R_r$  represents an empty-row-removal operator and  $\mathbf{H}^T$  is a diagonal block matrix of projection vectors

$$\mathbf{H}^T = \begin{bmatrix} -\mathbf{h}_1 - & 0 & \cdots & 0 \\ 0 & -\mathbf{h}_2 - & & \vdots \\ \vdots & & & 0 \\ 0 & \cdots & 0 & -\mathbf{h}_{n_e} - \end{bmatrix} \quad (7.16)$$

The actuation force Jacobian has the following form:

$$\mathbf{J}_a = \boldsymbol{\Pi} \mathbf{H} \mathbf{S}_a \quad (7.17)$$

where the actuator placement matrix

$$\mathbf{S}_a := R_c(\text{diag}(\mathbf{a})), \quad a_e := \begin{cases} 1, & \text{if element } e \text{ is actuated,} \\ 0, & \text{otherwise,} \end{cases} \quad (7.18)$$

where  $R_c$  represents an empty-column-removal operator.

### 7.3 State-space Representation

At last, we can now express the dynamics in the almost-balanced modal state-space form [44]:

$$\begin{aligned}\dot{\mathbf{x}} &= \mathbf{Ax} + \mathbf{Bu}, \\ \mathbf{y} &= \mathbf{Cx},\end{aligned}\tag{7.19}$$

where the system vectors and matrices are defined as

$$\mathbf{x} = \begin{bmatrix} \Omega \alpha \\ \dot{\alpha} \end{bmatrix}, \mathbf{u} = \mathbf{f}_a, \mathbf{y} = \mathbf{f}_s, \tag{7.20}$$

$$\begin{aligned}\mathbf{A} &= \begin{bmatrix} \mathbf{0} & \Omega \\ -\Omega & -\Delta \end{bmatrix}, \\ \mathbf{B} &= \begin{bmatrix} \mathbf{0} \\ \Phi^T \mathbf{J}_a \end{bmatrix}, \\ \mathbf{C} &= [k_s^c \mathbf{L}_0^{-1} \mathbf{J}_s \Phi \Omega^{-1} \quad \mathbf{0}].\end{aligned}\tag{7.21}$$

## 7.4 Optimality Criterions

The optimization of actuator and sensor placements for the vibration control is based on the maximization of certain controllability and observability criterions called the degree of controllability (DEGC) and the degree of observability (DEGO). These criterions are derived from the controllability and observability Gramians according to [45]. In appendix A, the Gramians of a simple tensegrity structure are analytically derived for clarity.

### 7.4.1 Degree of Controllability

For the actuator placement, a suitable objective is the minimization of control energy required to bring the system eigenmodes to the desired states after a certain time  $t$ . This can be expressed by the quadratic form

$$J_c = \int_0^t \mathbf{u}^T(\tau) \mathbf{u}(\tau) d\tau. \tag{7.22}$$

It can be shown that minimizing  $J_c$  with respect to actuator locations corresponds to the maximization of the measure of the controllability Gramian

$$\mathbf{W}_c(t) = \int_0^t e^{\mathbf{A}\tau} \mathbf{B} \mathbf{B}^T e^{\mathbf{A}^T \tau} d\tau. \tag{7.23}$$

It was shown that the controllability Gramian tends to a diagonal form for steady state when damping ratios  $\zeta_i$  are close to zero [46], corresponding to our notion of poor

damping in the infinitesimal mechanism directions. Hence, we can rewrite the expression for the  $i$ -th diagonal element of the controllability Gramian matrix

$$(\mathbf{W}_c)_{2i-1,2i-1} = (\mathbf{W}_c)_{2i,2i} = \sum_{j=1}^{n_a} \frac{b_{ij}^2}{4\zeta_i \Omega_i}, \quad (7.24)$$

where  $n_a$  and  $\Omega_i$  are the number of actuators and the  $i$ -th eigenfrequency, respectively, and  $b_{ij} = (\mathbf{B})_{n+1,j}$  where  $n$  is the number of DOF. The term  $(\mathbf{W}_c)_{ii}$  describes the modal controllability, in other words, what velocity can a mode obtain from a unit force per unit mass. This then corresponds to the transferable energy from the actuators to the  $i$ -th mode of the structure. Thus, if the  $i$ -th eigenvalue of  $(\mathbf{W}_c)_{ii}$  is small, the mode is difficult to control and will require more force to be controlled to the same extent as the modes with larger eigenvalues. In [45] a normalized optimality criterion accounting for the least controllable mode was proposed. The criterion here will be used without considering the residual modes

$$DEGC_{n_a}(\mathbf{a}) = \min_i \frac{\sum_{j=1}^{n_a} b_{ij}(\mathbf{a})^2}{\max_{\mathbf{a}} \sum_{j=1}^{n_a} b_{ij}(\mathbf{a})^2}, \quad \|\mathbf{a}\|_1 = n_a, \quad (7.25)$$

where  $n_a$  is the number of actuators and  $\mathbf{a}$  is the actuator placement vector. This criterion corresponds to the minimal diagonal component of  $(\mathbf{W}_c)_{ii}$  and since  $(\mathbf{W}_c)_{ii}$  tends to diagonal form, this value is proportional to the smallest principal component of the aforementioned Gramian matrix. For our case, the criterion is expanded to account for the different linearization operating points

$$DEGC_{n_a}(\mathbf{a}) = \min_i \frac{\sum_{k=1}^{n_{op}} \sum_{j=1}^{n_a} b_{ijk}(\mathbf{a})^2}{\max_{\mathbf{a}} \sum_{k=1}^{n_{op}} \sum_{j=1}^{n_a} b_{ijk}(\mathbf{a})^2}, \quad \|\mathbf{a}\|_1 = n_a. \quad (7.26)$$

This normalized criterion then represents the transferable mechanical energy for the  $i$ -th mode divided by its maximum receivable energy across all possible actuator placement configurations, hence  $DEGC_{n_a}(\mathbf{a}) \in \langle 0,1 \rangle$ .

#### 7.4.2 Degree of Observability

For the placement of sensors, we seek an arrangement that maximizes the output energy of the system in the form

$$J_0 = \int_0^\infty \mathbf{y}^T(\tau) \mathbf{y}(\tau) d\tau \quad (7.27)$$

for the desired modes. In [46] it was shown that this criterion corresponds to maximizing a certain norm of the observability Gramian (when system is released from the initial state and subjected to a persistent disturbance)

$$\mathbf{W}_o(t) = \int_0^t e^{A^T \tau} \mathbf{C}^T \mathbf{C} e^{A \tau} d\tau. \quad (7.28)$$

It was also shown that for a displacement output with well-spaced eigenfrequencies the Gramian tends to diagonal form

$$(\mathbf{W}_o)_{2i-1,2i-1} = (\mathbf{W}_o)_{2i,2i} = \sum_{j=1}^{n_s} \frac{c_{ji}^2}{4\zeta_i \Omega_i}, \quad (7.29)$$

where  $c_{ji} = (\mathbf{C})_{ji}$ . The term  $(\mathbf{W}_o)_{ii}$  describes the modal observability, in other words, what force can a sensor obtain from a unit displacement at a given frequency. This then corresponds to the transferable energy to the sensors from the  $i$ -th mode of the structure. Thus, if the  $i$ -th eigenvalue of  $(\mathbf{W}_o)_{ii}$  is small, the mode is difficult to observe and will require more displacement to be observed to the same extent as the modes with larger eigenvalues.

In [45] a normalized optimality criterion accounting for the least observable mode has been proposed. The criterion here will be used without considering the residual modes

$$DEGO_{n_s}(\mathbf{s}) = \min_j \frac{\sum_{i=1}^{n_s} c_{ij}(\mathbf{s})^2}{\max_{\mathbf{s}} \sum_{i=1}^{n_s} c_{ij}(\mathbf{s})^2}, \quad \|\mathbf{s}\|_1 = n_s, \quad (7.30)$$

where  $n_s$  is the number of sensors and  $\mathbf{s}$  is the sensor placement vector. This criterion corresponds to the least diagonal component of  $(\mathbf{W}_o)_{ii}$  and since  $(\mathbf{W}_o)_{ii}$  tends to diagonal form, this value is proportional to the smallest principal component of the aforementioned Gramian matrix. For our case, the criterion is expanded to account for different linearization operating points

$$DEGO_{n_s}(\mathbf{s}) = \min_i \frac{\sum_{k=1}^{n_{op}} \sum_{i=1}^{n_s} c_{ijk}(\mathbf{s})^2}{\max_{\mathbf{s}} \sum_{k=1}^{n_{op}} \sum_{i=1}^{n_s} c_{ijk}(\mathbf{s})^2}, \quad \|\mathbf{s}\|_1 = n_s. \quad (7.31)$$

This normalized criterion then represents the measurable output energy for the  $j$ -th mode divided by its maximum measurable output energy across all possible sensor placement configurations, hence  $DEGO_{n_s}(\mathbf{s}) \in \langle 0,1 \rangle$ .

### 7.4.3 Degree of Balanced Interaction

In active vibration suppression the collocated control is used frequently. For this reason, the placement of sensors and actuators is identical. Therefore, we cannot optimize the placements separately. Our task in this section is to find an optimality criterion suitable for the collocated placement. Ideally, with the same sensor and actuator placement, further referred to as the balanced interaction placement, we would like to minimize the control energy and maximize the output energy of the system simultaneously. This then translates to the maximization of both controllability and observability Gramians. A well-known balancing transformation [47] will come of use here. It describes a special state coordinate transformation  $\mathbf{T}$  which results in

$$\hat{\mathbf{W}}_c = \hat{\mathbf{W}}_o = \Sigma \quad (7.32)$$

where  $\Sigma$  is a diagonal matrix of Hankel singular values,  $\hat{\mathbf{W}}_c = \mathbf{T}^{-1} \mathbf{W}_c \mathbf{T}^{-H}$ , and  $\hat{\mathbf{W}}_o = \mathbf{T}^H \mathbf{W}_o \mathbf{T}$ , where  $( )^H$  is the Hermitian transpose. We obtain  $\mathbf{T}$  by solving a generalized spectral decomposition problem

$$\mathbf{W}_c \mathbf{W}_o \mathbf{T} = \mathbf{T} \Sigma^2 \quad (7.33)$$

or an equivalent principal component analysis (PCA) problem. We have now obtained a diagonal matrix representing controllability and observability of an internally-balanced state-space model

$$\tilde{\mathbf{A}} = \mathbf{T} \mathbf{A} \mathbf{T}^{-1}, \quad \tilde{\mathbf{B}} = \mathbf{T} \mathbf{B}, \quad \tilde{\mathbf{C}} = \mathbf{C} \mathbf{T}^{-1}. \quad (7.34)$$

Note that this matrix is generally different for each linearization operating point  $k$ . The optimal interaction placement for the collocated case is then

$$\mathbf{p}^* = \arg \max_{\mathbf{p}} \min_i \frac{\sum_{k=1}^{n_{op}} \sigma_{ki}}{\max_{\mathbf{p}} \sum_{k=1}^{n_{op}} \sigma_{ki}}, \quad \|\mathbf{p}\|_1 = n_{sa}, \quad (7.35)$$

where  $n_{sa}$  is the number of sensors or actuators,  $\sigma_{ki} = (\Sigma_k)_{ii}$  and  $\mathbf{p}$  is the placement vector such that

$$\mathbf{p}_e := \begin{cases} 1, & \text{if element } e \text{ is actuated and sensed,} \\ 0, & \text{if element } e \text{ is neither actuated nor sensed.} \end{cases} \quad (7.36)$$

Further, in the collocated case

$$\mathbf{a} = \mathbf{s} = \mathbf{p}. \quad (7.37)$$

The criterion to be maximized here can be interpreted as the smallest principal component of balanced Gramians across multiple operating points. This approach provides an optimization scheme which exactly balances actuator and sensor placements and makes them equivalent. However, due to heavy computational burden, especially when computing  $\max_{\mathbf{p}} \sum_{k=1}^{n_{op}} \sigma_{ki}$ , the author decided to utilize an almost-balanced form of state space model instead, providing a sufficient approximation to produce relevant results, yet with significantly less computational effort [44].

## 7.5 Implementation

A specific example of tensegrity structure has been developed [33]. It is a tensegrity tower with two stages of second order, which implies that two struts are connected at most within the structure. In our case the struts are connected in pairs with spherical joints between the stages. The nodes are fully connected with cables. We can divide the cables in three groups based on their orientation: *vertical*, *horizontal*, and *diagonal*. Figure 43 shows the geometrical model of the tower which was used in FEM modelling and the following optimization. The optimization of the low-authority actuator and sensor placement for active vibration suppression was implemented in Matlab® and the corresponding code can be found according to appendix C. The placement of sensors and

actuators was considered in cables only. The model is considered to have 18 DOF in total including the strut axial deformation and excluding the strut parasitic rotation, which is neglected in this case. This consequently results in 18 modelled vibrational modes.

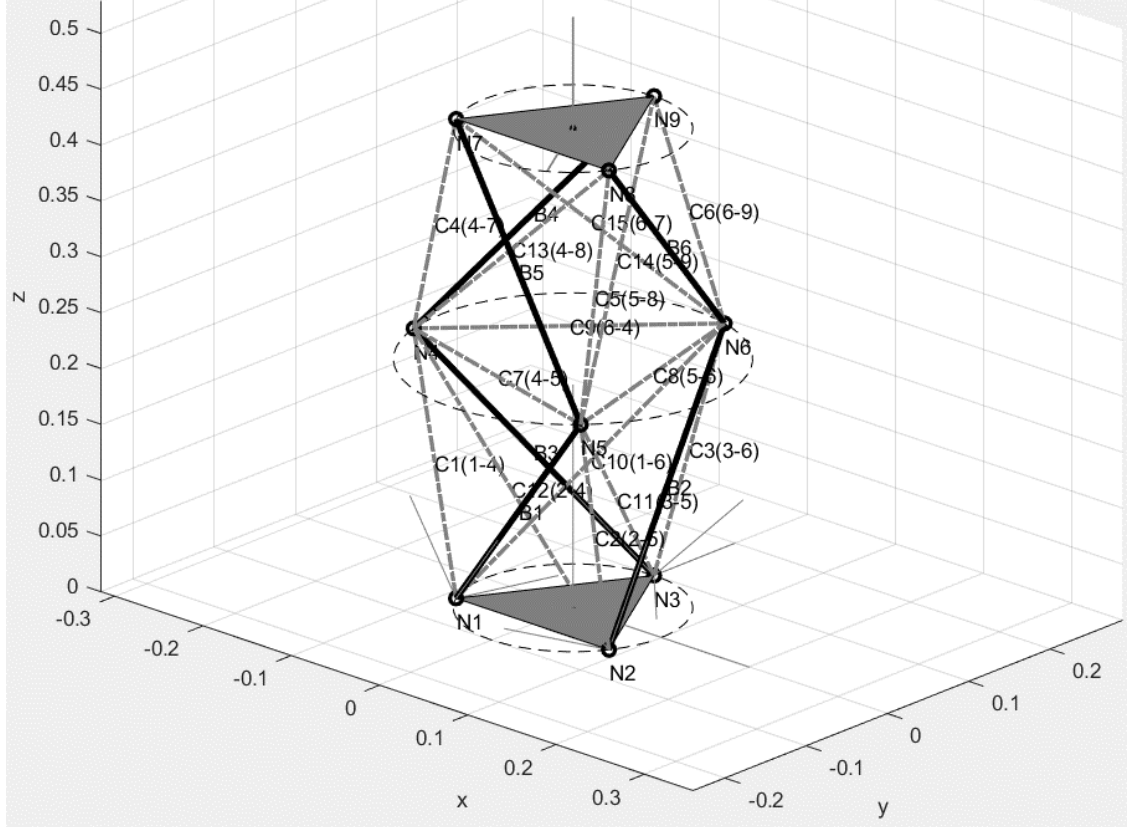


*Figure 43: 2-stage tensegrity tower of type-2 with fully connected nodes and a top platform. The struts are shown with a black solid line and cables with a purple dashed line. Nodes are labelled  $N_x$ , struts (bars) are labelled  $B_x$ , and cables  $C_x(y-z)$ , where  $x$  is the number of the node/element and  $y-z$  are the connected node numbers. Axes are measured in meters. [33]*

The optimization variables are the sensor placement vector according to (7.15) and the actuator placement vector according to (7.18). These are Boolean vectors of length identical with the number of cables, for all cables are allowed for the placement. Because of the Boolean nature, genetic algorithm was used for optimization. The basic optimization options selected for the algorithm are specified in Table 13. The two objective functions used for optimization are the degrees of controllability and observability as defined in sections 7.4.1 and 7.4.2. Maximizing these scalar functions yielded following results: quantitative and qualitative.

*Table 13: User-specified optimization options*

Optimization option	Value	Type
Algorithm	Genetic algorithm	
Crossover fraction	0.8	double
Population size	200	integer
Maximum stall generations	5	integer
Function tolerance	1e-6	double

### 7.5.1 Quantitative Optimization Results

They are related to the final value of the objective functions. In Figure 44 a DEGC plot for varying number of actuators is shown. It is displayed for three modes: first, second and the least controllable (indexed in ascending order according to the natural frequency). Because DEGC is computed relative to the maximum value of controllability across all placements, the maximum value will be unity. In Figure 45 the controllability relative to a single actuator is displayed. This plot has a significance for the decision-making purposes, where it serves as a useful tool to determine the used number of actuators to for the application. For example, one can see that for six actuators placed optimally within the structure even the least controllable mode is more controllable than this mode with only one actuator placed optimally to control this mode only. Also, for three actuators the least controllable mode has approximately half the controllability as this mode when only one actuator, placed optimally for this mode only, is used. Figure 46 and Figure 47 show the relative modal observability, which can be explained analogically.

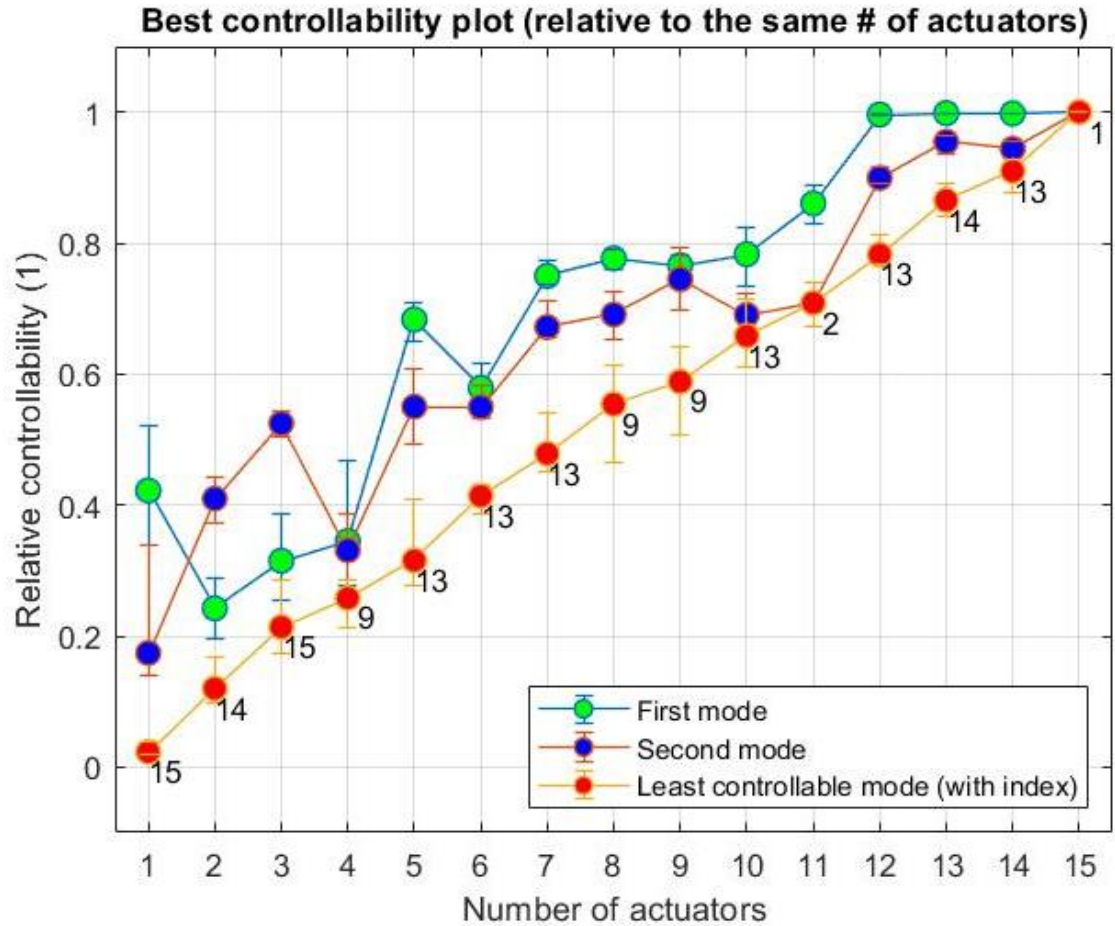


*Figure 44: Best controllability plot relative to the same number of actuators for each possible number of actuators. It is displayed for three different modes, where the relative controllability of the least controllable mode (LCM) is the maximized objective function DEGC. The data points of the LCM are labeled by the index of the mode which is least controllable for the given number of actuators. The error bars describe the scaled-down standard deviation of the data points at different linearization operating points.*

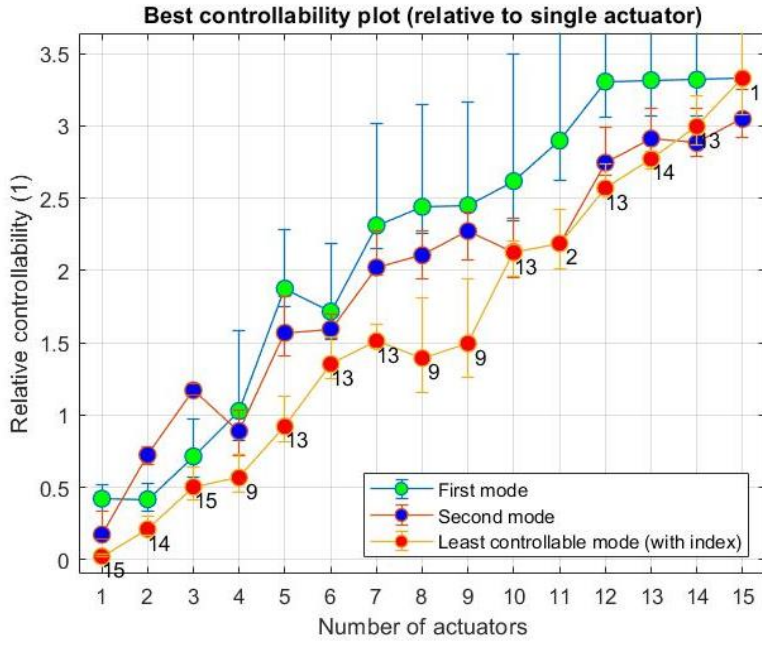


Figure 45: Best controllability plot relative to a single actuator for each possible number of actuators. It is displayed for three different modes. The data points of the LCM are labeled by the index of the mode which is least controllable for the given number of actuators. The error bars describe the scaled-down standard deviation of the data points at different linearization operating points.

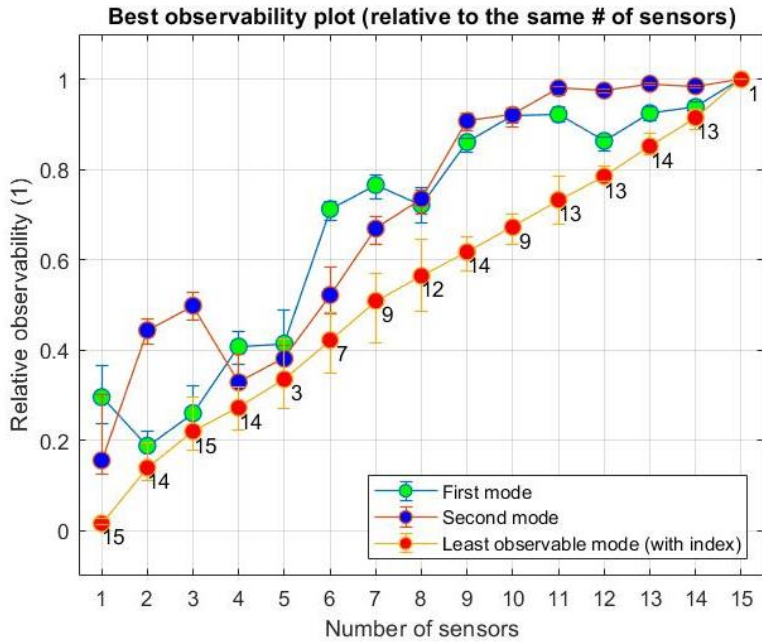


Figure 46: Best observability plot relative to the same number of sensors for each possible number of sensors. It is displayed for three different modes, where the relative observability of the least observable mode (LOM) is the maximized objective function DEGO. The data points of the LOM are labeled by the index of the mode which is least observable for the given number of sensors. The error bars describe the scaled-down standard deviation of the data points at different linearization operating points.

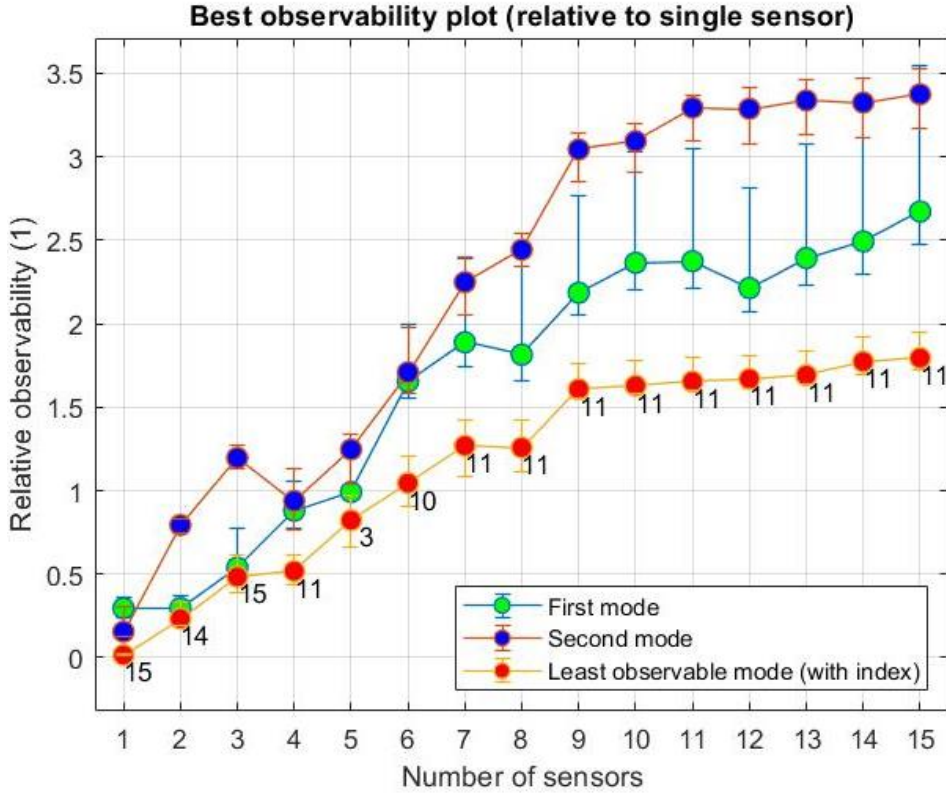


Figure 47: Best observability plot relative to a single sensor for each possible number of sensors. It is displayed for three different modes. The data points of the LOM are labeled by the index of the mode which is least observable for the given number of sensors. The error bars describe the scaled-down standard deviation of the data points at different linearization operating points.

### 7.5.2 Qualitative Optimization Results

Qualitative results correspond to the best possible placement of sensors (actuators) for every number  $n_s$  ( $n_a$ ) of them starting with one and ending with the total number of cables (when there are sensors/actuators present in each cable). As discussed in section 7.2, these placements correspond to the best configurations of Boolean vectors  $\mathbf{a}$  or  $\mathbf{s}$  with the number of “1” (true) components set to  $n_s$  or  $n_a$ , respectively.

As explained in the previous section, the plots in Figure 44-Figure 47 allow us to decide on the number of actuators based on performance. Other factors, however, need to be included as well. In this case, the numbers of sensors and actuators were decided based on Figure 45 and Figure 47. The chosen values were 3 and 6. These numbers were chosen according to the following factors: 1) both are divisible by 3, which is characteristic for the rotational tri-symmetry of the tensegrity tower; 2) with 3 actuators (sensors) which are optimally placed within the structure, even the least controllable (observable) mode

is around half as controllable (observable) as this mode with only one actuator (sensor) optimally placed only for this mode; 3) with 6 actuators (sensors) which are optimally placed within the structure, even the least controllable (observable) mode is more controllable (observable) than this mode with only one actuator (sensor) optimally placed only for this mode. By modifying Figure 43 we can display the placement of sensors and actuators graphically. In Figure 48 one can see the locations of 3 and 6 actuators resulting from the optimal placement optimization, while Figure 49 shows the case for the sensor placement.

An important finding of these results is the fact that the optimal placement is the same for both actuators and sensors, as could one identify from the figures below. This is particularly useful for our case, where collocated sensors and actuators are desired. A total solution would require maximizing the degree of balanced interaction according to section 7.4.3, which is computationally expensive, as mentioned previously. Therefore, the almost-balanced solution offers the same final results while being more efficient.

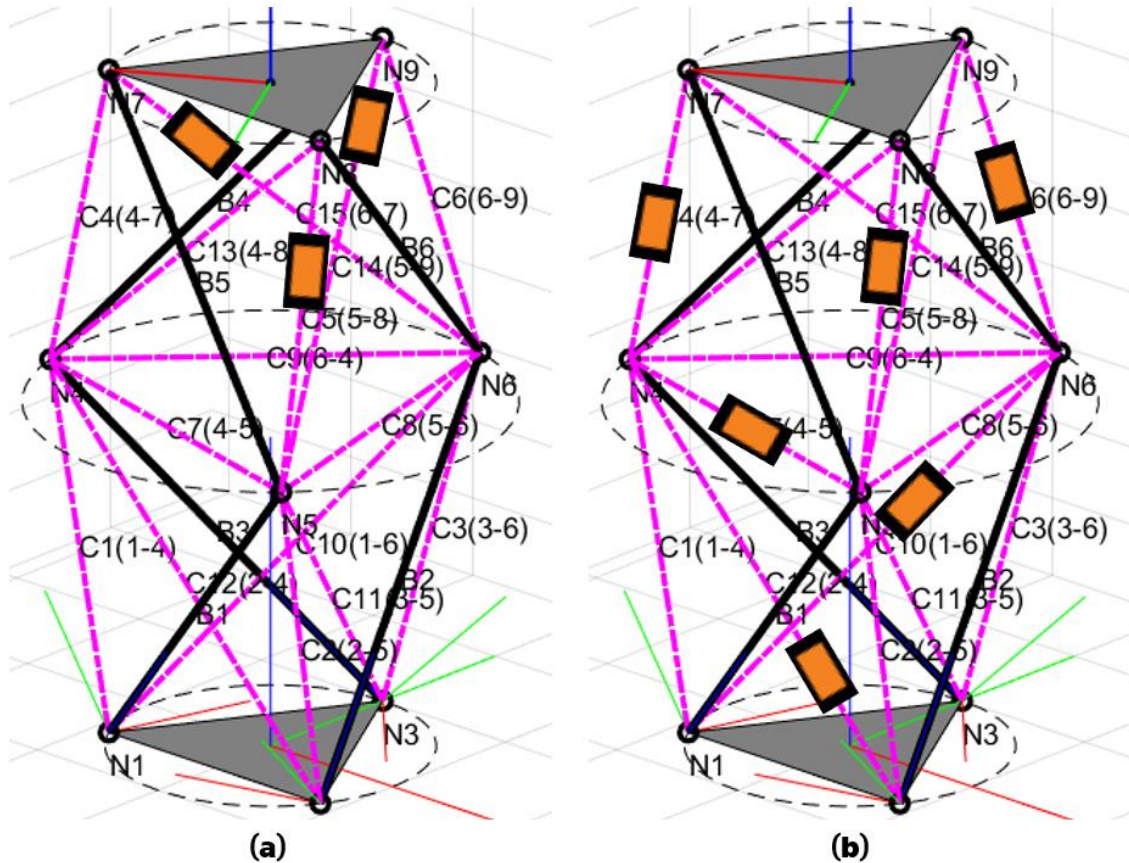


Figure 48: Pictorial representation of actuator placement for: a) 3 actuators; b) 6 actuators

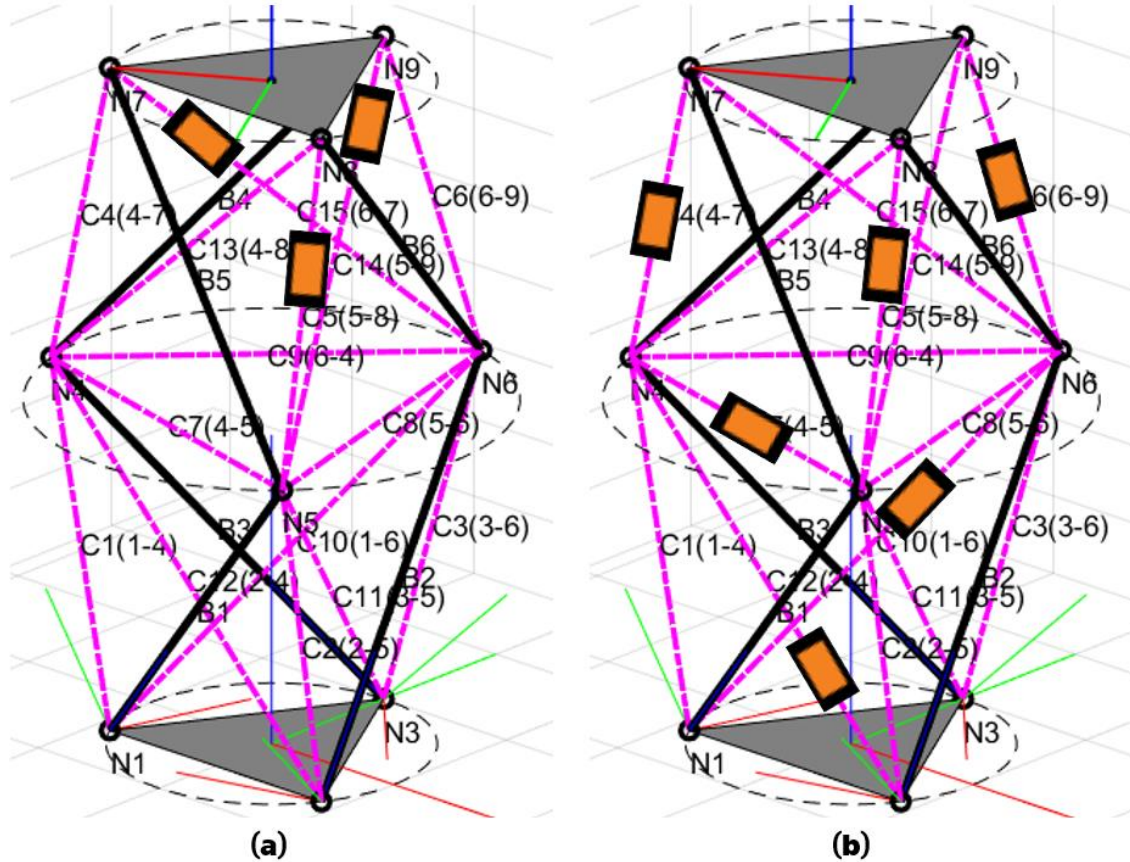


Figure 49: Pictorial representation of sensor placement for: a) 3 sensors; b) 6 sensors

# 8 Active Vibration Suppression Superimposed on Large Motion Control

## 8.1 The Model

For the practical implementation, a 2-stage tensegrity manipulator of type 1, which means that no two struts are connected, was constructed as shown in Figure 50 as a part of the project [33]. This demonstrator consists of two S3 tensegrity simplexes stacked on top of each other while being surrounded by two platforms – a bottom and a top platform. The bottom platform is considered fixed to the world frame (except for kinematic excitations) and the top platform supports the end-effector, which is not shown in the figure. The platforms are attached to the struts by universal joints, eliminating parasitic rotations, otherwise present in spherical joints. In Figure 51 a Simscape Multibody® virtual model of the structure is shown. As one can see, the universal joints and the cables are not displayed graphically.

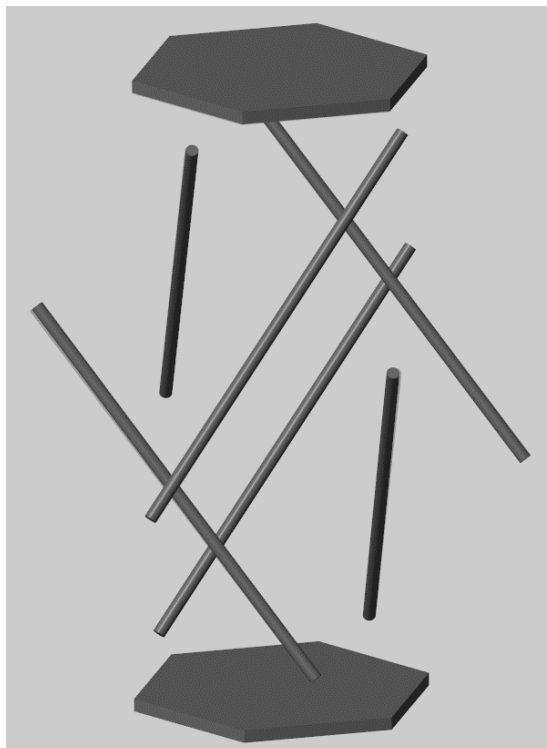
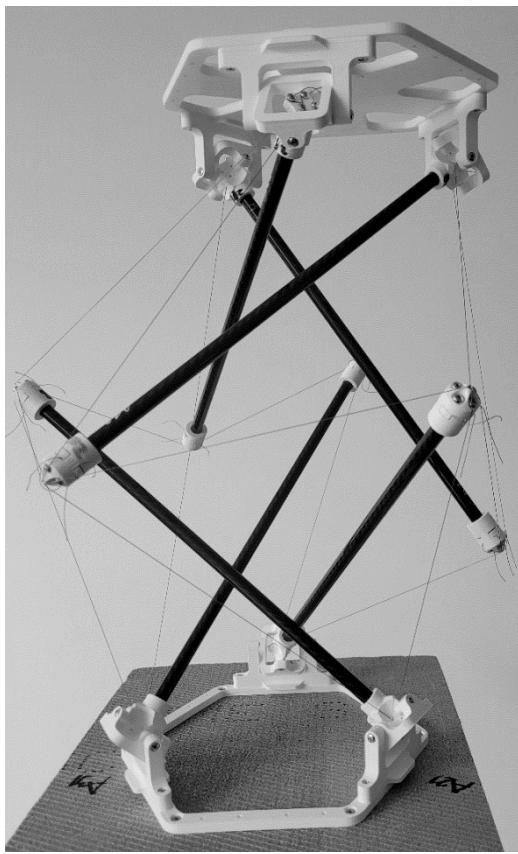


Figure 51: Simscape Multibody® model of the tensegrity manipulator [33]

Figure 50: Physical demonstrator of the 2-stage type-1 tensegrity manipulator [33]

The struts of the demonstrator are made of carbon fiber composite tubes and modelled as rigid round bars of length  $l_s = 360$  mm and diameter  $d_s = 10$  mm. The cables are modelled massless and according to Torayca T700SC-2400 high-strength carbon fiber cable with specific stiffness  $k_s^c = 179 \frac{\text{Nm}}{\text{mm}}$ , as identified in [48], and specific damping  $b_s^c = 17 \frac{\text{Ns}}{\text{m}}$  as specified in [34] as a lower bound, which yields an approximate damping ratio

$$b_{ra} = \frac{b_s^c}{2\sqrt{k_s m_t}} = \frac{17}{2\sqrt{1.79 \cdot 10^5 \cdot 4}} = 0.01 = 1\% \quad (8.1)$$

where  $m_t = 4$  kg is the assumed mass of the structure. The platforms are modelled as hexagonal extrusions of width  $W_p = 205$  mm and thickness  $t_p = 10$  mm. The model has a uniform density  $\rho_m = 2700 \text{ kg} \cdot \text{m}^{-3}$ .

For simulation, control law synthesis, and testing, a specific bending movement pattern was chosen as shown in Figure 52. The figure shows the task-space coordinates of the top platform along the chosen trajectory performed by the manipulator. The trajectory of the manipulator in 3D space is shown in Figure 53. The control of large displacements of the manipulator was produced using the computed torque control (CTC) on which the IFF active vibration control was later superimposed. Figure 54 and Figure 55 display the deviation of the real trajectory from the desired trajectory for the case when only CTC control is used, and no external disturbances are present. Hence, these plots represent the error, dependent only on the intrinsic dynamics of the system and the CTC controller. The gains of the controller are chosen according to Table 14 and can be modified to obtain a desired high-authority control response.

*Table 14: PID gains for the CTC controller*

$K_d$	$K_i$	$K_d$
300	0	0

This iteration aims to assess the interaction of the CTC and the IFF control on different authority levels. For this reason, the placements of actuators for each control law are chosen to be mutually exclusive, meaning there are no two actuators occupying the same cable. Furthermore, the actuator placement for large displacements is chosen such that the set of CTC-active cables is a relative complement of the set of IFF-active cables in

the set of all cables of the structure. Therefore, all cables of the structure are active, either with CTC or IFF actuator. However, an active cable model has also been developed which accounts for both types of actuators in the same cable and the reader can be referred to appendix B for more information.

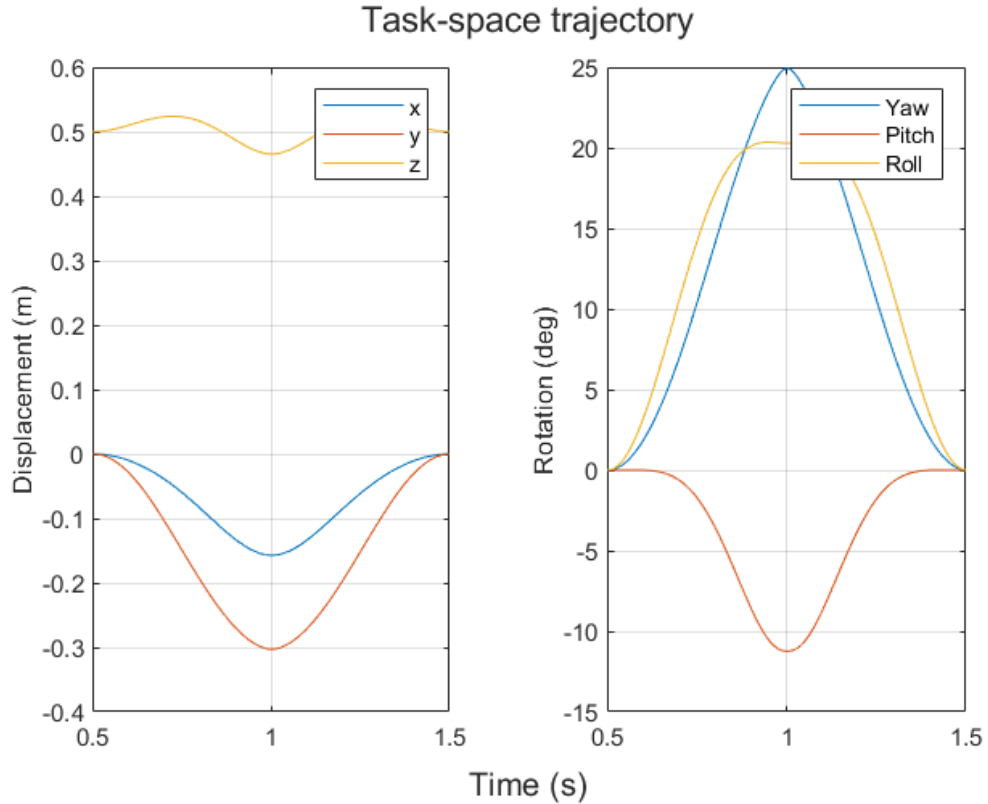
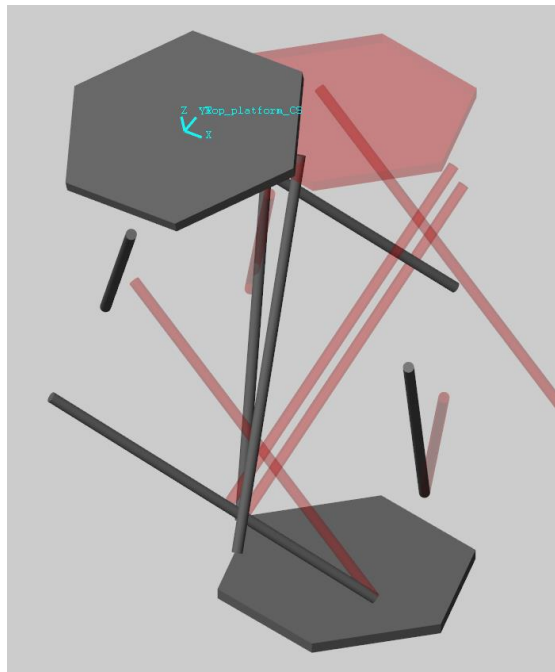


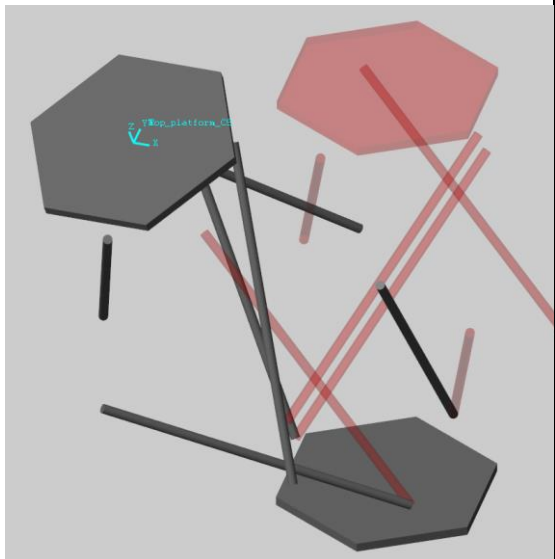
Figure 52: Displacement and rotation time plot of the top platform. The cycle starts at 0.5 s ( $\tau = 0$ ) and lasts  $T = 1$  s.



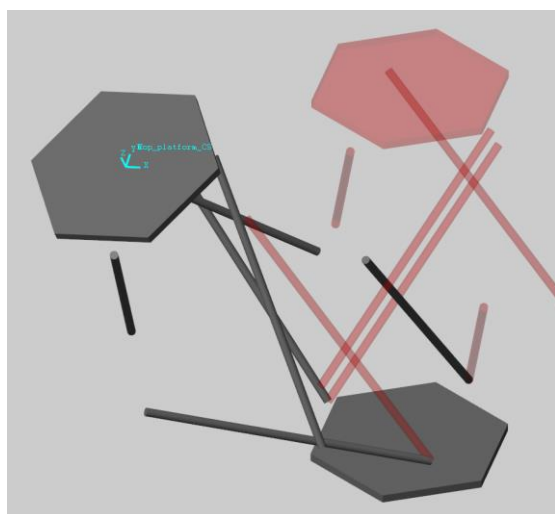
$$\tau = \frac{1}{8}T$$



$$\tau = \frac{2}{8}T$$



$$\tau = \frac{3}{8}T$$



$$\tau = \frac{1}{2}T$$

Figure 53: Manipulator trajectory half-cycle where  $T$  is the period of the trajectory. The starting position is shown in red.

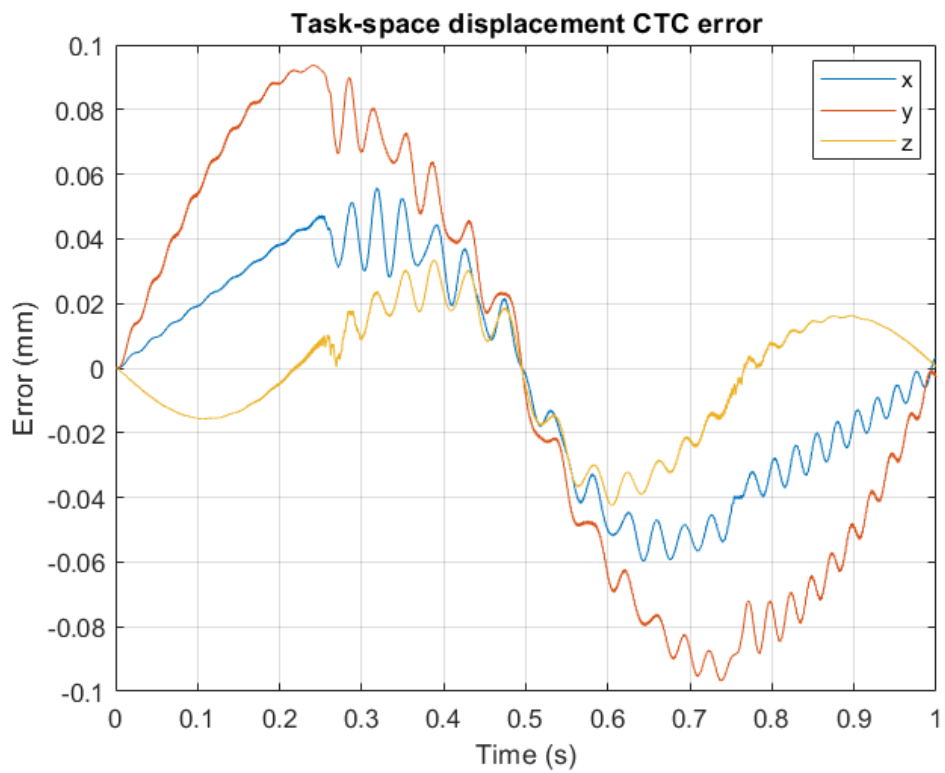


*Figure 54: CTC task-space displacement error plot along the trajectory without disturbances*

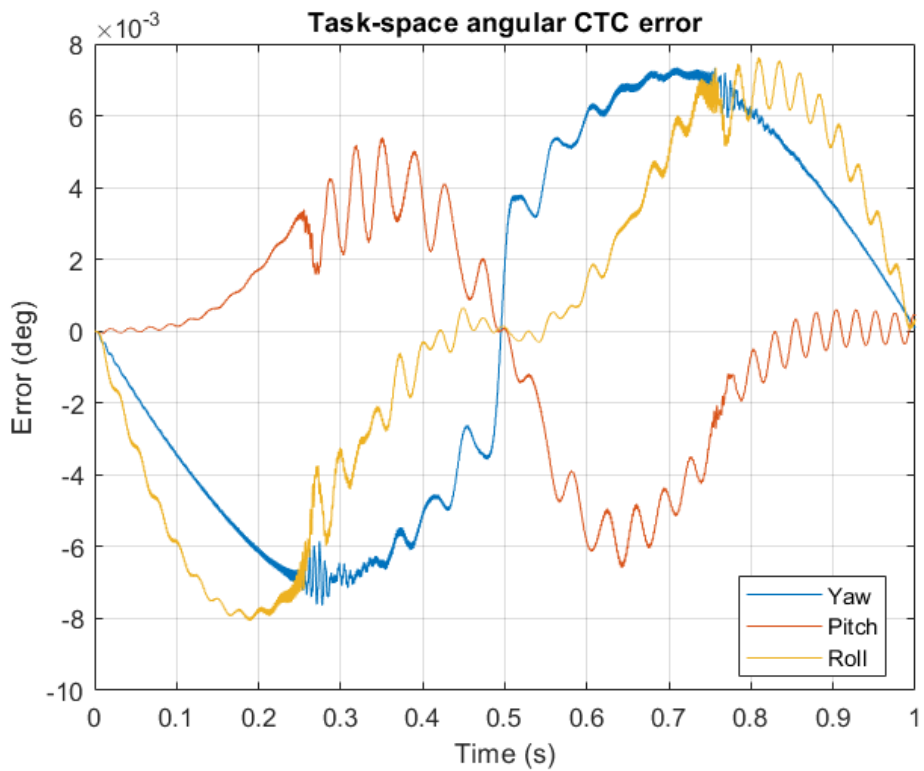


*Figure 55: CTC task-space angular error plot along the trajectory without disturbances*

The vibration-control actuator placement for the simulation purpose was chosen according to Figure 56. For vibration suppression only the mid-level cables are actuated. This type of actuator placement is analogous to the one of the Stewart platform in [49], where the mentioned placement is convenient for the following reasons:

- In default position, cables are almost orthogonal, which results in a diagonally dominant force Jacobian, nearly decoupling the actuator forces.
- Each path between the bottom and the top platform of the manipulator contains at least one active cable, making this configuration suitable for vibration isolation.

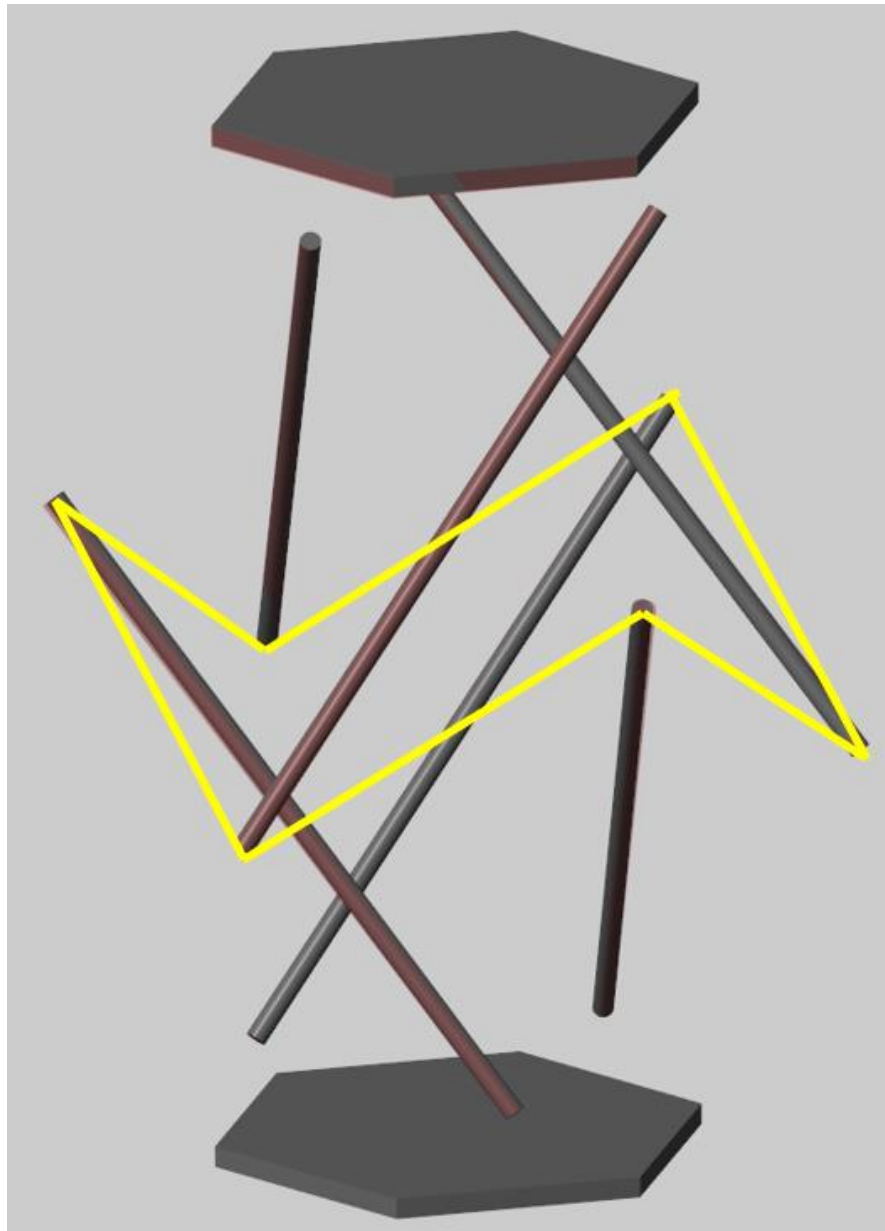


*Figure 56: Tensegrity manipulator use case. Cables actuated for vibration suppression are highlighted in yellow. All other cables are actuated using high-authority control.*

In vibration control only small displacements are considered to enable the use of linear control theory. Two linear plants were considered for the synthesis:  $P_1$  and  $P_2$ . The structure of both linearized closed-loop plants can be visualized according to Figure 57 with inputs and outputs of  $P_1$  defined in Table 15. The  $P_2$  is reduced by excluding the disturbance  $w_2$  from its inputs.

*Table 15: Inputs and outputs of the first considered plant  $P_1$ . The starting index and the ending index describe the location of the regarding quantity within the general input/output vector.*

	Symbol	Unit	Start idx	End idx	Description
<b>I</b>	$w_1$	N	1	6	6DOF force and torque disturbance applied to the top platform reference frame (RF)
	$w_2$	m	7	12	6DOF displacement and rotation kinematic disturbance applied to the bottom platform RF
	$u$	m	13	18	Uniaxial piezoactuator contraction (stroke)
<b>O</b>	$z_1$	m/s	1	3	3 components of the velocity vector of the top platform reference frame origin
	$z_2$	rad/s	4	6	3 components of the angular velocity vector of the top platform reference frame
	$y$	N	7	12	Uniaxial active cable forces

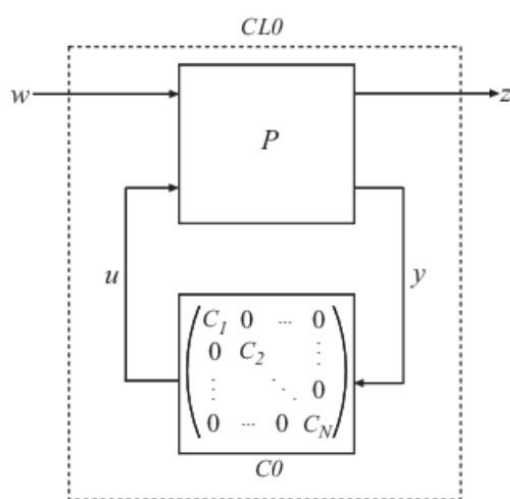


*Figure 57: Closed-loop plant model [50]*

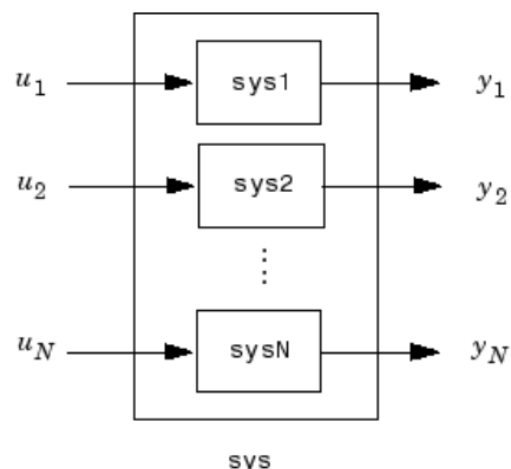


*Figure 58: Multiple operating point (OP) plant assembly, where  $sys1, \dots, sysN$  correspond to linearized plants in different OP [51]*

Because tensegrity structures exhibit highly nonlinear dynamics, let us expand the plant model to multiple linearization points. The structure is linearized in five operating points (OP) along the trajectory, as shown in Table 16, where  $T$  is the period of the trajectory.

*Table 16: Linearization times (snapshots) relative to the trajectory period  $T$*

Linearization point	1	2	3	4	5
Snapshot time	0	$T/4$	$T/2$	$3T/4$	$T$

This step allows us to capture linearized model dynamics in five different configurations along the used trajectory and makes the control law synthesis more robust. Figure 58 shows the procedure of assembling the multiple-OP plant  $P_{a1,2}$  and is analogous for the controller. The open-loop singular value response of the first assembled MIMO plant  $P_{a1}$  from disturbances to error signals, equivalent to  $g = 0$ , is displayed in Figure 59. One can identify that the resonant band of the plant dynamics ranges from 15 Hz to 2 kHz with  $H_\infty(P_{a1}) = 91$  dB in open loop. The second plant  $P_{a2}$ , on the other hand, has an open-loop response shown in Figure 60. It has a smaller band of resonant frequencies from 15 Hz to 1 kHz and much lower  $H_\infty(P_{a2}) = 14.6$  dB norm. It can be concluded that structure is more sensitive to kinematic excitations of the bottom platform than the latter.

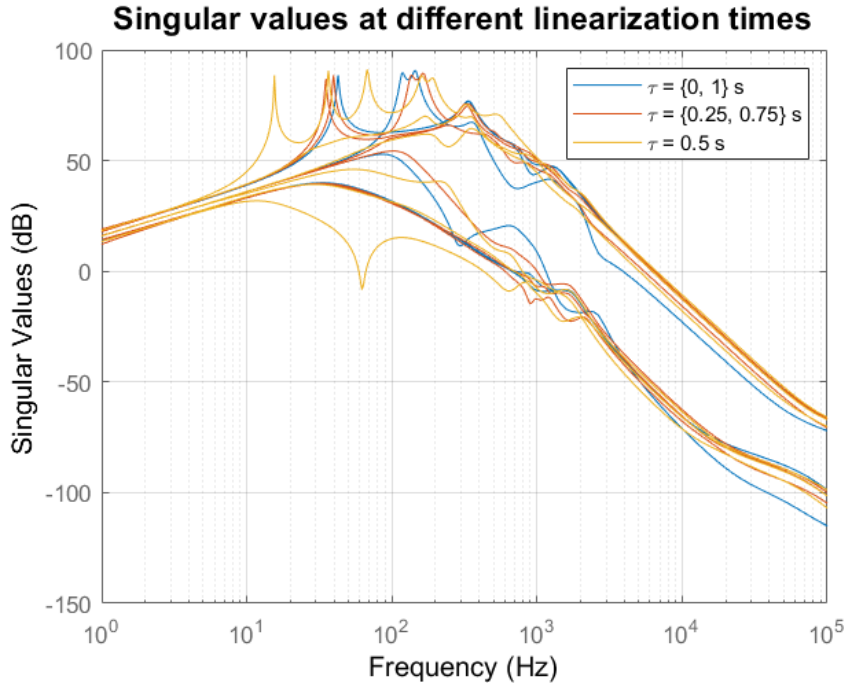


*Figure 59: Open-loop multiple OP disturbance response of plant  $P_{a1}$*

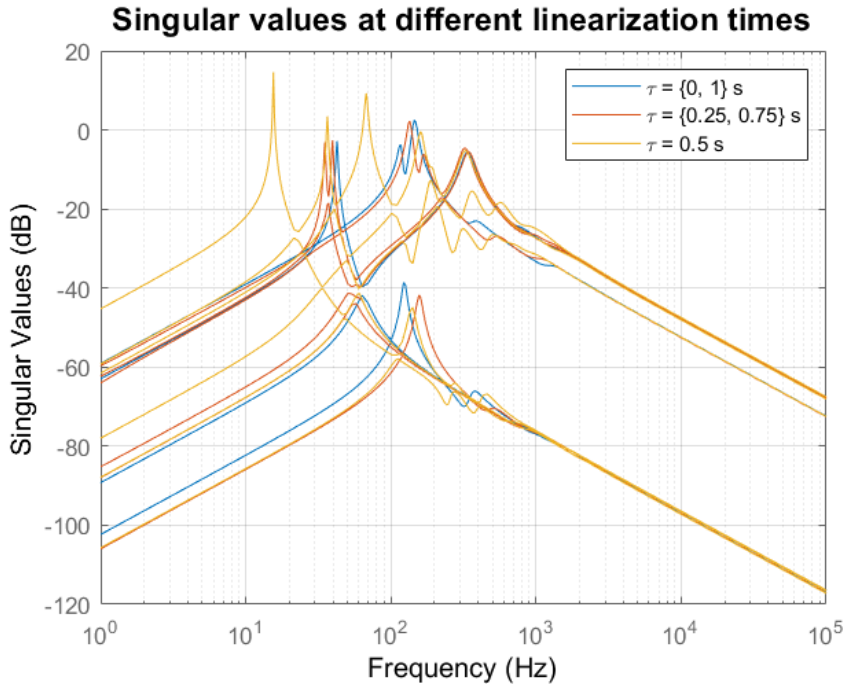


Figure 60: Open-loop multiple OP disturbance response of plant  $P_{a2}$

## 8.2 Control Law Comparison

Let us consider two collocated decentralized active vibration control configurations:

- single-gain decentralized IFF,
- multi-gain decentralized IFF.

These configurations are defined with respect to the number of free parameters, as described in section 3.4 and shown in Figure 57 as the controller  $C_0$ . Single-gain decentralized IFF is the simplest integral force feedback control law, where the gain<sup>11</sup> is identical for all collocated pairs of sensors and actuators, hence only one scalar value  $g$  governs the vibration control with  $g = C_1 = C_2 = \dots = C_N$ . Multi-gain decentralized IFF, on the other hand, enables one to choose a different value for each diagonal element  $C_i$  of the controller, corresponding to different sensor-actuator pairs, while the off-diagonal terms stay null. The controller gain is normalized by the cable specific stiffness  $k_s^c$ . The comparison of mentioned laws is performed by finding the optimal gain values for controller  $C_0$  of plants  $P_{a1,2}$  which minimize the  $H_\infty(P_{a1,2CL})$ -norm, where  $P_{a1,2CL}$

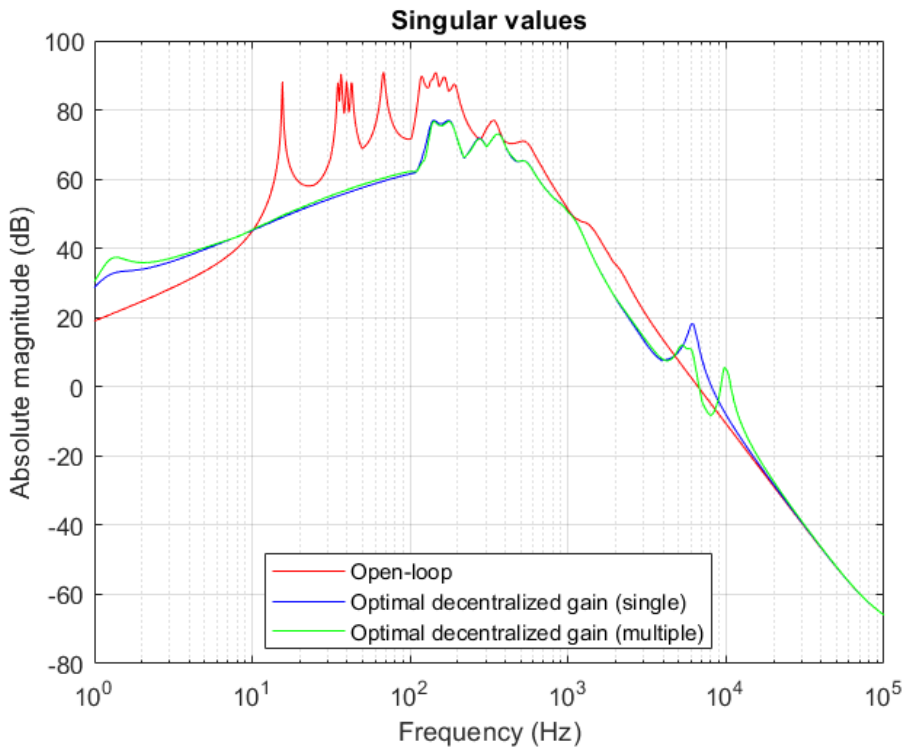
---

<sup>11</sup> SI unit of the gain in our case:  $[g] = \text{ms}^{-1}$

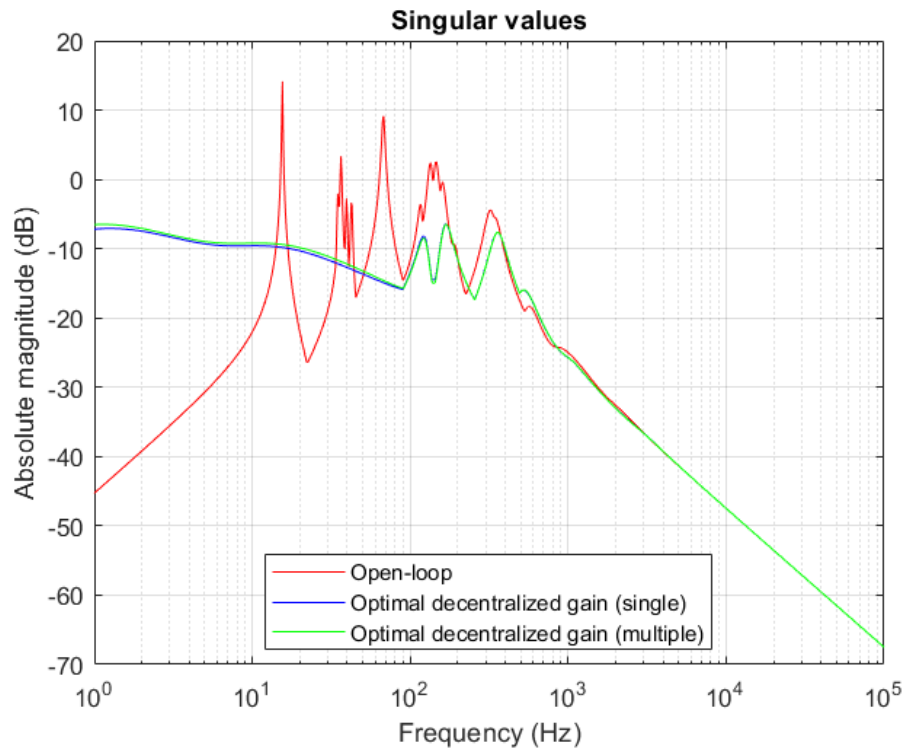
is the assembled multiple-OP plant in closed-loop with the controller. The optimization was performed using the simplex method of *fminsearch* Matlab® function and the optimal gains for each control law are displayed in Table 17. Note that for the case with only top platform force disturbances (no vibration isolation) the optimal gain values are smaller by one order of magnitude. Figure 61 displays the singular value (SV) bound  $\sigma_b(\omega) = \max_i \sigma_i(\omega)$  of plant  $P_{a1}$  for the open-loop case and the two closed-loop cases mentioned above, while Figure 62 shows the SV bound of plant  $P_{a2}$  for the same cases. Note that the SV response is similar for both control laws. This is explained by the initial conditions of the optimization. Firstly, the optimization for single-gain law was performed, starting at  $g_0 = 0$ . Subsequently, the resulting value  $g_{opt}$  was used as an initial condition  $\mathbf{K}_0 = g_{opt} \cdot \mathbf{I}$  for the optimization of the second law, trying to improve the response even further. It is clear that both syntheses resulted in an excellent attenuation of the first three modes.

Table 17:  $H_\infty$ -optimal gains for the chosen control laws

Control law	Plant	$P_{a1}$	$P_{a2}$	$C_0 =$
Single gain decentralized IFF		$g = 25.58 \cdot 10^3$	$g = 4 \cdot 10^3$	$\frac{g}{sk_s^c} \cdot \mathbf{I}$
Multi-gain decentralized IFF		$\mathbf{k} = \begin{bmatrix} 65.46 \\ 21.24 \\ 72.01 \\ 24.39 \\ 69.10 \\ 17.94 \end{bmatrix} \cdot 10^3$	$\mathbf{k} = \begin{bmatrix} 2.96 \\ 4.45 \\ 5.15 \\ 4.29 \\ 4.70 \\ 4.32 \end{bmatrix} \cdot 10^3$	$\frac{1}{sk_s^c} \text{diag}(\mathbf{k})$



*Figure 61: Singular value bound of closed-loop plant  $P_{a1CL}$  with the compared control laws of optimal gains and of the open-loop plant  $P_{a1}$*



*Figure 62: Singular value bound of closed-loop plant  $P_{a2CL}$  with the compared control laws of optimal gains and of the open-loop plant  $P_{a2}$*

Let us now define a sigma bound attenuation  $\Delta\sigma_b(\omega)$  as

$$\Delta\sigma_b(\omega) = \sigma_{bOL} - \sigma_{bCL}, \quad (8.2)$$

where  $\sigma_{bOL}$  is the open-loop SV bound and  $\sigma_{bCL}$  is the closed-loop SV bound of a given controller. The values of the attenuation for the plants and the control laws are displayed in Table 18. Based on the results shown in the table, one can conclude that the best overall performance is achieved by the single-gain decentralized IFF control law, achieving the highest level of attenuation of the first three modes with only a slightly lower  $H_\infty$ -norm than the other law. Both control laws result in a substantial disturbance amplification at low frequencies, nevertheless, still in the negative dB range. In the case of  $P_{a1}$  the laws also introduced minor resonant peaks around  $10^4$  Hz, which most likely corresponds to the controller dynamics. Given these findings and the significant simplicity of the single-gain controller when compared to the multi-gain controller, the following practical implementation on the nonlinear simulation model will utilize the single-gain IFF controller.

*Table 18: Sigma bound attenuation comparison of different control laws*

<b><math>\sigma</math>-bound attenuation (dB)</b>				
	$P_{a1}$		$P_{a2}$	
	<b>Single gain decentralized</b>	<b>Multi-gain decentralized</b>	<b>Single gain decentralized</b>	<b>Multi-gain decentralized</b>
1 <sup>st</sup> mode	39.23	38.72	23.95	23.53
2 <sup>nd</sup> mode	32.90	32.03	11.32	10.83
3 <sup>rd</sup> mode	31.49	30.63	24.03	23.72
$H_\infty$	14.15	14.46	20.97	21.13

### 8.3 Simulation

For practical testing of active vibration suppression, the disturbance signals according to Table 15 are injected into the nonlinear simulation model from section 8.1. These signals are modelled in two ways: band-limited white noise injected to both the top and the bottom platform reference frames; and force impulse applied only to the top frame. The former has a sampling period

$$T_{sd} = \frac{1}{10f_{max}} = \frac{1}{10 \cdot 6300} = 1.6 \cdot 10^{-5} \text{ s} \quad (8.3)$$

where  $f_{max} = 6300$  Hz is the system bandwidth. In our model it corresponds to the frequency where the maximum singular value magnitude of the open-loop system crosses 0 dB as shown in Figure 59.  $T_{sd}$  is also the correlation time of the noise. The noise power was chosen for the top and the bottom platform in such a way to ensure the signal parameters as shown in Table 19.

*Table 19: Injected disturbance noise parameters*

	Signal power (dB)	Average RMS	Average peak-to-peak	Unit
<b>Top platform</b>	-34	35	296	N
<b>Bottom platform</b>	-240	0.25	2.1	mm

The latter corresponds to a rectangular force impulse such that its RMS over period  $T$  is the same as of the former, and its amplitude is equal to one half of the peak-to-peak of the former. This results in an impulse of amplitude  $F_I = 148$  N and period  $t_I = 0.236T$ , starting at  $\tau = 0$ .

Firstly, the nonlinear closed-loop model was simulated with optimal gains obtained in section 8.2:  $g = 25.58 \cdot 10^3 \text{ ms}^{-1}$  for the white noise disturbance; and  $g = 4 \cdot 10^3 \text{ ms}^{-1}$  for the force impulse disturbance. For both cases, the simulation model collapsed to a different equilibrium position, violating the desired trajectory dramatically. This was caused by a hard model nonlinearity – singularity in the form of infinitesimal mechanism.

For this reason, the actual simulation gain had to be modified to a value  $g_{mod} = 70 \text{ ms}^{-1}$ , so that the starting equilibrium configuration is preserved. Moreover, an upstream high-pass filter with cutoff frequency of 5 Hz was introduced to account for the piezoelectric force sensor DC-rejection characteristic as mentioned in section 5.1.

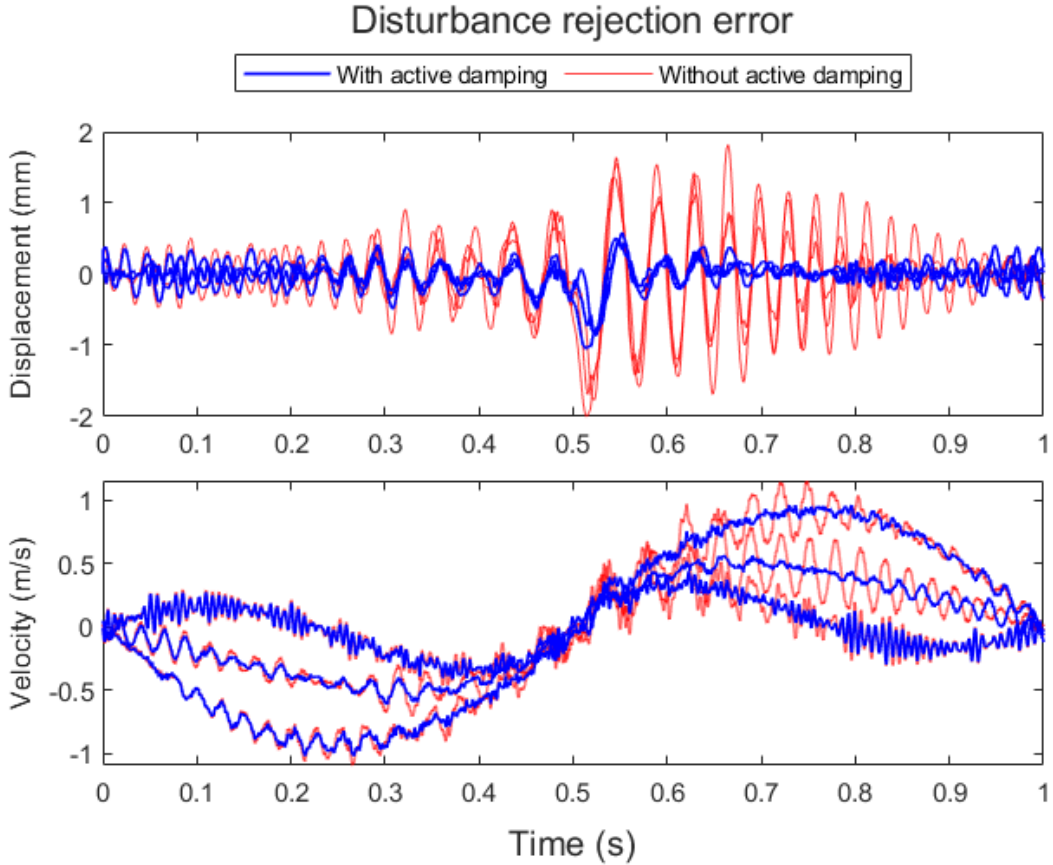


*Figure 63: Task-space displacement and velocity error with white noise disturbance*

After the disturbance injection, the actual manipulator trajectory is distorted. Firstly, Figure 63 shows the disturbance rejection error of the tensegrity manipulator as it traces the chosen trajectory with white noise disturbances to both the top and bottom platform. This error is the deviation between the disturbance-injected output and the output without external disturbances and it is displayed for both the open-loop and the closed-loop case. A significant improvement in the trajectory tracking of the task-space translation was recorded. The performance is worse for the tracking of the task-space rotation, especially for the angular velocity tracking. Thus, the angular position and velocity responses on white noise are not plotted for clarity. These findings are quantified in Table 20. In this table, the power attenuation of the disturbance output response signal superimposed on the original signal is shown.

It is calculated as follows:

$$\Delta w_i = w_i - w_{i0} \quad (8.4)$$

where  $\mathbf{w} = \{\mathbf{u}, \boldsymbol{\varphi}, \dot{\mathbf{u}}, \dot{\boldsymbol{\varphi}}\}$  are the displacement, rotation, velocity, and angular velocity signals, respectively,  $i = \{x, y, z\}$  is the task-space direction and “0” signifies the original signal without disturbances, as shown in Figure 52. The relative average power attenuation is then defined as

$$\Delta \bar{S}_{ii}^w = \frac{\bar{S}_{ii0}^w - \bar{S}_{ii}^w}{\bar{S}_{ii0}^w}, \quad (8.5)$$

where  $\bar{S}_{ii}^w$  is the average power of signal  $\Delta w_i$  and the subscript “0” signifies the open-loop disturbance response.

*Table 20: Output signal relative power attenuation*

		$\Delta \bar{S}_{ii} (\%)$			
		$\Delta u$	$\Delta \dot{u}$	$\Delta \varphi$	$\Delta \dot{\varphi}$
<b>White noise</b>	$x$	88.6	86.7	48.3	9.8
	$y$	83.4	82.6	73.4	11.3
	$z$	87.1	64.8	47.0	27.4
<b>Force pulse</b>	$x$	68.5	73.2	94.8	66.4
	$y$	91.3	87.8	65.3	46.3
	$z$	94.7	91.0	77.3	59.7

Secondly, the table also shows the relative power attenuation of the force impulse response. Note that the force impulse power attenuation is computed for the signal after the pulse falling edge. The impulse response is plotted in Figure 64 for displacement and velocity both in position and orientation. On the contrary to the white noise case, here the disturbance rejection error is reduced well for both translation and rotation, which becomes clear in the second half of the trajectory, where the pulse wears off.

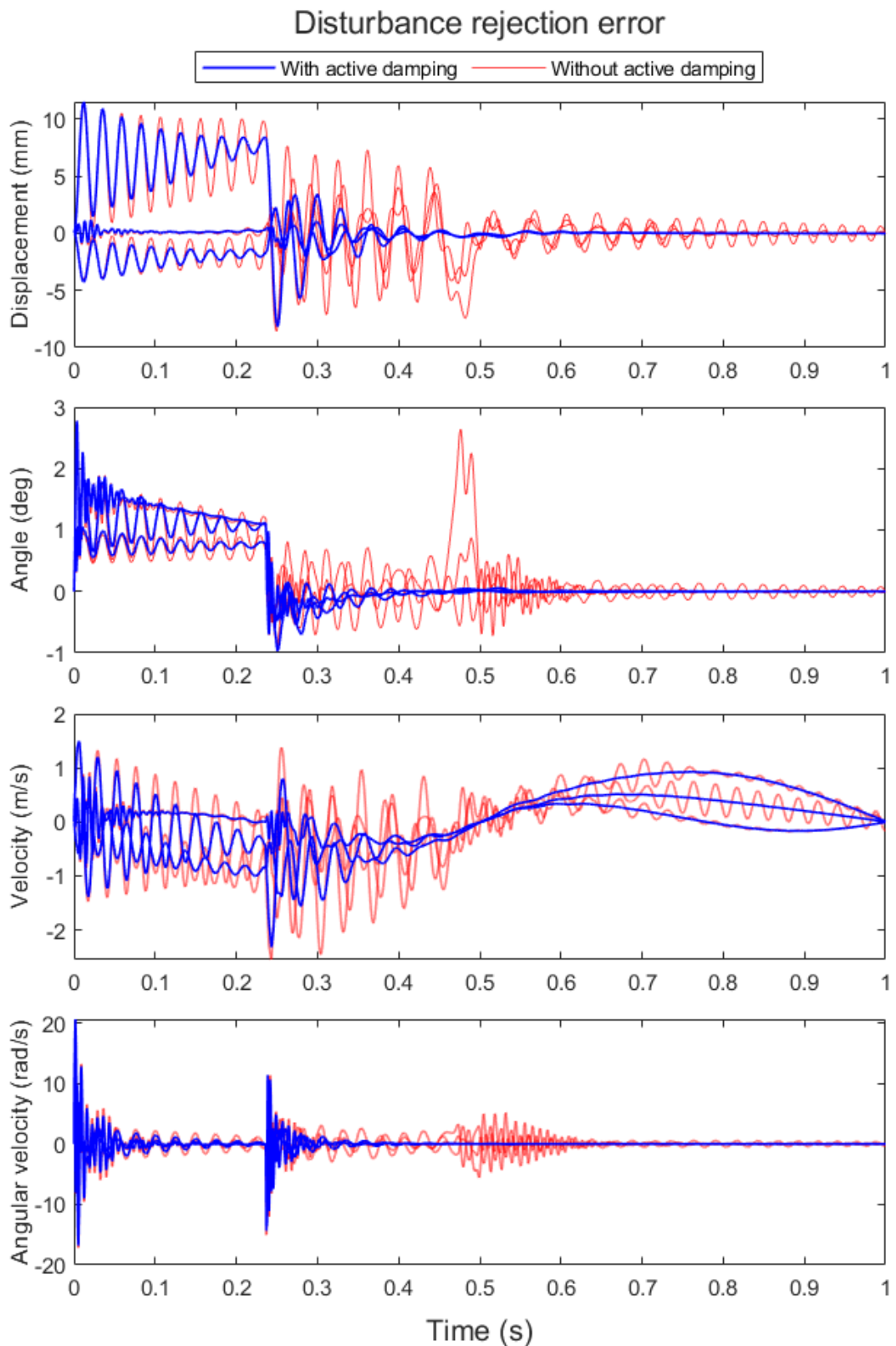
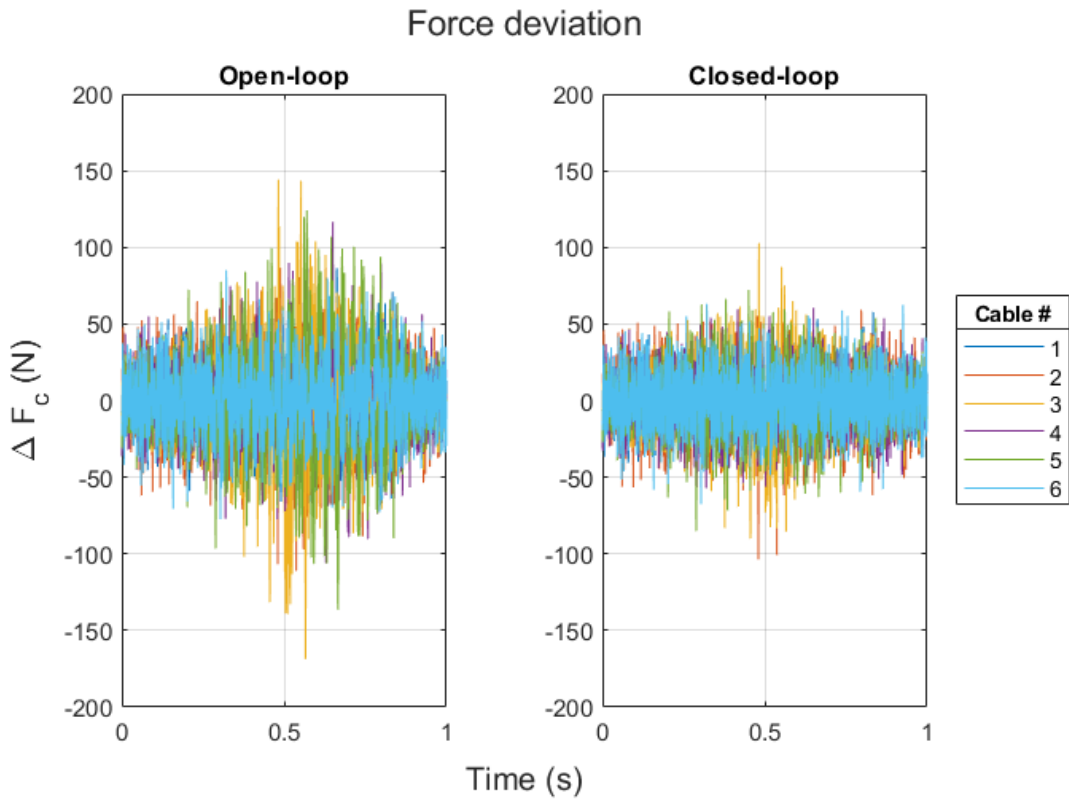


Figure 64: Disturbance rejection error of the force impulse response

Additionally, the forces of the mid-level cables are examined in this section. We can consider the cable forces to be a superposition of forces induced by the CTC control and external disturbances. The former results in a smooth trajectory as shown in Figure 52, while the latter corresponds to force fluctuations plotted in Figure 65. These fluctuations are computed as the difference of the forces with external white noise disturbances and the baseline forces without them. Naturally, these fluctuations are smaller with control than in open-loop. This is explained by the unconditional stability of the collocated decentralized IFF control, where the energy is always dissipated through the controller, resulting in a negative energy flow. This condition forces the control to always relax the cable as it is under tension, ultimately, reducing the internal force. Let us quantify the above energy condition. A well-known power transfer formula for collocated decentralized IFF control has a form

$$\dot{W}_i = F_i \dot{\delta}_i = -g_i F_i^2 < 0, \quad (8.6)$$

where  $F_i$  is the force measured in the  $i$ -th cable,  $\delta_i$  is a piezoactuator stroke in the  $i$ -th cable and  $g_i \in (0, \infty)$  the corresponding IFF gain for the  $i$ -th active cable [26]. It ensures that the control is always dissipative and does not add energy into the system, guaranteeing stability. As one can see in Figure 66, this assumption holds for most of the time during simulation. The minor inwards energy flow can be explained by the force filtering. This filtering ensures that the active damping of vibrations will not interfere with the high-authority trajectory control and has a form of a second-order high-pass filter with cutoff frequency of 5 Hz. This is equivalent to the inherent high-pass filtering property of the piezoelectric force sensor and is justified in [26].



*Figure 65: Deviation of the real cable force from the cable force without white noise disturbance injection*

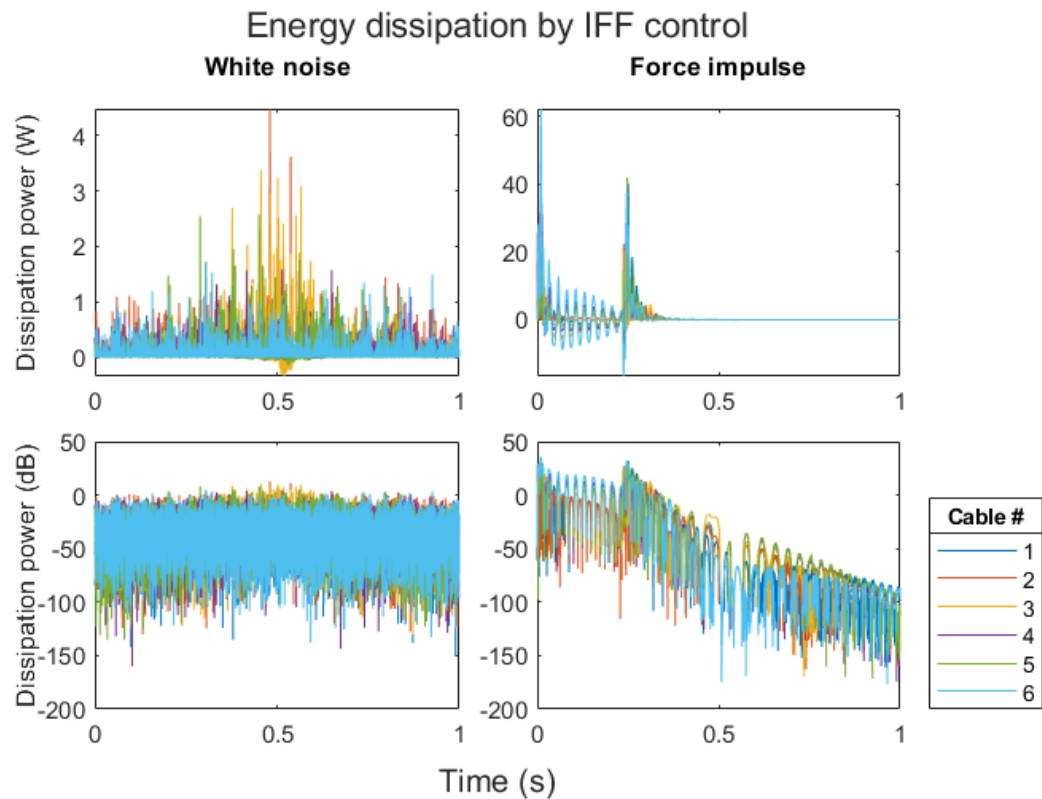


*Figure 66: Energy dissipation of the IFF control for both disturbance types*

## 9 Conclusion Remarks

Chapter 1 introduces the reader to the topic of serial and parallel robotics, while presenting a novel concept – the tensegrity robot, and its utilization of the mentioned architectures. The chapter briefly summarizes the main aspects of the new structure in connection to robotics, including infinitesimal mechanisms, which leads to the following proposal of active vibration suppression in these structures. The author summarizes his research motivation in connection to the discussed problem.

In chapter 2 a wide-ranging review of mechanisms using the tensegrity concept is performed. The review predominantly deals with mechanisms capable of large displacements, namely locomotion and manipulation, the two most common applications thereof. A significant progress in the field becomes clear and potential applications of the mentioned mechanisms are proposed.

Chapter 3 generalizes out of the aforementioned domains – tensegrity and robotics, so that it can elaborate on the concept of active vibration control from different perspectives. These perspectives include robotic structures as well as civil engineering structures and compares the concept of active damping with the former approach of the passive one. For these applications, the importance of the distinction between the flexural and the rigid-body modes is emphasized. Furthermore, the different classifications of active damping are introduced and described. Their juxtaposition reveals the influence on closed-loop stability as well as the suitability for various applications, such as vibration isolation. Chapter 4 briefly summarizes the general objectives of the thesis.

In chapter 5 the sensor and actuator selection are composed of two parts. The theoretical part deals with a general concept of electromechanical components used in smart materials and it is primarily focused on piezoelectric components, widely used in vibration control. The piezoelectric effect is characterized and translated to applications of force sensing and actuation. Afterwards, in the practical part, different aspects of sensor and actuator selection are considered, and specific components are selected for following analyses. Finally, the specifications of chosen components as well as the according circuitry, intended for a further electromechanical development of the demonstrator, are displayed for the reader.

Chapter 6 summarizes the author's development of large displacement actuator optimization methods. These were applied on the simplest tensegrity topology – the S3 simplex. The presence of significant nonlinearities within the model dynamics prevented the use of linear control theory, and instead relied on numerical simulations and global optimization techniques. The results of the optimization can be interpreted as less general than the linear case for the reason of the dimensionality curse, allowing the author to describe the behavior only in a limited number of dimensions. Despite this complexity, an optimal placement is found for every allowable number of actuators. The behavior is as expected in terms of the structural symmetries and the anticipated cost function monotonicity, confirming the validity of the optimization approach.

On the contrary to the previous paragraph, chapter 0 utilizes linear control theory to develop an alternative and more general way of actuator and sensor placement. The structure from the previous chapter was modified to result in a more complicated type-2 tensegrity tower. Firstly, a finite-element model is developed to capture the plant dynamics in a more responsive manner than in the case of the simulation model. The resulting linear dynamical model is in the form of an almost-balanced state space system, suitable for the collocated sensor and actuator placement. Secondly, sophisticated criterions of optimality, based on the Gramian approach, were introduced to normalize the modal behavior and to capture the dynamics in different configurations. Finally, the method is successfully implemented on the mentioned structure and resulted in comprehensive qualitative and quantitative results suitable for performance decision-making.

At last, chapter 8 introduces another structure - the most sophisticated structure when compared to the aforementioned two. Firstly, the structure is modelled with realistic data, so that the results are interpretable in real-world constraints. The specifications of the structure itself as well as of the CTC controller are mentioned there. Further, the prescribed trajectory of the manipulator and the performance of the CTC thereon is summarized and the linear multi-OP model for the IFF control law synthesis is derived. Secondly, on the linearized model in this chapter, two control laws are compared: single-gain IFF and multi-gain IFF. Despite the similar performance of the two, the former is chosen for the subsequent simulation because of its simplicity. In the final part of the chapter, a complex simulation of the model is performed both in open-loop and closed-

loop, both in presence and absence of external disturbances of distinct types. It is shown that the implemented method of active vibration suppression using collocated decentralized integral force feedback is highly effective for tensegrity structures. It is found to be more effective in the case of the force impulse vibration mitigation applied to the top platform, than in the case of the combined force/kinematic excitation with white noise. More specifically, the suppression was successful for both cases of translational task-space vibrations, but less so for the rotational vibrations, where the substantial damping is recorded for the former case only. This finding results in a realization that the pointing performance of controlled tensegrity manipulators needs to be addressed more deeply when kinematic excitations of the base frame are present.

## A. Gramians of a Simple Planar Tensegrity

In this appendix we investigate the properties of the non-collocated modal stiffness matrix as described in section 7.4. Let us have a planar compliant tensegrity structure according to Figure 67. The strut is represented by a solid line and the cables by a dashed line. The FEM incidence table of elements and nodes is then given by Figure 67, where  $k_s^e$  is the elemental specific stiffness,  $a$  is the characteristic length,  $e$  is the element number and  $i$  is the local node number.

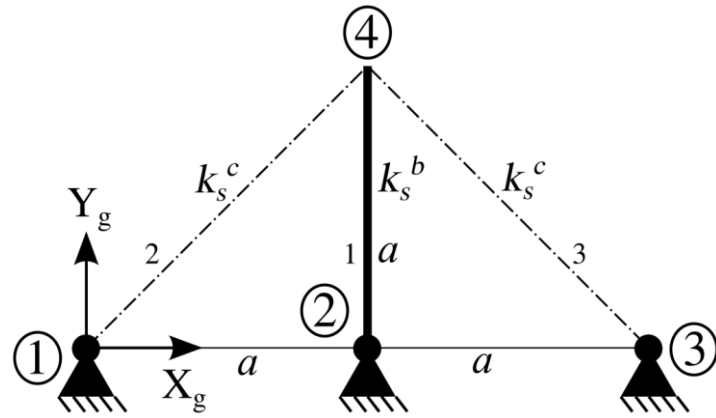


Figure 67: Simple planar tensegrity structure

Table 21: FEM incidence table of the case structure

$e \backslash i$	1	2
1	2	4
2	1	4
3	3	4

The incidence matrix  $\Pi$  is then defined as follows:

$$\begin{aligned} \Pi &= [\mathbf{0}_2 \quad \mathbf{I}_2 \quad \mathbf{0}_2 \quad \mathbf{I}_2 \quad \mathbf{0}_2 \quad \mathbf{I}_2] \\ &= \begin{bmatrix} 0 & 0 & 1 & 0 & 0 & 0 & 1 & 0 & 0 & 0 & 1 & 0 \\ 0 & 0 & 0 & 1 & 0 & 0 & 0 & 0 & 1 & 0 & 0 & 1 \end{bmatrix}, \end{aligned} \quad (9.1)$$

the directional cosine projection vectors

$$\mathbf{h}^1 = [0 \quad -1 \quad 0 \quad 1], \quad (9.2)$$

$$\mathbf{h}^2 = \frac{\sqrt{2}}{2} [-1 \quad -1 \quad 1 \quad 1], \quad (9.3)$$

$$\mathbf{h}^3 = \frac{\sqrt{2}}{2} [1 \quad -1 \quad -1 \quad 1], \quad (9.4)$$

the specific stiffness matrix

$$\mathbf{K}_s = \text{diag}([k_s^b \quad k_s^c \quad k_s^c]), \quad (9.5)$$

where  $k_s^b$  is the specific strut stiffness,  $k_s^c$  specific cable stiffness, and the inverse element length

$$\mathbf{L}_0^{-1} = \frac{1}{a} \text{diag} \left( \begin{bmatrix} 1 & \frac{\sqrt{2}}{2} & \frac{\sqrt{2}}{2} \end{bmatrix} \right). \quad (9.6)$$

The global stiffness matrix is then defined as

$$\mathbf{K} = \begin{bmatrix} \frac{\sqrt{2}k_s^c}{2a} \left( \frac{\Delta l_0^c}{\sqrt{2}a - \Delta l_0^c} + 1 \right) & 0 \\ 0 & \frac{k_s^b}{a} + \frac{\sqrt{2}k_s^c}{2a} \left( \frac{\Delta l_0^c}{\sqrt{2}a - \Delta l_0^c} + 1 \right) \end{bmatrix}, \quad (9.7)$$

where  $\Delta l_0^c \in \langle 0, \sqrt{2}a \rangle$  is an initial cable contraction for structural prestress, kept identical for both cables for simplicity, and the global inertia matrix is defined as

$$\mathbf{M} = 2 \left[ am_s^b + 2m_s^c (\sqrt{2}a - \Delta l_0^c) \right] \begin{bmatrix} 1 & 0 \\ 0 & 1 \end{bmatrix}, \quad (9.8)$$

which leads us to the following eigenmode realization sorted in ascending order and yields the spectral matrix

$$\boldsymbol{\Lambda} = \boldsymbol{\Omega}^2 = \frac{1}{d_\Lambda} \begin{bmatrix} \sqrt{2}ak_s^c & 0 \\ 0 & \sqrt{2}ak_s^c + k_s^b(2a - \sqrt{2}\Delta l_0^c) \end{bmatrix}, \quad (9.9)$$

where

$$d_\Lambda = 2\sqrt{2}a \left[ \left( \sqrt{2}m_s^b + 4m_s^c \right) a^2 + \left( m_s^b + 4\sqrt{2}m_s^c \right) \Delta l_0^c a + 2(\Delta l_0^c)^2 m_s^c \right] \quad (9.10)$$

and the modal matrix

$$\Phi = \begin{bmatrix} 1 & 0 \\ 0 & 1 \end{bmatrix}. \quad (9.11)$$

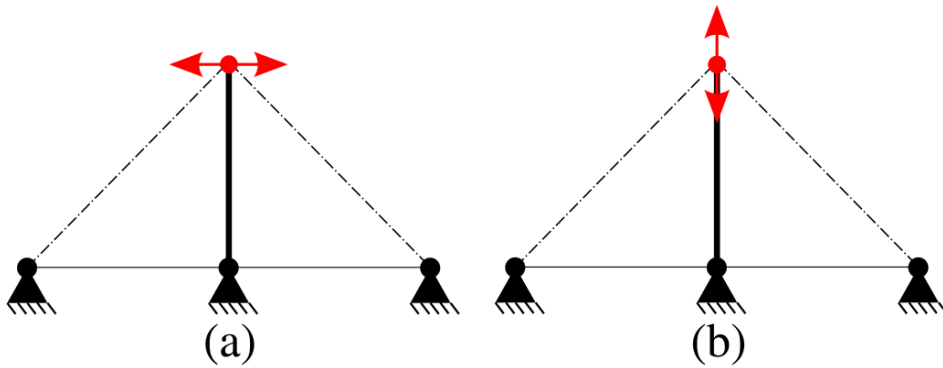


Figure 68: Eigenmodes of the structure: a) first; b) second

Let us now assume the presence of sensors and actuators in all elements

$$\mathbf{a} = [1, 1, 1]^T, \quad \mathbf{s} = [1, 1, 1]^T. \quad (9.12)$$

Hence, the input and output matrices yield

$$\mathbf{B} = \frac{\sqrt{2}}{2} \begin{bmatrix} 0 & 0 & 0 \\ 0 & 0 & 0 \\ 0 & 1 & -1 \\ \sqrt{2} & 1 & 1 \end{bmatrix}, \quad \mathbf{C} = \frac{1}{2a} \begin{bmatrix} 0 & 2k_s^b & 0 & 0 \\ k_s^c & k_s^c & 0 & 0 \\ -k_s^c & k_s^c & 0 & 0 \end{bmatrix}. \quad (9.13)$$

The input matrix interpretation is straightforward; however, we can interpret the output matrix as being the stiffness matrix which maps the modal displacements of the node 4 into the axial forces  $q_1, q_2, q_3$  within the structure elements. The eigenmodes then can be visualized according to Figure 68. Further, we utilize the fact that the controllability Gramian tends to diagonal form for displacement sensors [45], which is directly tied to the element internal force through stiffness. Arbitrary real positive damping ratios  $\zeta_1$  and  $\zeta_2$  are introduced, so that the state-transition matrix  $e^{\mathbf{A}t}$  is asymptotically stable, thus, the

Gramians reach the steady state and are then the solutions of Lyapunov equations [46].

The Gramians are defined in the diagonal form as follows:

$$\mathbf{W}_c : \begin{cases} (\mathbf{W}_c)_{11} = (\mathbf{W}_c)_{22} = \frac{1}{4\zeta_1} \sqrt{\frac{d_\Lambda}{\sqrt{2}ak_s^c}} \\ (\mathbf{W}_c)_{33} = (\mathbf{W}_c)_{44} = \frac{1}{2\zeta_2} \sqrt{\frac{d_\Lambda}{\sqrt{2}ak_s^c + k_s^b(2a - \sqrt{2}\Delta l_0^c)}} \end{cases}, \quad (9.14)$$

$$\mathbf{W}_o : \begin{cases} (\mathbf{W}_o)_{11} = (\mathbf{W}_o)_{22} = \frac{(k_s^c)^2}{8\zeta_1 a^2} \sqrt{\frac{d_\Lambda}{\sqrt{2}ak_s^c}} \\ (\mathbf{W}_o)_{33} = (\mathbf{W}_o)_{44} = \frac{2(k_s^b)^2 + (k_s^c)^2}{8\zeta_2 a^2} \sqrt{\frac{d_\Lambda}{\sqrt{2}ak_s^c + k_s^b(2a - \sqrt{2}\Delta l_0^c)}} \end{cases}. \quad (9.15)$$

We can see that the Gramians are diagonal and hence are corresponding to their principal components. To plot normalized controllability and observability energy ellipsoids, as displayed in Figure 69, we define additional parameters in the form:  $\mu_c$

$$z = \frac{\zeta_1}{\zeta_2}, \quad \kappa = \frac{k_s^b}{k_s^c}, \quad \eta = \frac{\Delta l_0^c}{\sqrt{2}a}. \quad (9.16)$$

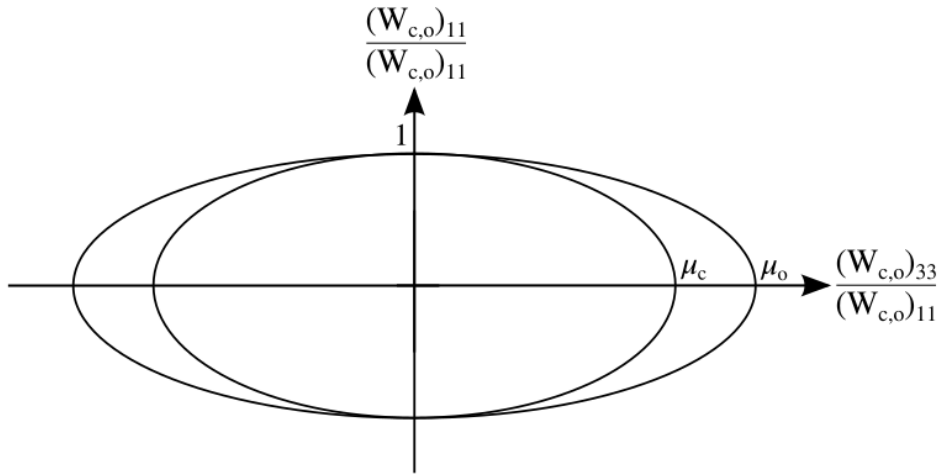


Figure 69: Controllability and observability energy ellipsoids

The ellipsoid semiaxis length ratios are then

$$\mu_c = \frac{(\mathbf{W}_c)_{33}}{(\mathbf{W}_c)_{11}} = \frac{2z}{\sqrt{1 + \sqrt{2}\kappa(1 - \eta)}}, \quad (9.17)$$

$$\mu_o = \frac{(\mathbf{W}_o)_{33}}{(\mathbf{W}_o)_{11}} = \frac{(2\kappa^2 + 1)z}{\sqrt{1 + \sqrt{2}\kappa(1 - \eta)}}, \quad (9.18)$$

and the plotted dependencies are displayed below in Figure 70 - Figure 72.

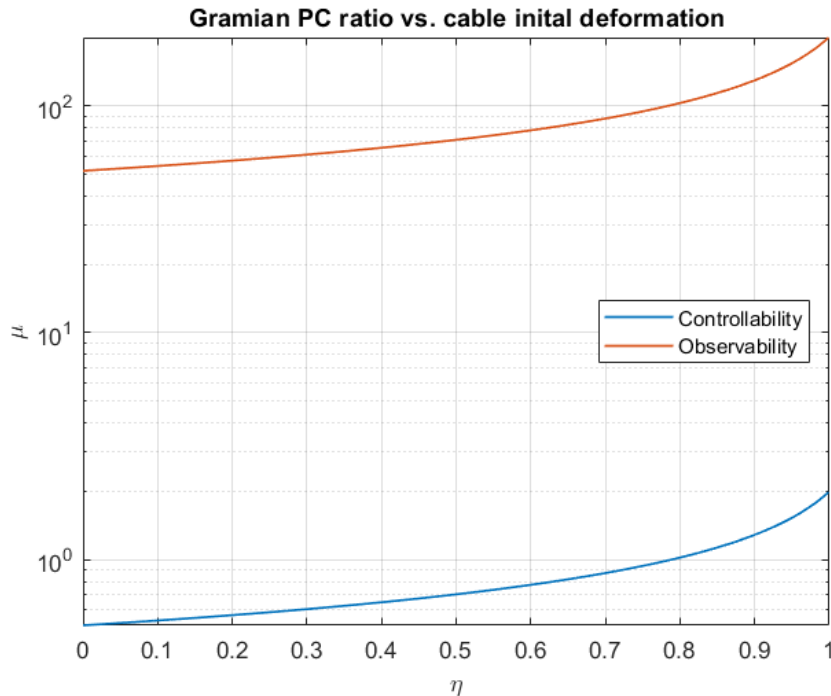


Figure 70: Gramian principal component ratio with varying initial prestressing cable elongation

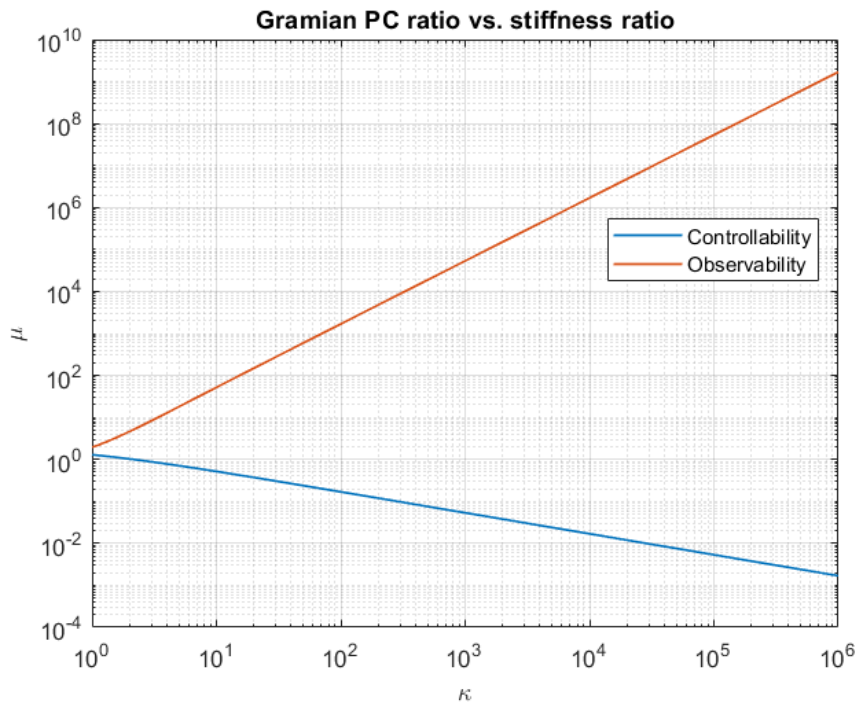


Figure 71: Gramian principal component ratio with varying strut-to-cable specific stiffness ratio

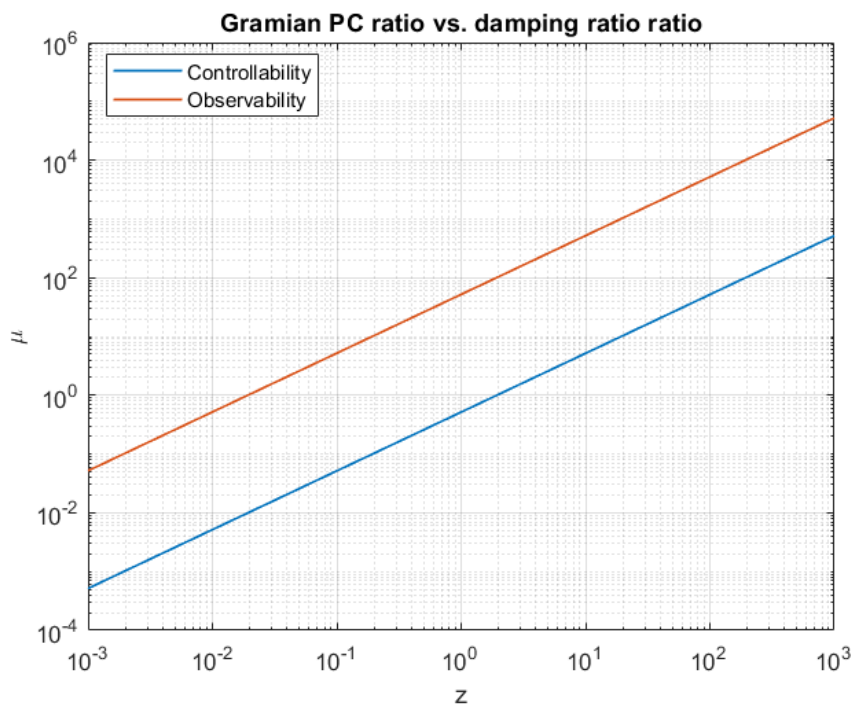


Figure 72: Gramian principal component ratio with varying damping ratio of the first mode relative to the second mode

Finally, we plotted the relative controllability and observability expressed by the Gramian principal component (PC) ratios. As the strut becomes stiffer or the cables more compliant, the observability of the first mode, relative to the second, vanishes. The explanation is that the second mode translates its displacement into the strut completely in the axial direction with no rotational components, hence maximizing the axial load. However, in the horizontal direction of the first mode, the modal displacement does not contribute to the strut axial stress and only rotates it, which prevents the strut from generating any internal force except the prestressing force. This finding is applicable when the internal force is sensed in all elements. In other cases, where only particular elements have internal sensing, the corresponding rows of matrix **C** become null.

## B. Active Cable Model

Let us consider an active cable with collocated sensor/actuator pair according to Figure 17. The collocated pair will be referred to as transducer. The entire cable can be simplified as two springs in series, where the transducer is a spring of stiffness  $k_a$  variable rest length  $l_{a0}(t)$ , and the cable is a spring of variable stiffness  $k_c(t)$  and variable rest length  $l_{c0}(t)$ . When a nonzero tensile force  $F(t)$  is applied to the cable, it is deformed according to Figure 73, inducing transducer deformation  $\varepsilon(t) = l_a(t) - l_{a0}(t)$  and cable deformation  $\eta(t) = l_c(t) - l_{c0}(t)$ . This results in the overall deformation of the active cable  $\Delta L(t) = L(t) - L_0(t)$ , where  $L_0(t)$  is the rest length of the whole active cable system.

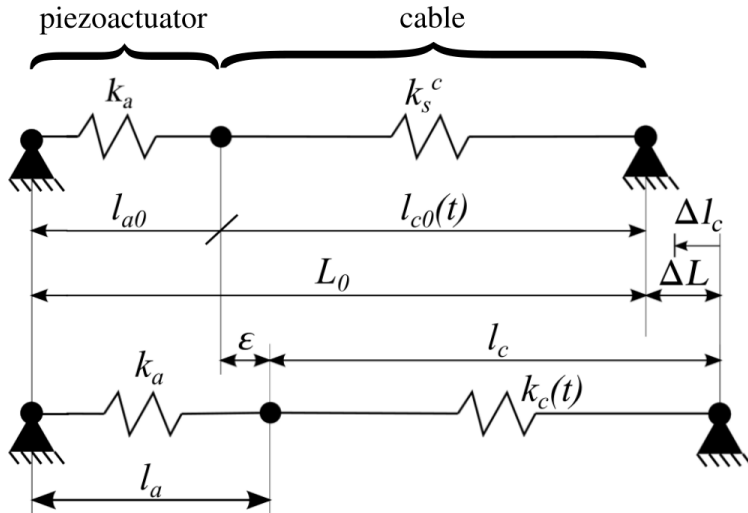


Figure 73: Simplified model of an active cable

We can then define further relation: the cable stiffness

$$k_c = \frac{k_c^s}{l_{c0}}, \quad (9.19)$$

where  $k_c^s$  is the cable specific stiffness. The cable rest length is variable in the form

$$l_{c0} = L_0 - l_{a0}, \quad (9.20)$$

where  $l_{a00}$  is the nominal rest length of the transducer when its electrodes are short-circuited ( $V = 0$ ). Nonzero voltage across the electrodes of the actuator induces a change of its rest length  $\delta(t)$ , called the *stroke*, and it is defined as

$$l_{a0} = l_{a00} + \delta. \quad (9.21)$$

Furthermore, the cable is subjected to a geometric boundary condition

$$l_c = L - l_{a0} - \varepsilon, \quad (9.22)$$

tying the transducer deformation and the cable deformation together. At last, the equilibrium equations of the springs yield

$$F = k_a \varepsilon, \quad (9.23)$$

$$F = k_c \eta. \quad (9.24)$$

Using equations (9.21) and (9.22) we can redefine the passive deformation of the cable segment

$$\eta = L - l_{a0} - \varepsilon - l_{c0} = L - L_0 - \varepsilon - \delta = \Delta L - \varepsilon - \delta, \quad (9.25)$$

and from the equilibrium equations (9.23) and (9.24) we get the relation

$$\varepsilon = \frac{k_c}{k_a + k_c} (\Delta L - \delta). \quad (9.26)$$

Then the tensile force can be defined in terms of the known deformations

$$F = k_a \varepsilon = k (\Delta L - \delta), \quad (9.27)$$

where, when using equation (9.19), the composite stiffness of the active cable according to the rule of springs in series is

$$k = \frac{k_a k_c}{k_a + k_c} = \frac{k_c^s k_a}{k_c^s + k_a (L_0 - l_{a00})}, \quad (9.28)$$

which results in a general expression for the cable elastic force

$$F_c(t) = \frac{k_c^s k_a}{k_c^s + k_a \{L_0(t) - l_{a00}\}} \{L(t) - L_0(t) - \delta(t)\}. \quad (9.29)$$

If the cable force  $F_c$  and its actual length  $L$  are known, the rest length  $L_0$  can be expressed as

$$L_0 = \frac{k_c^s k_a L - F_c (k_c^s - k_a l_{a00})}{k_a (F_c + k_c^s)}, \quad (9.30)$$

which can be simplified to

$$L_0 = \frac{k_c^s L}{F_c + k_c^s} \quad (9.31)$$

under assumptions  $k_a \gg k_c^s$ , and  $k_c^s L \gg F_c l_{a00}$ , which can be redefined as

$$L \gg \frac{F_c}{k_c^s} l_{a00} \quad (9.32)$$

and can be interpreted as the deformation of a cable of length  $l_{a00}$  under the force  $F_c$ . Both assumptions can be considered valid for realistic configurations, geometries and parameters. Further, we define the damping force of the active cable

$$F_{damp} = b_c \dot{l}_c \quad (9.33)$$

which is assumed to occur only in the passive cable segment and not the transducer. Firstly, let us express the length of the passive cable

$$\begin{aligned} l_c(t) &= L(t) - l_{a00} - \delta(t) - \varepsilon(t) \\ &= L(t) - l_{a00} - \delta(t) - \frac{k_c^s \{L(t) - L_0(t) - \delta(t)\}}{k_c^s + k_a \{L_0(t) - l_{a00}\}}. \end{aligned} \quad (9.34)$$

Now we can define the damping coefficient of the cable segment

$$b_c(t) = \frac{b_c^s}{l_{c0}(t)} = \frac{b_c^s}{L_0(t) - l_{a00}}, \quad (9.35)$$

where  $b_c^s$  is a specific damping coefficient of the cable. Using the chain rule, let us express the cable deformation speed

$$\dot{l}_c = \frac{\partial l_c}{\partial L} \dot{L} + \frac{\partial l_c}{\partial \delta} \dot{\delta} + \frac{\partial l_c}{\partial L_0} \dot{L}_0, \quad (9.36)$$

where according to equation (9.34) we get the partial derivatives

$$\begin{aligned} \frac{\partial l_c}{\partial L} &= 1 - \frac{k_c^s}{k_c^s + k_a \{L_0 - l_{a00}\}} \cong 1, \\ \frac{\partial l_c}{\partial \delta} &= -1 + \frac{k_c^s}{k_c^s + k_a \{L_0 - l_{a00}\}} \cong -1, \\ \frac{\partial l_c}{\partial L_0} &\cong \frac{k_c^s}{k_a^2 L_0^2} \{k_c^s - k_a(l_{a00} + \delta)\} \cong 0, \end{aligned} \quad (9.37)$$

which are valid for the same assumptions as in equation (9.32). The velocity is then

$$\dot{l}_c = \dot{L} - \dot{\delta} \quad (9.38)$$

which finally yields

$$F_{damp} = b_c^s \frac{\dot{L} - \dot{\delta}}{L_0 - l_{a00}}. \quad (9.39)$$

## C. Electronic Data

Electronic files such as the simulation models, data files, scripts, and other code, are attached to this thesis. They are included on the attached CD and the GitHub repository: <https://github.com/tsindel/tensegrity-thesis>. Please see the README file in the directory for more information about the structure of the files.

# Bibliography

- [1] Y. Liu, Q. Bi, X. Yue, Y. Li, B. Yang and J. Wu, "A review on tensegrity structures-based robots," *Mechanism and Machine Theory*, vol. 168, no. 104571, 2022.
- [2] Z. Pandilov and V. Dukovski, "COMPARISON OF THE CHARACTERISTICS BETWEEN SERIAL AND PARALLEL ROBOTS," *Acta Technica Corviniensis-Bulletin of Engineering*, vol. 7, no. 1, 2014.
- [3] R. Motro, *Tensegrity: structural systems for the future*, Elsevier, 2003.
- [4] K. Snellson, "Snellson on the tensegrity invention," *International Journal of Space Structures*, vol. 11, no. 1-2, pp. 43-48, 1996.
- [5] R. E. Skelton, R. Adhikari, J.-P. Pinaud, W. Chan and J. W. Helton, "An Introduction to the Mechanics of Tensegrity Structures," in *Proceedings of the 40th IEEE Conference on Decision and Control*, Orlando, Florida, USA, 2001.
- [6] C. Sultan, "Tensegrity deployment using infinitesimal mechanisms," *International Journal of Solids and Structures*, vol. 51, no. 21-22, pp. 3653-3668, 2014.
- [7] M. Pedretti, "Smart tensegrity structures for the Swiss Expo 2001," *Smart Structures and Materials 1998: Sensory Phenomena and Measurement Instrumentation for Smart Structures and Materials*, vol. 3330, pp. 378-386, 1998.
- [8] D. S. Shah, J. W. Booth, R. L. Baines, K. Wang, M. Vespiagnani, K. Bekris and R. Kramer-Bottiglio, "Tensegrity robotics," *Soft robotics*, 2021.
- [9] Oppenheim, J. Irving and W. O. Williams, "Vibration of an elastic tensegrity structure," *European Journal of Mechanics-A/Solids*, vol. 20, no. 6, pp. 1023-1031, 2001.
- [10] *Active vibration control of a three-stage tensegrity structure*, vol. 5386, Chan, Wai Leung, et al. "Active vibration control of a three-stage tensegrity structure." *Smart Structures and Materials 2004: Damping and Isolation*. Vol. 5386. SPIE, 2004., 2004.

- [11] C. Sultan, "Stiffness formulations and necessary and sufficient conditions for exponential stability of prestressable structures," *International Journal of Solids and Structures*, vol. 50, no. 14-15, pp. 2180-2195, 2013.
- [12] S. Lessard, D. Castro, W. Asper, S. D. Chopra, L. B. Baltaxe-Admony, M. Teodorescu, V. SunSpiral and A. Agogino, "A bio-inspired tensegrity manipulator with multi-DOF, structurally compliant joints," in *IEEE/RSJ International Conference on Intelligent Robots and Systems (IROS)*, 2016.
- [13] A. Iscen, A. Agogino, V. SunSpiral and K. Tumer, "Learning to control complex tensegrity robots," in *Proceedings of the 2013 international conference on Autonomous agents and multi-agent systems*, 2013.
- [14] A. P. Sabelhaus, J. Bruce, K. Caluwaerts, P. Manovi, R. F. Firoozi, S. Dobi, A. M. Agogino and V. SunSpiral, "System design and locomotion of SUPERball, an untethered tensegrity robot," in *2015 IEEE international conference on robotics and automation (ICRA)*, 2015.
- [15] B. R. Tietz, R. W. Carnahan, R. J. Bachmann, R. D. Quinn and V. SunSpiral, "Tetraspine: Robust terrain handling on a tensegrity robot using central pattern generators," in *2013 IEEE/ASME International Conference on Advanced Intelligent Mechatronics*, 2013.
- [16] Mirats-Tur, J. M. and J. Camps, "A three-DoF actuated robot," *IEEE robotics & automation magazine*, vol. 18, no. 3, pp. 96-103, 2011.
- [17] S. Burt, "Kinematics algorithms for tensegrity structures.," University of California, Santa Cruz, 2013.
- [18] I.-W. Park and V. SunSpiral, "Impedance controlled twisted string actuators for tensegrity robots," in *14th International Conference on Control, Automation and Systems (ICCAS 2014)*, 2014.
- [19] D. Fadeyev, A. Zhakatayev, A. Kuzdeuov and H. A. Varol, "Generalized dynamics of stacked tensegrity manipulators," *IEEE Access*, vol. 7, pp. 63472-63484, 2019.

- [20] V. Ramadoss, K. Sagar, M. S. Ikbal, J. H. L. Calles and M. Zoppi, "Hedra: a bio-inspired modular tensegrity soft robot with polyhedral parallel modules," arXiv:2011.14240, 2020.
- [21] E. Jung, V. Ly, N. Cessna, M. L. Ngo, D. Castro, V. SunSpiral and M. Teodorescu, "Bio-inspired tensegrity flexural joints," in *IEEE International Conference on Robotics and Automation (ICRA)*, 2018.
- [22] A. Preumont, Vibration control of active structures: an introduction, vol. 246, Springer, 2018.
- [23] C. C. Fuller, S. J. Elliott and P. A. Nelson, Active control of vibration, Academic press, 1996.
- [24] G. G. Rigatos, "Model-based and model-free control of flexible-link robots: A comparison between representative methods," *Applied Mathematical Modelling*, vol. 33, no. 10, pp. 3906-3925, 2009.
- [25] Z. Hou and S. Jin, Model free adaptive control, Boca Raton, FL: CRC Press, 2013.
- [26] W. L. Chan, D. Arbelaez, F. Bossens and R. E. Skelton, "Active vibration control of a three-stage tensegrity structure," *Smart Structures and Materials 2004: Damping and Isolation*, vol. 5386, pp. 340-346, 2004.
- [27] H. Liu, J. Zhang and W. Zhao, "An intelligent non-collocated control strategy for ball-screw feed drives with dynamic variations," *Engineering*, vol. 3, no. 5, pp. 641-647, 2017.
- [28] W. P. Engels, O. N. Baumann, S. J. Elliott and R. Fraanje, "Centralized and decentralized control of structural vibration and sound radiation," *The journal of the Acoustical Society of America*, pp. 1487-1495, 2006.
- [29] W. Levine and M. Athans, "On the determination of the optimal constant output feedback gains for linear multivariable systems," *IEEE Transactions on Automatic control*, vol. 15, no. 1, pp. 44-48, 1970.

- [30] M. J. Balas, "Direct velocity feedback control of large space structures," *Journal of guidance and control*, vol. 2, no. 3, pp. 252-253, 1979.
- [31] J. Q. Sun, "Some observations on physical duality and colocation of structural control sensors and actuators," *Journal of Sound and Vibration*, vol. 194, no. 5, pp. 765-770, 1996.
- [32] E. J. Davison and S. H. Wang, "Properties and calculation of transmission zeros of linear multivariable systems," *Automatica*, vol. 10, no. 6, pp. 643-658, 1974.
- [33] Š. Zbyněk and M. Hajžman, "TA ČR Starfos: Projekt: GA20-21893S," TA ČR Starfos, 2022. [Online]. Available: <https://starfos.tacr.cz/cs/project/GA20-21893S>. [Accessed 1 July 2022].
- [34] T. Kaňka, Tensegritní mechanismy pro nahradu prostorových seriových robotů, Master's thesis, České vysoké učení technické v Praze. Vypočetní a informační centrum., 2021.
- [35] M. Del Giudice, "Self-regulation in an evolutionary perspective," in *Handbook of biobehavioral approaches to self-regulation*, New York, NY, Springer, 2014, pp. 25-41.
- [36] Omegatron, "Wikimedia Commons," 4 November 2007. [Online]. Available: [https://commons.wikimedia.org/wiki/File:Piezoelectric\\_sensor\\_frequency\\_response.svg](https://commons.wikimedia.org/wiki/File:Piezoelectric_sensor_frequency_response.svg). [Accessed 6 July 2022].
- [37] PCB Piezotronics, Inc., "Model : 208C02 | ICP® Force Sensor," PCB Piezotronics, Inc., 2022. [Online]. Available: <https://wwwpcb.com/products?m=208C02>. [Accessed 5 July 2022].
- [38] PCB Piezotronics, "PCB Piezotronics, Inc.," 2022. [Online]. Available: [https://wwwpcb.com/contentStore/docs/pcb\\_corporate/forcetorque/products/manuals/208c02.pdf](https://wwwpcb.com/contentStore/docs/pcb_corporate/forcetorque/products/manuals/208c02.pdf). [Accessed 6 July 2022].
- [39] M. Simic and N. Herakovič, "Piezo actuators for the use in hydraulic and pneumatic valves," in *Fluid power 2017*, 2017.

- [40] F. Claeysen, R. L. Letty, F. Barillot and O. Sosnicki, "Amplified piezoelectric actuators: Static & dynamic applications," *Ferroelectrics*, vol. 351, no. 1, pp. 3-14, 2007.
- [41] CEDRAT TECHNOLOGIES, "Product: Amplified piezo actuator - APA120ML," 2022. [Online]. Available: <https://www.cedrat-technologies.com/fileadmin/datasheets/APA120ML.pdf>. [Accessed 7 July 2022].
- [42] O. Yaowen, X. Feng and M. Mohammad Shamim, "Active vibration control of tensegrity structures for performance enhancement: A comparative study," *Earthquake Engineering and Engineering Vibration*, vol. 18, no. 3, pp. 679-693, 2019.
- [43] X. Feng, M. Mohammad S. and O. Yaowen, "Dynamic behavior and vibration mitigation of a spatial tensegrity beam," *Engineering Structures*, vol. 171, pp. 1007-1016, 2018.
- [44] W. K. Gawronski, Dynamics and control of structures: A modal approach, Springer Science & Business Media, 2004.
- [45] I. Bruant and P. Laurent, "Optimal location of actuators and sensors in active vibration control," *Journal of intelligent material systems and structures*, vol. 16, no. 3, pp. 197-206, 2005.
- [46] A. Hać and L. L., "Sensor and actuator location in motion control of flexible structures," *Journal of sound and vibration*, vol. 167, no. 2, pp. 239-261, 1993.
- [47] M. Bruce C., "Principal component analysis in linear systems: Controllability, observability, and model reduction," *IEEE transactions on automatic control*, vol. 26, no. 1, pp. 17-32, 1981.
- [48] P. SVATOŠ, *Optimalizace a řízení pohybu vláknově ovládaných paralelních mechanismů*, Praha: FS ČVUT, 2016.
- [49] A. A. Hanieh, *Active isolation and damping of vibrations via Stewart platform*, Université Libre de Bruxelles, Active Structures Laboratory, 2003.

- [50] The MathWorks, Inc., "hinfstruct," The MathWorks, Inc., 1994-2022. [Online]. Available: <https://www.mathworks.com/help/robust/ref/lti.hinfstruct.html>. [Accessed 29 July 2022].
- [51] The MathWorks, Inc., "append," The MathWorks, Inc., 1994-2022. [Online]. Available: <https://www.mathworks.com/help/control/ref/lti.append.html>. [Accessed 29 July 2022].
- [52] S. R. Moheimani and A. J. Fleming, Piezoelectric transducers for vibration control and damping, London: Springer, 2006.
- [53] NATIONAL INSTRUMENTS CORP., "Understanding Dynamic System Models (Control Design and Simulation Module)," NATIONAL INSTRUMENTS CORP., 2022. [Online]. Available: [https://www.ni.com/docs/en-US/bundle/labview-control-design-and-simulation-module/page/lvsimconcepts/sim\\_c\\_models.html](https://www.ni.com/docs/en-US/bundle/labview-control-design-and-simulation-module/page/lvsimconcepts/sim_c_models.html). [Accessed 5 July 2022].
- [54] J. Curie and P. Curie, "Développement par compression de l'électricité polaire dans les cristaux hémièdres à faces inclinées," *Bulletin de minéralogie*, vol. 3, no. 4, pp. 90-93, 1880.
- [55] Cedrat Technologies, "Piezo actuators," Cedrat Technologies, [Online]. Available: <https://www.cedrat-technologies.com/en/products/piezo-actuators.html>. [Accessed 4 July 2022].
- [56] CEDRAT TECHNOLOGIES, "Product: Parallel Pre-stressed Actuator - PPA40L," 2022. [Online]. Available: <https://www.cedrat-technologies.com/en/products/product/PPA40L.html>. [Accessed 7 July 2022].
- [57] CEDRAT TECHNOLOGIES, "Product: Amplified piezo actuator - APA100M," 2022. [Online]. Available: <https://www.cedrat-technologies.com/en/products/product/APA100M.html>. [Accessed 7 July 2022].
- [58] Š. Miroslav and H. Zdeněk, Úvod do metody konečných prvků, Praha: ČVUT, 2011.